UC San Diego
UC San Diego Electronic Theses and Dissertations

Title

Ultrafast Dynamics and Interfacial Structural Orientation Investigated with Multidimensional Vibrational Spectroscopy

Permalink

https://escholarship.org/uc/item/8c19821r

Author

Wang, Jiaxi

Publication Date

2019

Peer reviewed|Thesis/dissertation

UNIVERSITY OF CALIFORNIA SAN DIEGO

Ultrafast Dynamics and Interfacial Structural Orientation Investigated with Multidimensional
Vibrational Spectroscopy

A dissertation submitted in partial satisfaction of the
requirements for the degree
Doctor of Philosophy

in

Chemistry

by

Jiaxi Wang

Committee in charge:

    Professor Wei Xiong, Chair
    Professor Richard Averitt
    Professor Judy Kim
    Professor Joel Yuen-Zhou
    Professor Brian Zid

2019

The dissertation of Jiaxi Wang is approved, and it is acceptable in quality and form for publication on microfilm and electronically:

_____

_____

_____

_____

_____

Chair

University of California San Diego

2019

TABLE OF CONTENTS

LIST OF FIGURES

LIST OF TABLES

ACKNOWLEDGEMENTS

VITA

2014   B. S. in Chemistry, Wuhan University, Wuhan, China.

2014-2017   Teaching Assistant, University of California, San Diego

2017-2019   Research Assistant, University of California, San Diego

2019   Ph. D. in Chemistry, University of California, San Diego

ABSTRACT OF THE DISSERTATION

Ultrafast Dynamics and Interfacial Structural Orientation Investigated with Multidimensional
Vibrational Spectroscopy

by

Jiaxi Wang

Doctor of Philosophy in Chemistry

University of California San Diego, 2019

Professor Wei Xiong, Chair

In this thesis, two multidimensional spectroscopic methods — two-dimensional infrared
(2D IR) spectroscopy and heterodyne 2D sum frequency generation (HD 2D SFG) spectroscopy
— were applied to investigate ultrafast chemical exchange of organometallics in bulk solution and
structural orientation of surface catalysts at interface, respectively.

2D IR spectroscopy was used to study the ultrafast chemical exchange of two organometallics
compound ($Ru(S_2C_2(CF_3)_2)(CO)(PPh_3)_2$ and $Co(CNAr^{Mes2})_4$) occurring on the picosecond
time scale. Combined with DFT simulation results, 2D IR provides direct evidence of the ex-
istence of various isomers. For the five-coordinate Ru complex, one isomers that serves as the

intermediate of the axial-equatorial exchange was observed for the first time. Furthermore, 2D IR was successful at identifying the surprisingly low kinetic barriers of dynamic exchange between multiple, considering both of the transition metal complexes under study have relatively large ligands. The low kinetic barriers are attributed to the small core-angle movement involved in the chemical exchange. 2D IR was also applied to $W(CO)_6$/dual cavity system to observe ultrafast intercavity nonlinear polariton interactions. Combined with a newly developed theory model, we show that the nonlinear interaction is realized by shared molecular anharmonicities among cavity modes, e.g. through mode delocalization, some molecules (with anharmonicity) are coupled by cavity modes adjacent to each other.

HD 2D SFG spectroscopy was used to study a model CO_2 reduction catalyst, Re(diCN-bpy)(CO)$_3$Cl, as a monolayer on a gold surface. We show that short-range interactions with the surface can cause substantial line-shape differences between vibrational bands from the same molecules. This interaction can be explained as the result of couplings between CO vibrational modes of the catalyst molecules and the image dipoles on gold surface, which are sensitive to the relative distance between the molecule and the surface. Thus, by analysis of HD 2D SFG line-shape differences and polarization dependences of IR spectra, the ensemble-averaged orientation of the molecules on the surface can be determined unambiguously. The high sensitivity of HD 2D SFG spectra to short-range interactions can be applied to many other adsorbate–substrate interactions and therefore serve as a unique tool to determine adsorbate orientations on surfaces.

In addition, surface molecules of the monolayers can adopt conformations with many different orientations. Thus, it is necessary to describe the orientations of surface molecular monolayers using both mean tilt angle and orientational distribution, which together we refer to as orientation heterogeneity. Orientation heterogeneity is difficult to measure and in most cases, in order to calculate the mean tilt angle, it is assumed that the orientational distribution is narrow. This assumption causes ambiguities in determining the mean tilt angle and loss of orientational distribution information, which is known as the "magic angle" challenge. Using

HD 2D SFG spectroscopy, we report a novel method to solve the "magic angle" challenge, by simultaneously measuring mean tilt angle and orientational distribution of molecular monolayers. Although applied to a specific system, this method is a general way to determine the orientation heterogeneity of an ensemble-averaged molecular interface.

Chapter 1

Introduction

The complexity of molecular dynamics in solution is attributed to the many forces present within the bulk system. Forces, such as those between molecules, that lead to the time evolution of molecular or collective structures, and irreversible relaxation processes are often convoluted and ambiguous. Thus, finding simplified descriptions for the various interactions present in a complex system is of great importance to understanding conformational changes in solutes, fluctuations in solvent configuration, and vibrational relaxation processes.

Time-resolved experimental methods are useful tools in investigations of time evolving molecular or collective structures since molecular dynamics in solution always involve structural changes on picosecond or longer time scales. Such methods must statistically analyze structural variation of an ensemble as well as show how this variance evolves with time.[3]

Though one-dimensional (1D) electronic and vibrational spectroscopies have the intrinsic time-resolution required for such studies, interpreting them is generally ambiguous. This is because 1D spectroscopies project ensemble-averaged responses of the electronic or nuclear coordinates onto one frequency axis, generating ambiguous results from the multiple degrees of freedom in the system. As a result, it is generally impossible to separate overlapping spectral contributions and line broadening processes in 1D spectra. More importantly, although the

signatures of different nuclear or electronic coordinates may be present, the structural and dynamical relationships between these coordinates is usually challenging to establish.

To unravel the underlying molecular interactions that are obscured in traditional methods, multidimensional spectroscopies have been developed.[4–6] Such techniques apply a sequence of electromagnetic fields to monitor a system as a function of multiple time periods or frequency variables. Two-dimensional (2D) nuclear magnetic resonance (NMR) has been used for some time as a tool for determining solution phase structures. For example, in a 2D NMR spectrum, spectral information is spread over two frequency axes as compared to one in 1D NMR. "Cross peaks" between the resonances on the diagonal axis very often indicate coupling between spin states experiencing different chemical environments.[6, 7] Unfortunately, 2D NMR has seen limited use in studying molecular dynamics in solution because the measurement time scale is in the millisecond range, while lots of chemical exchanges happen on the picosecond timescale.

Ultrafast multidimensional vibrational spectroscopy has since been developed and has proven itself to be a powerful probe of both chemical and biological systems for the past decade. Such techniques includes Two-dimensional IR (2D IR) spectroscopy,[8–13] 2D Raman experiments,[14, 15] and mixed IR-Raman 2D spectroscopies, etc.[16–19] 2D IR methodology is closely related to that of 2D NMR methods.[6, 7] 2D IR is based on a sequence of ultrafast infrared laser pulses which are applied to vibrational resonances whose frequencies are dictated by bonding and local environments. As a vibrational spectroscopic method, the main advantage of 2D IR spectroscopy over 2D NMR arises from the inherent high time resolution (many orders of magnitude faster than NMR methods), as a result of the short free-induction decay times of vibrational transitions. Resolving ultrafast molecular dynamics in picosecond to millisecond timescale is made possible with advances in laser technology that has enabled a new generation of mid-IR pulses with durations on the order of 100 fs. This time resolution, combined with the ability of infrared spectroscopy to provide detailed information on molecular structure and local environments, provides new approaches that can be used to characterize features that are

masked in traditional methods. Thus, 2D IR has been established as a powerful tool to probe the structural fluctuations and conformational variation in previously inaccessible detail.[20–22] The range of topics that 2D IR has been used to explore has greatly expanded since the technique was first developed,[23] including vibrational relaxation dynamics such as intramolecular vibrational energy transfer,[24, 25] hydrogen bonding environments and solvent–solute interactions indicated by 2D line shapes,[26–31] the investigation of rates of chemical exchange at chemical equilibrium,[27, 32, 33] and study of protein structure in solution.[23, 34–38]

We will now change our concentration from solution phase dynamics to molecules at surfaces or interfaces. The properties of chemical bonds and absorbate-substrate interactions of molecules at solid-liquid/gas interfaces play a prominent role in chemistry, biology, and physics. Although this importance is widely acknowledged,[39–56] a detailed molecular understanding of dynamic properties at interfaces is still a challenge to obtain experimentally. The challenge partly lies in the fact that molecules at surfaces can adopt many different structural orientations, which generate a high level of inhomogeneity from a microscopic point of view. As a result, the dynamic properties are more complicated than in bulk solution. In addition, molecular properties generated by molecules at surfaces are easily overwhelmed by those generated from the bulk generally, which makes the study of interfacial molecules even more difficult. Therefore, one of the most essential aspects common for all the interfacial systems is to determine how molecules at an interface perform for desired physical or chemical process to occur. Examples regarding this question, ranging from fundamental science to technical applications, have been investigated in depth. Possibly the best-known process is related to molecular self-assembly of covalently bound adsorbates at surfaces.[57–62] Great interests in solid-liquid/gas interfaces also exist from the perspective of chemical synthesis or in the field of energy science, both of which have strong connections to heterogeneous (photo-) catalysis.[63–70] The goals here are to clarify the role of interactions between the surface and adsorbates,[71–74] and to understand vibrational energy flow at interfaces along with its relevance for chemical reactions.[75–78] Other

aspects of surface science, with high commercial and social relevance emerge from the fields of molecular electronics[79–82] and energy supply, including topics such as the understanding of charge migration at electrode-electrolyte interfaces in, e.g., battery devices.[83–85]

In this regard, experimental methods that are sensitive only to molecular properties at interfaces are ideal for studying molecules at surfaces. It is well-known that even-order nonlinear spectroscopic methods such as second harmonic generation (SHG) and sum frequency generation (SFG) spectroscopy are intrinsically surface sensitive — detect only response from non-centrosymmetric systems, e.g. surfaces and interfaces.[86] One dimensional sum frequency generation spectroscopy[87–89] is powerful approach to investigate surfaces under working conditions, which can distinguish whether a molecular group is pointing towards or away from the surface (in microscopic view) by the sign of the signal when heterodyne detected and phase corrected.[90–96] However, the intrinsic spectral broadening of most one-dimensional spectroscopic methods still makes understanding surface interactions difficult.[97] As discussed previously, 2D IR is particularly powerful in determining interactions between functional groups or between molecules, in addition to resolving mechanisms of line broadening of vibrational bands. These capabilities of 2D IR, if combined with a surface specific spectroscopic method such as SFG, can be applied to the molecules at surfaces/interfaces, extracting information such as inter- and intra- molecular interaction and dynamics of absorbates can be made available also to surface science.

Efforts have been made to achieve this combination of techniques in experimental practices. 2D SFG spectroscopy[91, 96, 98, 99] can be viewed as a surface sensitive version of 2D IR. It is capable of resolving homogeneous and inhomogeneous dynamics and molecular orientation on molecular submonolayers including air/water interfaces,[91, 99] electrode surfaces, and surface bound biomolecules,[96] which makes it an ideal technique to probe molecules on surfaces. In its initial implementation, 2D SFG was used as a homodyne detected method for investigations of liquid-air interfaces,[99–103] which have been the first experiments to demonstrate that

multidimensional vibrational spectroscopy can be extended to monolayer samples at interfaces. Later on, the implementation of heterodyne detection considerably advanced 2D SFG in the interpretation of the obtained spectra, and broadened the applications of 2D SFG to systems at solid-liquid interfaces to study surface specific signals of CO adsorbed to platinum electrodes,[98] surface-bound peptides[96] and DNA strands,[104] amyloid fibers,[94] as well as metal carbonyl electrocatalysts.[74, 105, 106]

Chapter 2

Multidimensional Vibrational Spectroscopy in Theory

2.1 Linear Macroscopic Polarization

Macroscopic polarization is the signal emitted by a system in interaction with an external electric field. In general, the polarization ($P(\omega)$) of a sample induced by light of frequency ω is expanded in powers of the incident electric fields ($E_i(\omega)$): [86]

$$
\begin{aligned}
P(\omega) = \varepsilon_0 [& \chi^{(1)} E_1(\omega) + \chi^{(2)} E_1(\omega) E_2(\omega) + \chi^{(3)} E_1(\omega) E_2(\omega) E_3(\omega) \\
& + \chi^{(4)} E_1(\omega) E_2(\omega) E_3(\omega) E_4(\omega) + \cdots] \\
\equiv & P^{(1)}(\omega) + P^{(2)}(\omega) + P^{(3)}(\omega) + P^{(4)}(\omega) + \cdots
\end{aligned}
\tag{2.1}
$$

In linear optics, the polarization depends linearly on the electric field E:

$$
P(\omega) = P^{(1)}(\omega) = \varepsilon_0 \chi^{(1)} \cdot E(\omega)
\tag{2.2}
$$

with $\chi^{(1)}$ the linear susceptibility. This susceptibility is related to IR absorption spec-troscopy.

For linear spectroscopy such as FTIR, macroscopic polarization relies on the linear response as described in time-domain representation in the following function:[22]

$$P(t) = P^{(1)}(t) = \frac{i}{\hbar} \int_0^\infty dt_1 \mu_1 E_0(t - t_1) \cdot R^{(1)}(t_1) \tag{2.3}$$

where μ_1 is the transition dipole moment of the sample, and $R^{(1)}(t_1)$ is the first order response function. The emitted signal field $E^{(1)}(t)$ is given by:

$$E^{(1)}(t) \propto iP^{(1)}(t) \tag{2.4}$$

which is called the free induction decay.

2.2 Nonlinear Macroscopic Polarization

However, when the external electric fields are intense enough, the above linear relation between macroscopic polarization and electric field does not hold anymore because the nonlinear terms in the expansion (Eq. 2.1) become non-negligible.

2D IR is a third order spectroscopic technique and as such, the macroscopic response ($P^{(3)}(t)$) is associated with $\chi^{(3)}$ and a function of three input pulses. In ultrafast spectroscopy,

it is more convenient to use a time-domain representation instead of the frequency-domain representation of Eq. 2.1. In a 2D IR pulse sequence each pulse interacts with the sample at time intervals t_1, t_2, and t_3. Therefore, an expression for the macroscopic polarizability can be written as:[1]

$$P^{(3)}(t) \propto (\frac{i}{\hbar})^3 \int_0^\infty dt_3 \int_0^\infty dt_2 \int_0^\infty dt_1 \mu_3 E_3(t-t_3)\mu_2 E_2(t-t_3-t_2)$$
$$\mu_1 E_1(t-t_3-t_2-t_1) \cdot R^{(3)}(t_3,t_2,t_1)$$

(2.5)

where $P^{(3)}$(t) results from the convolution of the three external IR fields with the response function $R^{(3)}$(t) generated by samples. The emitted signal field $E^{(3)}$(t) is given by:

$$E^{(3)}(t) \propto iP^{(3)}(t)$$

(2.6)

The variables t_i are time intervals between the successive ultrashort IR pulses. These time delays can be controlled in experiments and are scanned to acquire 2D spectra, as well as dynamics of systems under study. The response function $R^{(3)}$(t) constitutes all possible pathways for the electric fields to act on the sample and emit signal. For the simple case of a single vibrational mode that is not coupled to any other mode, three pathways known as ground state bleach (GSB), stimulated emission (SE), and excited state absorption (ESA) are represented in the energy-level diagram (Figure 2.1) introduced by Albrecht et al.[107, 108]

For a standard 2D IR signal, the three lowest vibrational levels, i.e. v = 0, 1, 2 are often in consideration. The 0 -1 transition (GSB/SE) and 1-2 transition (ESA) result in opposite signs of the signal: 0 -1 transition reduce absorption of the probe IR pulse, while 1-2 transition introduce

8
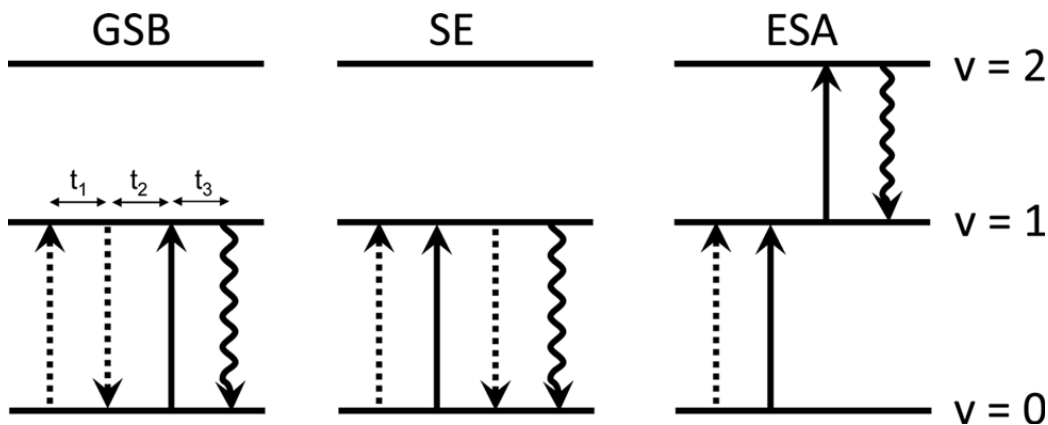
Figure 2.1: Energy level diagrams for third-order IR spectroscopy. Only rephasing diagrams are shown for clarity. Vibrational states (v = 0, 1, 2) are represented by horizontal lines. Signal emission is indicated with a wavy arrow. Figure reproduced from [1]

new absorption (Figure 2.2). Therefore, for a vibrational mode to be observable in 2D IR, the mode cannot be a ideal harmonic mode — 0 -1 and 1-2 transition will have same frequency yet opposite sign and cancel out each other.

In general, the three pulses involved in Two-dimensional IR are two pump pulses and a probe pulse. The first and third interaction with IR pulse to produce vibrational coherences, which oscillate as functions of t_1 and t_3, respectively. Thus, t_1 and t_3 are referred to as "coherence time". The second pump pulse interacts with the system and converts the coherence state produced by first pump pulse to a population state, which makes t_2 the "population time". 2D IR spectra for a fixed population time t_2 are obtained after a 2D Fourier transformation of the emitted field as a function of coherence times t_1 and t_3,[22] which correspond to the two spectral axes in 2D IR spectra. often called "pump" (ω_1) and "probe" (ω_3) The shape of the resulting 2D IR spectra will depend on t_2.

In order to make 2D IR a surface specific method, we need to go one order higher in nonlinearity ($\chi^{(4)}$). The reason even-order spectroscopic methods are surface specific lies in the requirement of a break in symmetry for even-order χ terms to not to be zero. In other words, in any centrosymmetric system, such as bulk solution, even-order χ needs to be zero for the centrosymmetric properties to hold. Thus, only noncentrosymmetric systems i.e. surfaces and
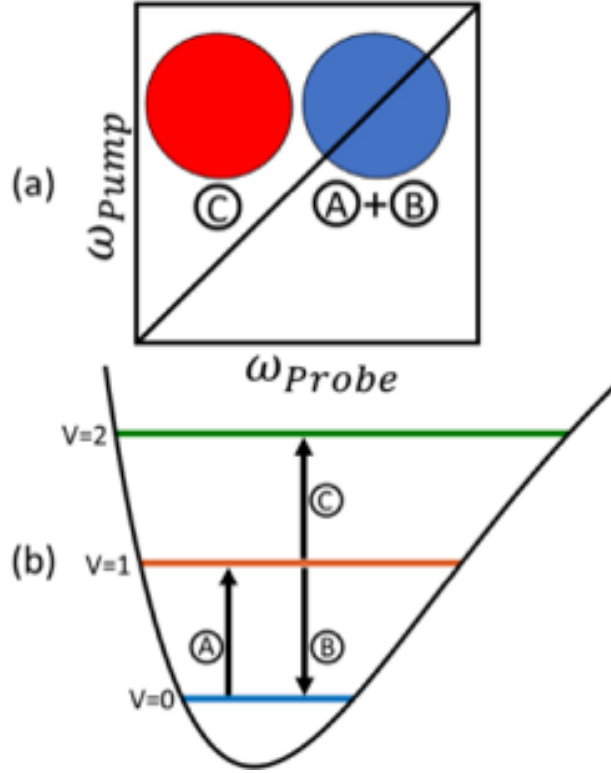
Figure 2.2: a) Cartoon representation of a 2D IR spectrum. b) corresponding enerfy level diagram in an anharmonic vibrational mode. Transitions are labeled as a, b, and c.Figure reproduced from[2]

interfaces would generate non-zero even-order χ and polarization signal.

This can be achieved by adding an additional fourth pulse to the three-pulse 2D IR sequence. The fourth electric field comes from a VIS pulse, which up-converts the free induction decay of $P^{(3)}(t)$ to a VIS signal. The method is terms sum frequency generation (SFG) spectroscopy due to the summation of IR and VIS frequencies. In the same way, the fourth-order polarization in 2D SFG can be represented in time-domain as following:

$$
\begin{aligned}
P^{(4)}(t) \propto (\frac{i}{\hbar})^4 \int_0^\infty dt_4 \int_0^\infty dt_3 \int_0^\infty dt_2 \int_0^\infty dt_1 \\
\alpha E_{4,VIS}(t-t_4)\mu_3 E_3(t-t_4-t_3)\mu_2 E_2(t-t_4-t_3-t_2) \\
\mu_1 E_1(t-t_4-t_3-t_2-t_1) \cdot R^{(4)}(t_4,t_3,t_2,t_1)
\end{aligned}
\tag{2.7}
$$

where the laser pulses interact with the sample through either the transition dipole moments (IR, $\mu_{1,2,3}$)or the molecular polarizability (VIS, α).

It is noteworthy that the frequency of the up-converting VIS pulse is generally tuned off-resonance to any molecular electronic transition. In such case, the VIS interaction with a nonresonant virtual state and is very short lived ($\approx$ 1 fs) as compared to the IR response, it can be approximated as a δ-shaped in time domain. The fourth-order response thus reduces to the product of the third-order response and the δ function:

$$R^{(4)}(t_4,t_3,t_2,t_1) = R^{(3)}(t_3,t_2,t_1) \cdot \delta(t_4) \tag{2.8}$$

The expression for $P^{(4)}$(t) thus simplies to a 3-fold integral:

$$\begin{aligned}
P^{(4)}(t) \propto (\frac{i}{\hbar})^4 \alpha E_{4,VIS} &\int_0^\infty dt_3 \int_0^\infty dt_2 \int_0^\infty dt_1 \\
&\mu_3 E_3(t-t_3)\mu_2 E_2(t-t_3-t_2) \\
&\mu_1 E_1(t-t_3-t_2-t_1) \cdot R^{(3)}(t_3,t_2,t_1)
\end{aligned} \tag{2.9}$$

Also with a signal field $E^{(4)}$(t) emitted from the sample:

$$E^{(4)}(t) \propto iP^{(4)}(t) \tag{2.10}$$

Similarly, there are three pathways (GSB, SE, ESA) in the response function of a standard uncoupled vibrational mode in 2D SFG. The energy level diagrams are also comparable to those

11

for 2D IR, with the addition of a fourth VIS pulse and a virtual state (Figure 2.3).
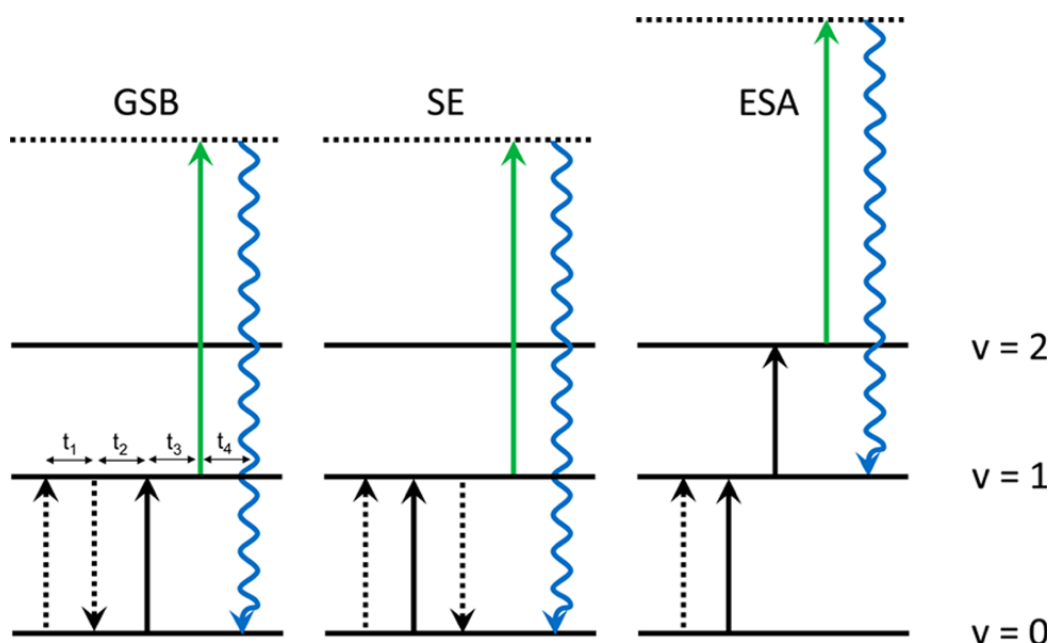
Figure 2.3: Energy level diagrams for fourth-order 2D SFG. Only rephasing diagrams are shown for clarity. Vibrational states (v = 0, 1, 2) are represented by solid horizontal lines, while virtual states are represented by dashed horizontal lines. Figure reproduced from [1]

It is also important to note that the addition of the fourth VIS pulse in 2D SDF requires additional terms in selection rule to the systems for 2D IR — vibrational mode needs to not only non-zero transition dipole moment (μ), but also non-zero transition polarizability (α)

When obtaining 2D SFG spectra, the VIS up-conversion frequency is commonly subtracted from the signal frequency to shift back to IR spectral range, considering the rule of summation of frequencies in SFG. In this way, 2D SFG as a surface specific version of 2D IR, generally provides similar information and have similar spectral appearances to 2D IR.[74]

2.3   Lineshape Broadening

Homogeneous and inhomogeneous broadening are two sources of spectral broadening that are challenging to differentiate in linear absorption spectroscopy. Homogeneous broadening

are originated from very fast flucuations between molecules and the bath modes in the solvent system, while inhomogeneous broadening comes from the same molecules experiencing different local environments, thus having a distribution of different frequencies, as depicted in Figure 2.4a.[37, 109] Fortunately, these different broadening processes also manifest themselves in 2D IR spectra. As shown in Figure 2.4, a chemical system experiences inhomogeneous broadening would generate an elongated peak along the diagonal of 2D spectra, while homogeneously broadened modes show up as round peaks on diagonal.
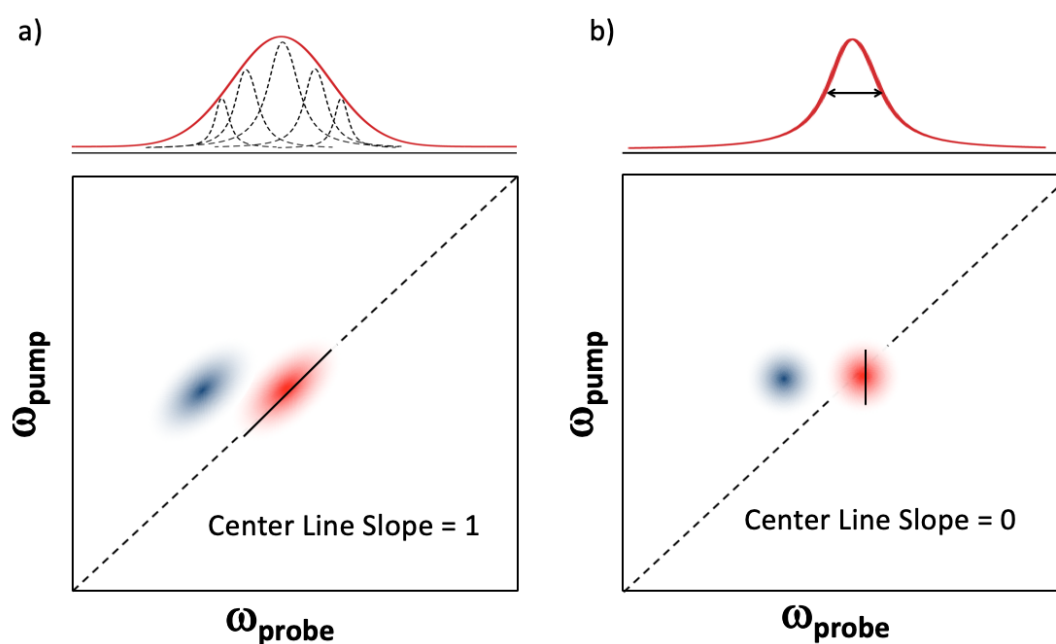
Figure 2.4: a) Inhomogeneously broadened spectral feature in linear IR and 2D IR at early population time. b) Homogeneously broadened spectral feature in linear IR and 2D IR at later population time after vibrational mode samples all solvent environments.

2.4   Spectral Diffusion

The process of a inhomogeneously broadened spectral feature evolves over population time to a homogeneously broadened lineshape (after experiencing solute-solvent fluctuations and

sampling all solvent environments) is referred to as spectral diffusion.[110, 111] Such changes in line shape can be related to important physical properties, including the nature of the solvent-solute interactions and structral dynamics of the systems. Several techniques including monitoring the ellipticity of peak shapes, nodal line slopes (NLS) between the peak pairs, and monitoring the center line slope (CLS) of a particular peak in a 2D IR spectrum have been developed to quantify 2D IR peak shapes.[112–114] Regardless of the method used, spectral diffusion is essentially the experimental manifest of frequency frequency correlation function (FFCF),[115] which is an expression that describes the fluctuations of the frequencies of a molecule. FFCF are directly related to the fluctuations of the local environment around the oscillator/vibrational mode. The FFCF can be expressed as C(t) as in following equation:

$$C(t) = \langle \delta\omega(t)\delta\omega(0) \rangle \tag{2.11}$$

where $\delta\omega(t)$ is the difference between the measured frequency at time t and the average frequency over the course of the experiment:

$$\delta\omega(t) = \omega(t) - \langle \omega \rangle \tag{2.12}$$

14

Chapter 3

Multidimensional Vibrational Spectroscopy in Practice

3.1 Experimental Setup for 2D IR Spectroscopy

2D IR spectra were collected in pump-probe geometry, as shown in the schematic layout in Figure 3.1.[116, 117] The pulse sequence is described in Figure 3.2. Two pump pulses and a probe pulse (pulse duration of 100-150 fs) interact with samples at delayed times (t_1, t_2 and t_3).

To generate the pulse sequence, 800 nm laser pulses ($\approx$35 fs, $\approx$6 W, 1 kHz) were generated by ultrafast Ti:Sapphire regenerative amplifier (Astrella, Coherent) . The 800 nm was converted into mid-IR pulses by optical parametric amplifier (TOPAS, LightConversion) followed by a different frequency generation process on a Type II $AgGaS_2$ crystal (Eksma). The mid-IR pulse (30 μJ) was split into two beams by a CaF_2 wedge beam-splitter. The majority (95%) was sent into a Ge-AOM based pulse shaper (QuickShape Kit, PhaseTech) to prepare the two pump pulse in the pulse sequences, whereas 5% mid-IR served as the probe. The pump pulse pair (2 μJ at the sample), the probe ($<$0.5 μJ) were all focused and spatially overlapped on the sample by a f = 10 cm parabolic mirror and collimated by another parabolic mirror in a symmetric geometry. In
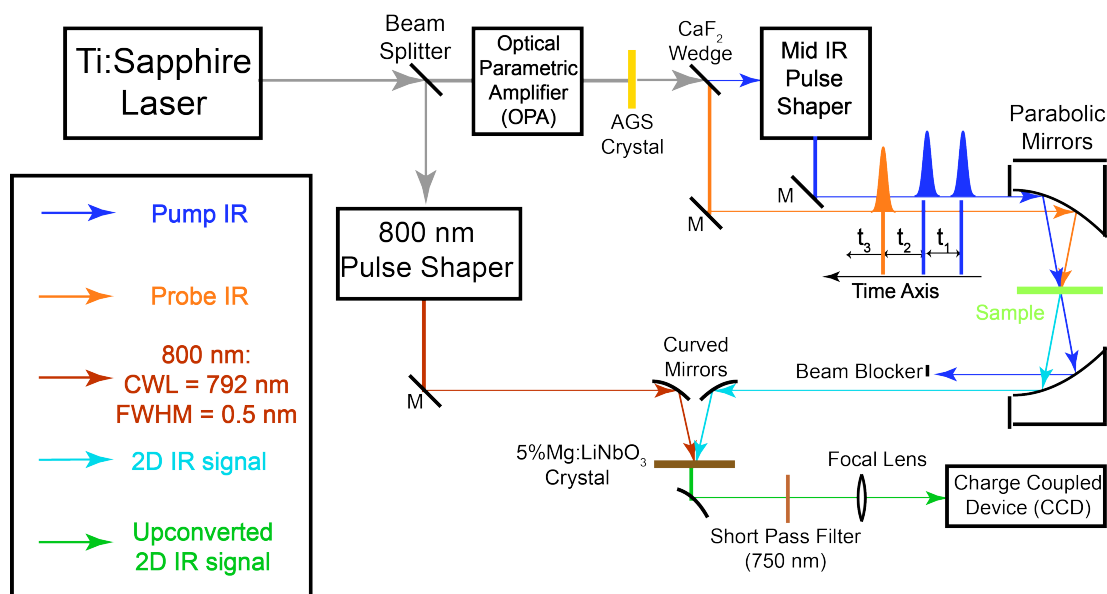
Figure 3.1: Scheme of 2D IR experimental setup.
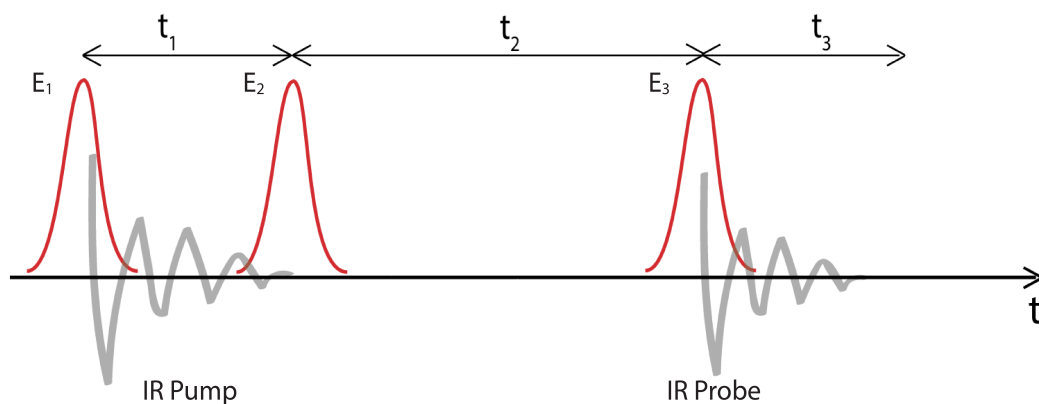
Figure 3.2: Pulse sequence in 2D IR experiment. E_1, E_2 and E_3 are the mid IR pulses interacting with the molecules.

order to detect the output IR signal by the CCD camera ($256 \times 1{,}024$, Andor), the collimated signal and the probe beam were then upconverted by a residue 800 nm beam on a 5%Mg: $LiNbO_3$ crystal. [118, 119] The 800 nm beam that comes out of the OPA passes through an 800 nm pulse shaper which narrows its spectrum in the frequency domain (center wavelength of 791 nm and a FWHM of 0.5 nm or 9.5 cm^{-1}).

3.2 2D IR Data Collection and Analysis

In the 2D IR experiments, two vibrational coherences were generated during t_1 and t_3 periods, respectively. The first coherence was measured by scanning t_1 time from 0 to 2000 fs (could vary depending on the free induction decay time of the vibrational mode) in steps of 20 fs using the pulse shaper, where a rotating frame at $f_0=1583$ cm^{-1} was used to shift the oscillation period to 80 fs, so that the scanning step can meet with the Nyquist frequency requirement. After waiting for t_2, the third IR pulse (probe) interacts the sample, and generate the second coherence. The resulting macroscopic polarization emits an IR signal. This IR signal is upconverted by a narrow-band 800 nm beam. The upconversion process covers the t_3 time delay and the 800 nm pulse duration determines the scanning length of t_3.[97, 120] The up-converted IR signals (second vibrational coherence) were experimentally Fourier transformed by a spectrograph and detected by a CCD camera. To get full absorptive 2D IR spectra, the first vibrational coherence was numerical Fourier transformed along t_1 axis. The pump and probe pulses had the same polarization in 2D IR measurements. For the time dependent 2D IR measurements, t_2 was scanned by a computerized delay stage.

3.3 Experimental Setup for 2D SFG Spectroscopy

Heterodyne 2D Sum Frequency Generation (HD 2D SFG) spectrum3 is collected in a pump-probe geometry, with additional narrow band (fwhm $\approx$ 1.5nm) 800 nm pulse for the SFG process (Figure 3.3). The pulse sequence is described in Figure 3.4. In brief, three mid-IR pulses are sent to interact with the molecular sample, where two vibrational coherences are created during t_1 and t_3 period, and the picosecond 800 nm pulse is used to interact with the second vibrational coherence for sum frequency generation process.

To generate the pulse sequence, 800 nm laser pulses ($\approx$35 fs, $\approx$6 W, 1 kHz) are generated by ultrafast Ti:Sapphire regenerative amplifier (Astrella, Coherent) . The 800 nm is then converted
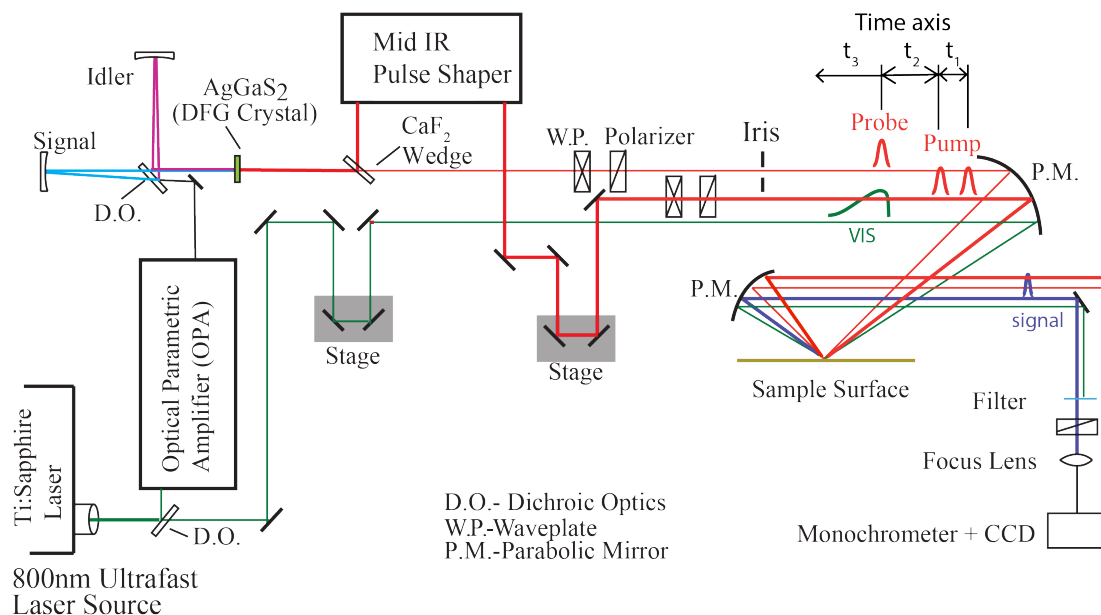
Figure 3.3: Scheme of 2D SFG experimental setup.
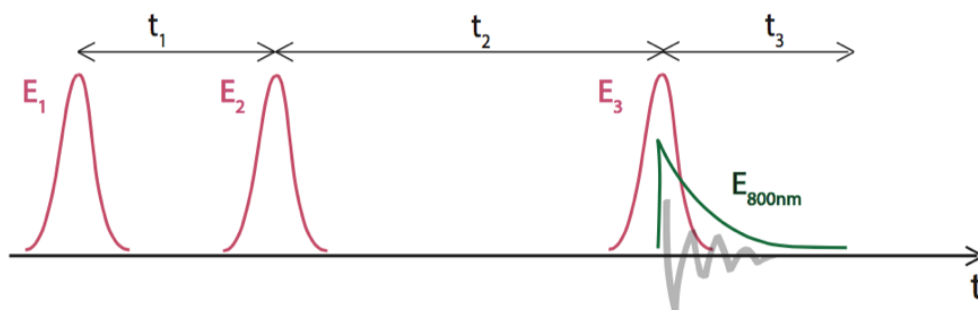
Figure 3.4: Pulse sequence in 2D SFG experiment. E_1, E_2 and E_3 are the mid IR pulses interacting with the molecules. The E_{800nm} is the upcoversion pulse that upconvert the vibrational coherence into a virtual state, following with a sum frequency generation signal.

into mid-IR pulses by optical parametric amplifier (TOPAS, LightConversion) followed by a different frequency generation process on a Type II $AgGaS_2$ crystal (Eksma). The mid-IR pulse (50 μJ) is split into two beams by a CaF_2 beam-splitter. The majority (95%) is sent into a home-assembled Ge-AOM based pulse shaper (QuickShape Kit, PhaseTech) to prepare the first two pump pulse pair in the pulse sequences, whereas 5% mid-IR served as the probe. The residue 800 nm beam after the OPA is narrowed to <1.5nm by an interference-based notch filter. The

pump pulse pair (4μJ at the sample), the probe ($\approx 1\mu$J) and the 800 nm upconversion pulse ($<$ 2μJ) are all focused and spatially overlapped on the sample by a f = 10 cm parabolic mirror.

During the mid-IR pulse interactions, two vibrational coherences are generated during t_1 and t_3 periods, respectively. The first coherence is measured by scanning the t_1 time from 0 to 2500 fs in steps of 20 fs using the pulse shaper, where a rotating frame at f_0=1583 cm^{-1} is used to shift the oscillation period to 80 fs, so that the scanning step can meet with the Nyquist frequency requirement. To remove scatter and linear SFG signal, instead of taking the difference between pump on and off SFG spectra, the difference SFG spectra at the same t_1 but with different pump pulse phase are recorded, which is known as phase cycling.[117] The second vibrational coherence is upconverted to a virtue state by a picosecond 800 nm pulse and subsequently emits visible signals through sum frequency generation process. Since the 800 nm serves as a window function, the t_3 time delay are simultaneously covered by the upconversion process and the 800 nm pulse duration determines how long t_3 is "scanned".[97, 120] The SFG signals are heterodyned by the local oscillator from non-resonance signal from gold surface and experimentally Fourier transformed by a spectrograph and detected by a CCD camera ($256 \times 1,024$, Andor). To get full 2D absorptive SFG spectra, the first vibrational coherence is numerical Fourier transformed into frequency domain.

3.4   2D SFG Data Collection and Analysis

SFG of bare gold was also collected as the reference for phase calibrations. The HD 2D SFG signal is measured at ppppp polarization, where the polarizations of all pulses are set to be p (in plain with the surface normal-incidence beam plain) to the sample, by pairs of waveplates and polarizers, and only p polarized signal is detected. We note in both our experiment and many other SFG experiments gold surfaces are used as the substrate, which generate the non-resonance SFG signal. In both experiments, the gold SFG signal can interfere with the SFG signal of interests.

Therefore, in principle, both experiments are self-heterodyned. The difference between our heterodyne detection scheme and the other SFG experiments, is that the measured self-heterodyne spectrum is further phase corrected by the reference SFG spectrum from bare gold, following the methods by Tahara.[90] In this way, we can extract both the real and imaginary part of the SFG spectra, whereas other experiments does not phase correct the spectrum and take advantage of this self-heterodyne scenario. The samples are constantly rastered between each scan ($\approx$10 mins) to avoid sample damaging. To improve signal to noise ratio, multiple scans are averaged for each time step.

To obtain absorptive HD 2D SFG spectra with calibrated phase, the non-resonance SFG signal from bare gold surface are collected for extraction of phase information.[90, 97, 121] First, we inversely Fourier Transform the SFG spectra of gold surface back to time domain. We then apply causality in the time domain to set any signal at t<0 to zero. The new time domain data is Fourier Transformed back to the frequency domain, and now the gold SFG spectra has both the real and imaginary part, where the linear phase φ can be extract from this complex spectra.

For the mixed time-frequency domain 2D SFG raw data, we applied the same time causality treatment. At each t_1 time, each SFG (ω_3) probe spectrum is inversely Fourier Transformed, applied time causality and Fourier Transformed back to time domain. Then, the complex SFG spectra is multiplied by the exp(-i$\times\varphi$) to remove fringes due to the linear phase. After this linear phase correction, the leftover signal in the imaginary part corresponds to the linear absorptive SFG spectra at a specific t_1 time. This absorptive SFG signal is background free, since the gold non-resonance signal is purely refractive (real). To accommodate the real and imaginary convention in 2D IR spectroscopy, the real and imaginary part of the SFG spectra are flipped, where after flipping, the real part corresponds to the absorption spectra and the imaginary part corresponds to the refraction spectra.

The difference spectra between two SFG spectra at the same t_1 but different pump pulse phase are the mixed time-frequency domain fourth order 2D SFG (t_1, ω_3) signal. The 2D SFG (t_1,

ω_3) are Fourier transformed along t_1 to obtain rephrasing and non-rephasing spectra 2D SFG (ω_1, ω_3).[98] The rephasing and non-rephasing spectra are separated in different quadrants, because of their different time dependent. By flipping the rephasing spectra back to the first quadrants and add them to the non-rephasing spectra, absorptive HD 2D SFG spectra can be retrieved.

Chapter 4

Direction Observation of the Intermediate in an Ultrafast Isomerization

4.1 Introduction

Chemical exchange dynamics is often studied by using Bloch equation analysis of coalescing lineshapes in nuclear magnetic resonance (NMR) spectroscopy. The typical (radio) frequencies used in the NMR experiment determine that dynamical time scales in the range of milliseconds to microseconds can be studied. A similar treatment has been applied to systems exchanging on the IR vibrational time scale.[122–124] For reactions occurring on the picosecond time, lineshape analysis of FTIR and Raman vibrational spectra can be applied. In practice, there are comparatively few examples of chemical exchange measurable by linear IR or Raman vibrational spectroscopy, because inhomogeneous broadening, solvent environment fluctuation and multiple dynamic processes in addition to chemical exchange can contribute to the overall lineshape. Examples of fast reactions can include intramolecular electron transfers,[123, 125, 126] proton transfers,[127] and isomerizations.[122, 128] Here, we present the study of the rapid structural isomerization of a five-coordinate ruthenium complex on the ultrafast (vibrational) time

scale.

The ruthenium complex, $Ru(S_2C_2(CF_3)_2)(CO)(PPh_3)_2$, was first reported by was first reported by Miller and Balch in 1971.[129] The solvent from which the complex is recrystallized determines whether orange crystals or a mixture of orange and violet crystals are obtained. X-ray crystal structure analysis revealed that both the orange and violet isomers were square pyramidal, differing only in the position of the carbonyl ligand.[130] The more stable orange isomer was found to have the CO in the apical position, and is referred to as **2** (see Figure 4.1) here, while the violet isomer had the CO in the equatorial plane, and is referred to as **1**. The solid state FTIR stretching frequencies for the CO in each of these isomers are separated by ca. 30 cm^{-1}(orange: v(COap), 1944 cm^{-1} ; violet: v(COeq), 1973 cm^{-1}),[129] while in methylene chloride (DCM) solutions at 20°C, only one broad absorption (FWHM $\approx$ 50 cm^{-1}) appears near the average frequency of the violet and orange isomers, (ca. 1958 cm^{-1}).
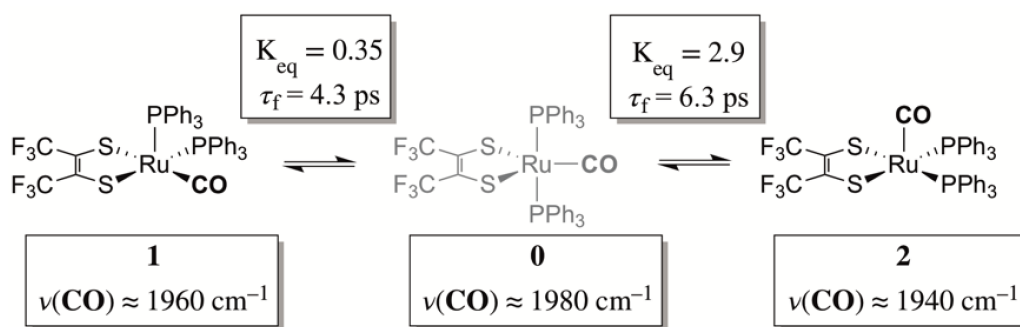
Figure 4.1: Isomerization of $Ru(S_2C_2(CF_3)_2)(CO)(PPh_3)_2$ as observed by 2D IR

Complete fittings of the solution 1D IR lineshape consisting of contributions from only these two isomers are less than satisfactory; owing to extra absorbance in the vicinity of 1980 cm^{-1} from a possible third minor component (vide infra). The solution state ^{31}P NMR in DCM-d_2 shows only one resonance at 47.57 ppm indicating that the ruthenium bound triphenylphosphine ligands experience an identical average environment, and the fluxional behavior of the ligands is faster than the NMR timescale (Figure 4.2, $k_{ex} > 10^6 s^{-1}$).[131] Together, these spectroscopic

observations suggest dynamic averaging on the ultrafast timescale of molecular vibrational modes.
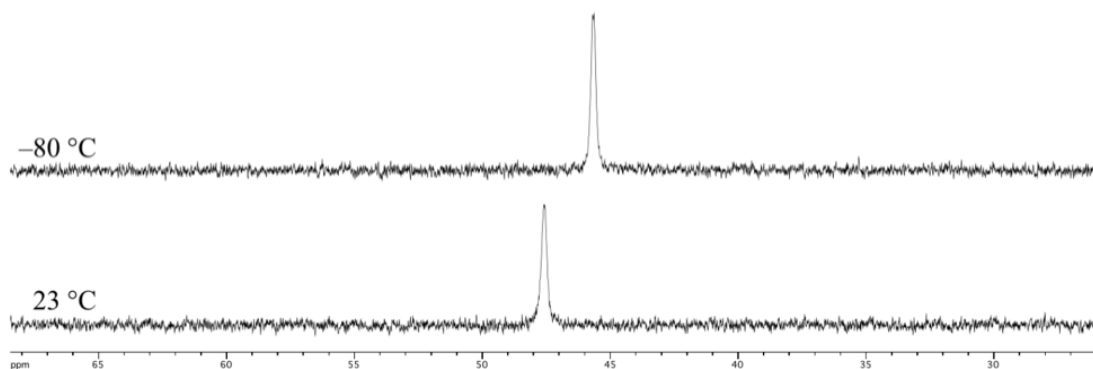
Figure 4.2: Variable temperature ^{31}P NMR in DCM-d_2.

Ultrafast two-dimensional infrared (2D IR) spectroscopy is a powerful method that can obtain molecular structure and provide details of dynamical processes with sub-picosecond time resolution.[3, 23, 34, 132–135] 2D IR spectroscopy has been applied to measure chemical exchange between two conformations in solution phase under thermal equilibrium.[27, 28, 32, 133, 136–139] In 2D IR spectroscopy, three ultrafast mid-IR pulses interact with the sample sequentially: the first two pulses initialize and interrogate vibrational coherences, which generate a transient vibrational tag, and the third pulse probes the evolution of these tagged vibrational modes (Figure 4.3). Because vibrational modes of molecules are sensitive to molecular conformations, local solvent environments, and excess internal energy, scanning the waiting time (t_2) between the second and third pulses can track the dynamics of chemical exchange,[27, 28, 133, 139] solvent fluctuation[113, 140–142] and vibrational energy relaxation.[25, 143–145] In the present study, 2D IR is employed to understand chemical exchange.

4.2   Methods

4.2.1   Sample Preparation and Purification

The 2,3-hexafluorobutyne was used as received from Oakwood Chemicals while the triruthenium doedecacarbonyl and triphenyl phosphine was used as received from Acros Organics. The cyclohexane stabilized dichloromethane (DCM), was purchased from VWR International LLC, deoxygenated and dried over alumina columns on a custom built solvent system under an argon atmosphere and stored over activated molecular seives (4 Å) in a nitrogen filled glove box. The 2,3-dithiolene and $Ru(S_2C_2(CF_3)_2)(CO)(PPh_3)_2$ were prepared following modified literature reported proceudures.[129] In brief:

Bis(perfluoromethyl)-1,2-dithietene. In accord with literature,[146] in a well ventilated fumehood, a 2 neck round bottom flask equipped with a short path distillation head was charged with 25 g (97.46 mmol) of sulfer and heated to 325 °C under a nitrogen stream. Upon reaching 325 °C, the 2,3-hexafluorobutyne was bubbled through the molten sulfer in short puffs and the dithietene was collected in a receiving Schlenk flask as a red-tinted oil.

$Ru(S_2C_2(CF_3)_2)(CO)(PPh_3)_2$. Under an inert atmosphere a 250 mL Schlenk flask was charged with 400 mg (0.63 mmol) of triruthenium dodecacarbonyl, 580 mg (2.57 mmol) of bis(perfluoromethyl)-1,2-dithietene, and approximately 100 mL of n-heptane that was heated under reflux. After 45 minutes, following carbon monoxide evolution an orange solid had precipitated. The flask was cooled and the orange solid was collected by vacuum filtration, washed with n-heptane, and dried under vacuum. The orange solid, tentatively identified as $Ru_2(S_2C_2(CF_3)_2)(CO)_6$ $[359 \text{ mg } (0.60 \text{ mmol})]$, was then added to a flask containing 1.1427 g (4.36 mmol) of triphenylphosphine suspended in 50 mL of n-heptane. After heating to reflux for 12 hours, the flask was cooled to 0 C and the crystalline complex was collected by filtration. Futher purification was achieved by recrystalization for dichloromethane/hexanes solutions where a mixture of orange and violet crystals were obtained.

4.2.2   Infrared Data Collection and Analysis

Infrared spectra were collected on a Bruker Equinox 55 FTIR spectrometer using a SPECAC flow through optical cryostat (model, 21525) with a 1.12 mm path length (determined from infringing pattern), CaF_2 windowed cell enclosed in a vacuum jacketed housing. Solutions were prepared in a glove box under a nitrogen atmosphere using pre-dried DCM from a mixture of orange and violet crystals. Cell temperature (± 1 °C) was regulated by addition of liquid nitrogen/methanol to the cooling compartment and heating to the desired temperature with a computer controlled thermocouple/heating coil system. Both solutions of the complex and solvent blanks were recorded at temperature ranging from 20 to -80 °C to ensure accurate solvent subtraction. To obtain the integrated spectral areas for the exchanging species, spectral curve fitting was carried out in MATLAB (version 9.1.0.44655). The ν(CO) bands were fit by constraining three Gaussian functions 4 cm^{-1} centered around 1940, 1960, and 1980 cm^{-1} for all temperatures, while fixing a fourth Gaussian centered at 1920 cm^{-1}.

4.2.3   UV/visible Data Collection and Analysis

Cryostatic UV-visible spectra were collected on a Shimadzu UV-3600 UV/vis/NIR spectrometer, using the same cell setup described above for FTIR data collection. Samples were contained in SPECAC sealed liquid FTIR cells with CaF_2 crystal optic windows and a path length of 1.12 mm. Spectral curve fitting was carried out in MATLAB (version 9.1.0.44655).

4.2.4   Density Functional Theory Analysis

Calculations were performed in the ORCA software suite (version 3.0.3) at the BP86 level of theory with the RIJCOSX approximation.[147–151] Ruthenium, phosphorous, sulfur, and oxygen atoms were treated with the DEF2-TZVP/J basis sets while DEF2-SVP/J was used for all other atoms.[152–160] Dispersion corrections were applied using the atom-pairwise dispersion

correction with a Becke-Johnson damping scheme (D3BJ) and solvation was accounted for using the COSMO solvation model in methylene chloride.[161–163] Analytical frequency calculations were performed at the same level of theory and molecular graphics were performed with the UCSF Chimera package.[164]

4.2.5   NMR Data Collection and Analysis

^{1}H NMR spectra were recorded on a JEOL 500 MHz NMR spectrometer and analyzed using iNMR software. A total of 64 scans of 32768 data points were collected from from -185 to 185 ppm. [31]P spectra were recorded in predried dichloromethane-d2 solutions from 25 to -80 °C.

4.2.6   Obtaining Chemical Exchange Rate Constants from Time Dependent 2D IR Spectra

2D IR spectra were collected in pump-probe geometry.[116, 117] 2D IR experimental setup, data collection and analysis is described in details in Section 3.1
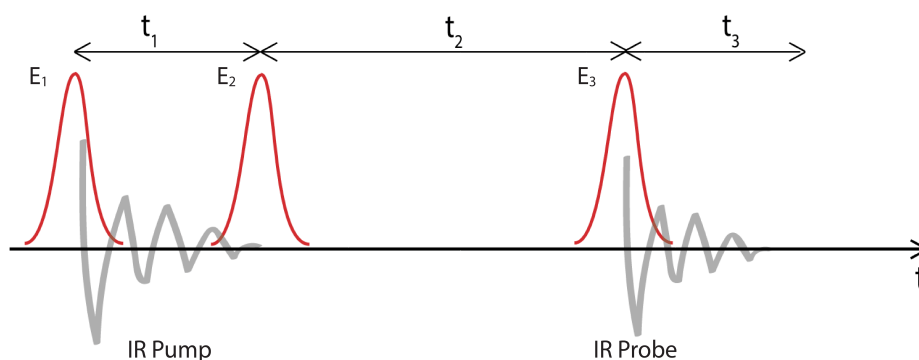
Figure 4.3: Pulse sequence used in 2D IR experiment.

The volume of each peak with respect to t_2 was obtained from the t_2-dependent 2D IR spectra.[27, 32] As shown in Figure 4.5, multiple Gaussian functions were used to fit the 2D IR spectral cut along the probe axis at the peak 2 frequency ($\approx 1940 \text{ cm}^{-1}$) on the pump axis. All

2D IR spectra at different t_2 times were fit following the same method. Each Gaussian function represents one species in the 2D IR spectrum. For example, at $t_2 = 0$ ps, the single Gaussian was used to fit the positive peak of the spectral cut corresponding to the fundamental transition of diagonal peak 2. Similarly, at $t_2 = 25$ ps, three Gaussians were needed to account for the cross peaks resulting from chemical exchange. Peak volumes for each species were obtained from the Gaussian fitting parameters, assuming a circular 2D Gaussian distribution for each peak component. In the generalized transition of a species A to B, the lower corner cross peak of the diagonal peak ratios in the 2D IR spectrum can be expressed as functions of t_2, as shown in Eq. 4.1.[22] The sum of the rate constants of a transition ($k_{for} + k_{rev}$) was directly obtained from fitting $S_{crosspeak}$ / $S_{diagonalpeak}$ with respect to t_2. Given the K_{eq} from VT-FTIR data (in Table 4.1), k_{for} and k_{rev} can be calculated separately (Figure 4.6).

$$\frac{S_{BA}}{S_{AB}} = \frac{1 - e^{-(k_{AB}+k_{BA}) \cdot t_2}}{1 + \frac{k_{AB}}{k_{BA}} \cdot e^{-(k_{AB}+k_{BA}) \cdot t_2}} = \frac{1 - e^{-k_{sum} \cdot t_2}}{1 + K_{eq(A \leftrightarrow B)} \cdot e^{-k_{sum} \cdot t_2}} \tag{4.1}$$

4.3   Results and Discussion

The 2D IR spectra of $Ru(S_2C_2(CF_3)_2)(CO)(PPh_3)_2$ are shown in Figure 4.4. The spectra are essentially 2D frequency correlation maps of vibrational coherences, which are plotted against the initially tagged pump frequency, along the y-axis, and the probe frequency, along the x-axis. On the diagonal (Figure 4.4, dashed line), we observe three individual peaks for $Ru(S_2C_2(CF_3)_2)(CO)(PPh_3)_2$ in DCM solution at $t_2 = 0$ ps, labeled as peak 0 (1980 cm^{-1}), peak 1 (1960 cm^{-1}), and peak 2 (1940 cm^{-1}). The three diagonal peaks indicate three different $\nu(CO)$ modes in the system. The 1960 and 1940 cm^{-1} peaks correspond to the two isomers (**1** and **2**, respectively) as previously observed in the solid state FTIR spectra. The third $\nu(CO)$ band at 1980 cm^{-1} corresponds to a third isomer of the ruthenium complex **0** that was not isolable in the solid state, and appears only as a small shoulder in solution phase FTIR spectra. The third isomer has

been determined to be a metastable trigonal bipyramidal structure of $Ru(S_2C_2(CF_3)_2)(CO)(PPh_3)_2$ (vide infra).
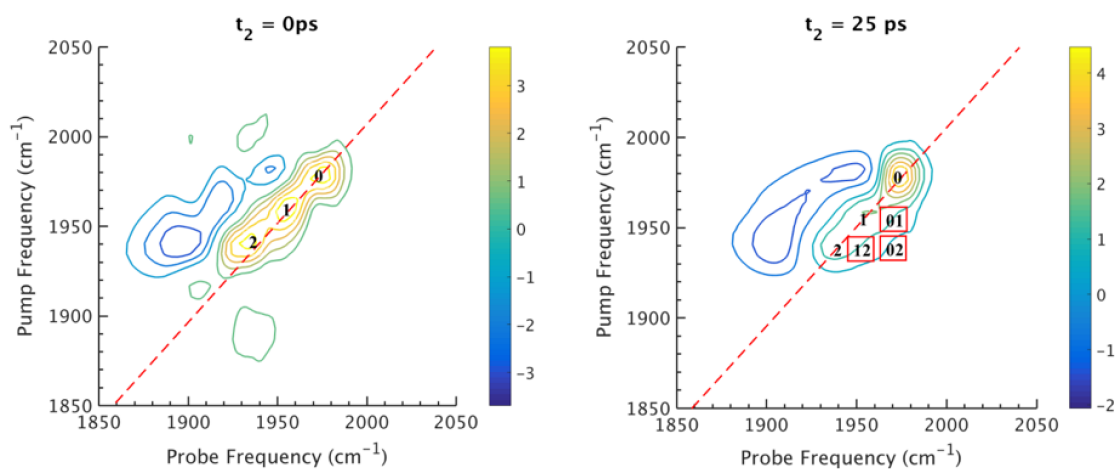
Figure 4.4: (left) 2D IR spectrum at $t_2 = 0$ ps. Peaks 0, 1, 2 are diagonal peaks that lie along dashed diagonal line. (right) 2D IR spectrum at $t_2 = 25$ ps. Red boxes indicate locations of corresponding cross peaks. For instance, 01 is a cross peak that corresponds to population transfer from 1 to 0.

The dynamics between the three isomers are revealed by 2D IR spectra collected at a series of t_2 time delays. As t_2 increases, the three diagonal peaks decay due to population relaxation of the vibrational modes, while cross peaks increase relative to the diagonal peaks (Figure 4.5). Cross peaks in the 2D IR represent chemical exchanges between the species appearing on the diagonal, at peaks 0, 1, and 2. For instance, a cross peak located at the pump frequency of **1** and the probe frequency of **0**, indicates exchange between isomers **1** and **0**. Chemical exchange time constants between each isomer are extracted by fitting cross peak intensities at different t_2 times and plotting them as a function of t_2. (Figure 4.6). The extracted time constants indicate that the transition from **1** to **0** occurs with a 4.3 (1.5) ps time constant, while the transition from **0** to **2** requires 6.3 (1.6) ps. A cross peak for the conversion of **1** to **2** was also observed with a time constant of 8.6 (2.0) ps;

29
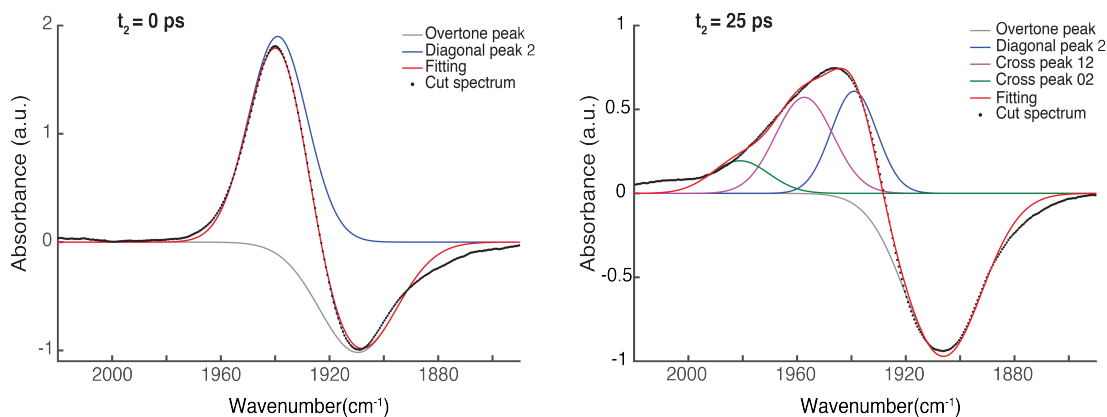
Figure 4.5: (Left) Cut $t_2 = 0$ ps 2D IR spectrum along probe axis at peak 2 on pump axis. Two Gaussian functions were used to fit the spectrum; (Right) Cut $t_2 = 25$ ps 2D IR spectrum along probe axis at peak 2 on pump axis. Four Gaussian functions were used to fit the cut spectrum.
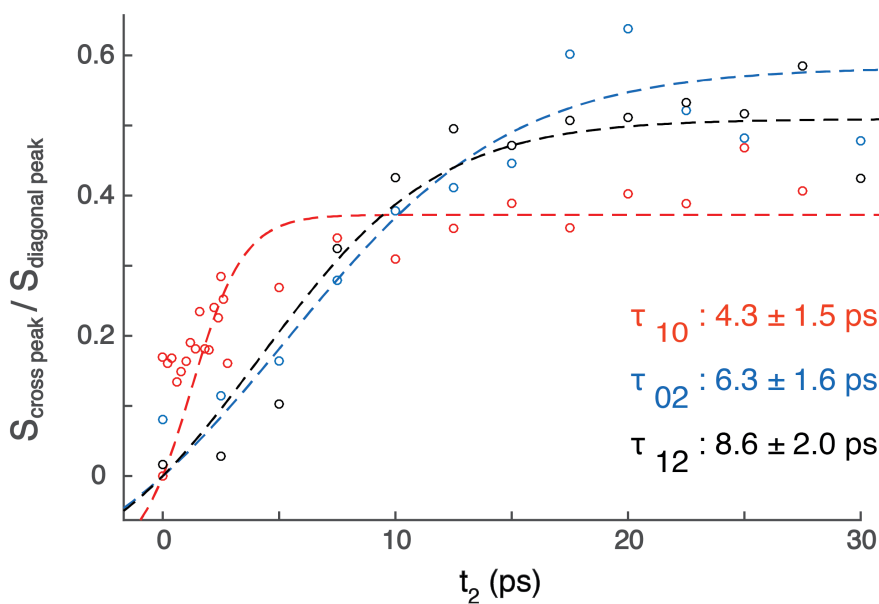
Figure 4.6: (left) Cross peak ratios at varies t_2 time delays. Dots are experimental results; dashed lines are experimental results fitted to chemical exchange model. Time constant of each dynamic exchange process is extracted from the increasing cross peak ratio over t_2.

We note that spectral diffusion could be another source of lineshape change that manifests as an off-diagonal component growth.[113, 134, 135, 140, 141] For $Ru(S_2C_2(CF_3)_2)(CO)(PPh_3)_2$ in DCM, spectral diffusion was observed separately with a time constant 83.3 (15.3) ps, which is much longer than the cross peak intensity growth, indicating that the cross peak dynamics
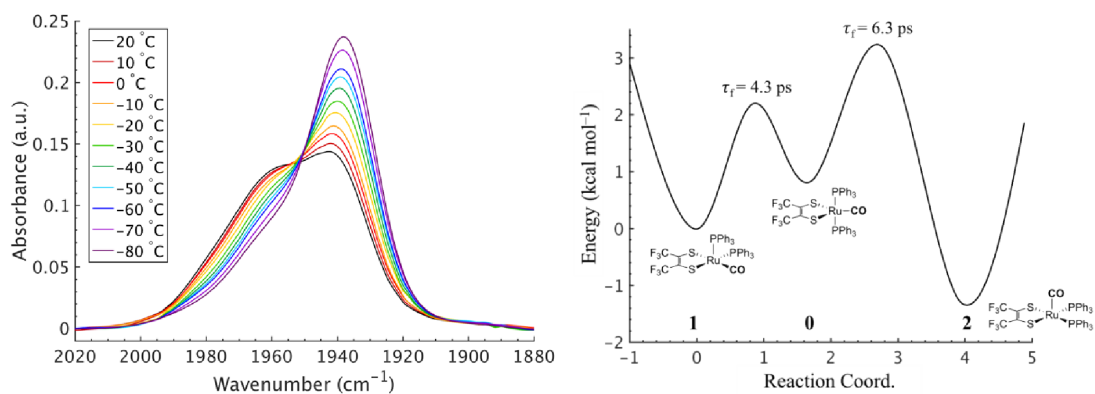
Figure 4.7: (left) VT-FTIR of $Ru(S_2C_2(CF_3)_2)(CO)(PPh_3)_2$ in DCM from 20 to -80 °C. (right) Qualitative potential energy surface for the presented isomerization reaction. Energy surface was constructed using the experimental kinetic and thermochemical data obtained from 2D IR and VT-FTIR.

reflect chemical exchange.[165] It is also important to note that the power of the mid-IR pulses interacting with the system is insufficient to perturb the system from thermal equilibrium, and does not drive the system away from a persistent steady-state population. The IR pulse sequence serves only to tag and probe the vibrational modes at different time delays. This allows the observation of the intramolecular rearrangement of interest under thermal equilibrium.

To investigate the thermodynamics of the chemical exchange process observed here, the variable temperature 1D FTIR (VT-FTIR) spectra of the complex was collected using a SPECAC flow-through optical cryostat. The sample was enclosed in a CaF_2 crystal windowed sample cell contained in a vacuum jacketed housing and cooled from 20 to -80 °C using a methanol liquid nitrogen slurry. Upon cooling, the broad band centred at ca. 1958 cm^{-1} shifts to lower frequencies (ca. 1938 cm^{-1}), sharpens and gains intensity while the shoulders near 1960 and 1980 cm^{-1} significantly lose intensity (Figure 4.7). The temperature dependence is completely reversible and suggests that at low temperature, DCM solutions contain predominantly the more favoured CO_{apical} isomer, **2**. After solvent subtraction, the 1D FTIR line shapes were fit to three Gaussian functions centred about the equilibrium positions for each isomer (Figures 4.8-4.9, $\nu(CO) \approx$ **0**:
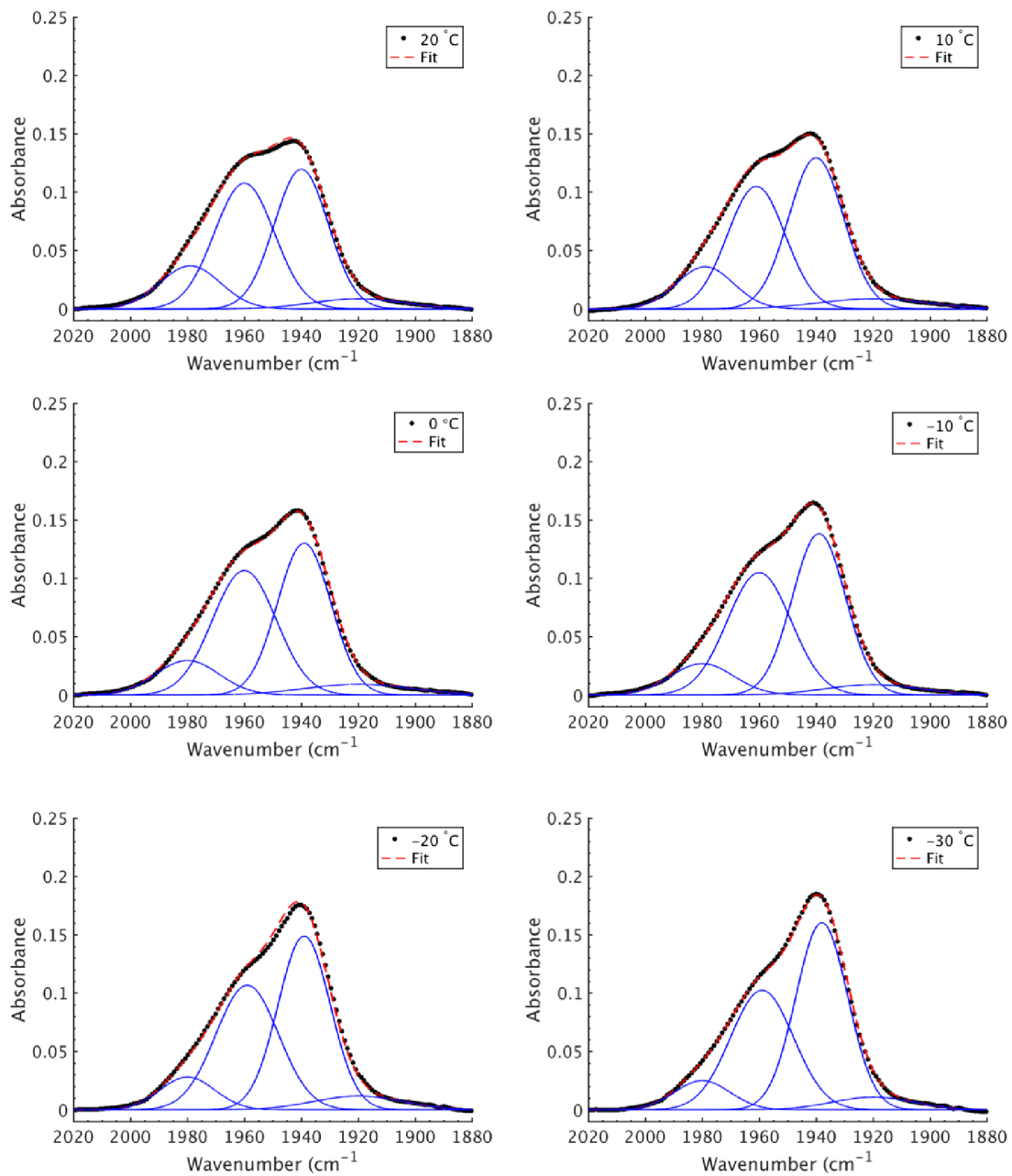
Figure 4.8: VT-FTIR fits of ν(CO) bands for 0 (1980 cm^{-1}), 1 (1960 cm^{-1}), and 2 (1940 cm^{-1}) isomers ranging from 20 to -30 °C in DCM. Black traces are experimental data while the red traces are the sum of the Gaussian functions use to fit the ν(CO) bands.
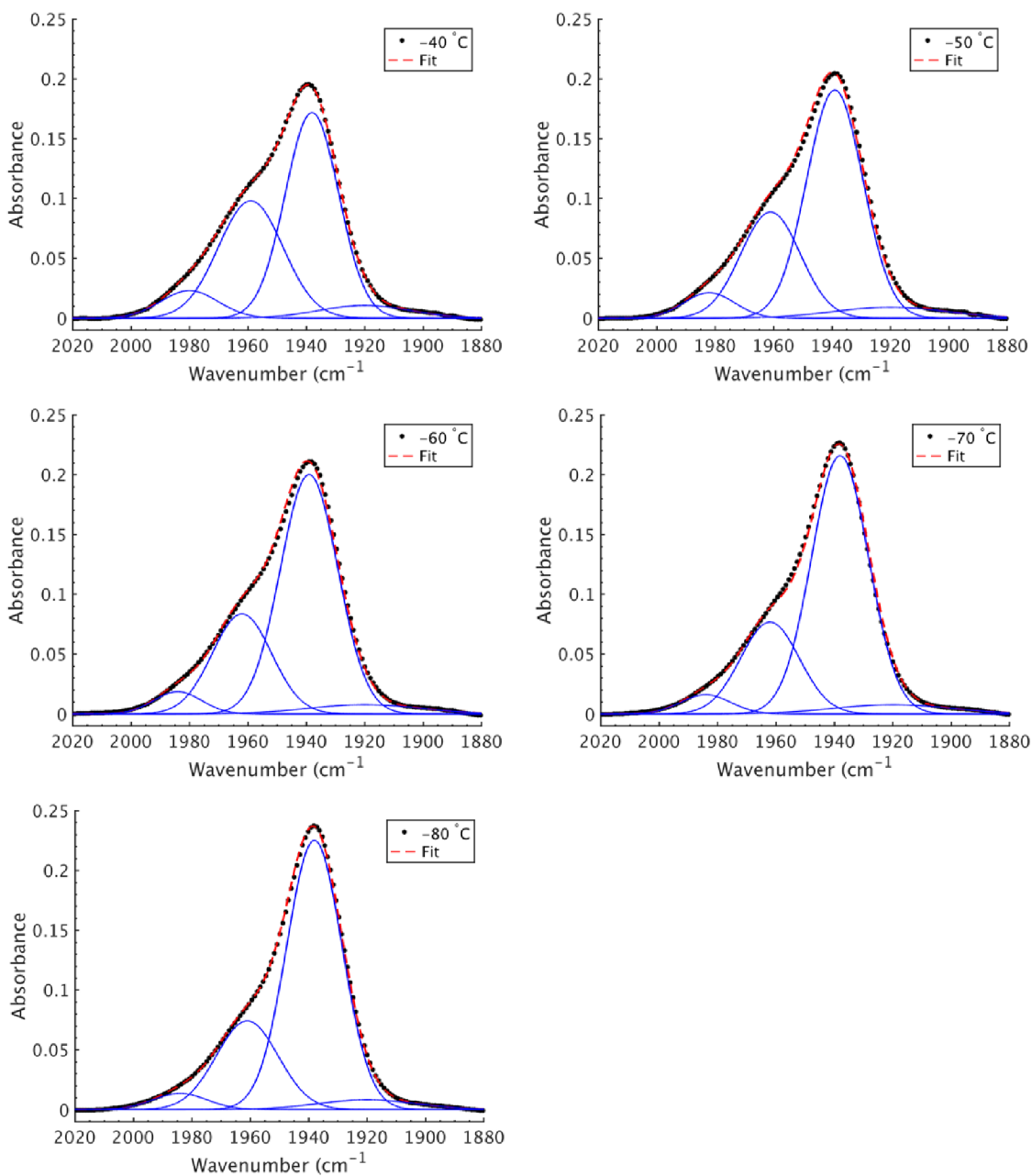
Figure 4.9: VT-FTIR fits of ν(CO) bands for 0 (1980 cm^{-1}), 1 (1960 cm^{-1}), and 2 (1940 cm^{-1}) isomers ranging from -40 to -80 °C in DCM. Black traces are experimental data while the red traces are the sum of the Gaussian functions use to fit the ν(CO) bands.
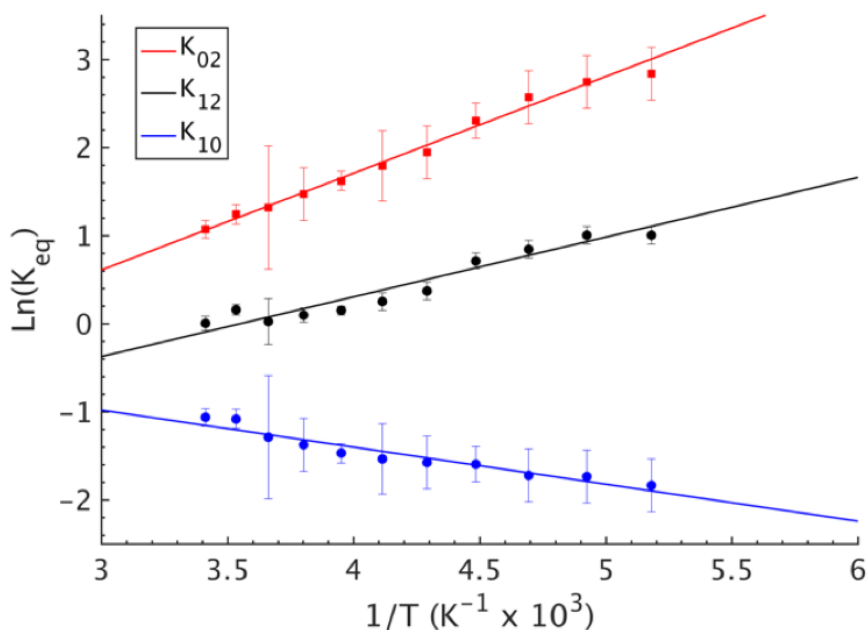
Figure 4.10: Plot of Ln(K_{eq}) vs. 1/T for the isomerization reaction. K_{10} represents the equilibrium constant for exchange between 1 and 0, K_{02} represents the equilibrium constant for exchange between 0 and 2, and K_{12} represents the equilibrium constant for exchange between 1 and 2.

1980 cm^{-1}, **1**: 1960 cm^{-1}, **2**: 1940 cm^{-1}) and allowed to move ±4 cm^{-1}. Using the determined spectral areas, the population ratios of the isomers at all temperatures were then determined and a Van't Hoff analysis was performed (Figure 4.10). Exchange between **1** and **0** was found to be endergonic in nature with ΔH = 0.84 (0.08) kcal mol^{-1}, ΔS = 0.6 (0.4) eu, and ΔG^{298} = 0.7 (0.1) kcal mol^{-1}, while exchange between **0** and **2** was found to be exergonic with ΔH = -2.18 (0.06) kcal mol^{-1}, ΔS = -5.3 (0.3) eu, and ΔG^{298} = -0.6 (0.1) kcal mol^{-1}. The exchange process overall from **1** to **2** (CO$_{equitorial}$ to CO$_{apical}$) was found to be thermodynamically favoured in DCM with ΔH = -1.3 (0.1) kcal mol^{-1}, ΔS = -4.8 1 (0.5) eu (Table4.1). While the direct exchange between **1** and **2** is possible, given literature precedent, the kinetic analysis and DFT results (vide infra) all exchange is believed to involve the TBP intermediate (**0**) (Figure 4.7).[166, 167]

It is important to note that since both the equilibrium constant and the rate constant for exchange will contribute to the overall FTIR lineshape it is useful to determine the equilibrium

constants for the isomers independently. This was done by variable temperature UV-visible electronic spectroscopy. Electronic spectra of the solid state isomers in a KBr pellet present a single transition for the orange isomer (**2**) at 466 nm while the violet isomer (**1**) presents three transitions at 571 nm, 460 nm, and 396 nm (Figure 4.11). In DCM solutions at 20 °C three transitions are present with band maxima at 386, 466 and 561 nm. Upon cooling to -80 °C, the bands at 386 and 561 nm are seen to decrease in intensity while the band at 470 gains significant intensity and blue shifts to 455 nm (Figure 4.12). The bands are assigned to the equatorial (**1**) and apical (**2**) isomers respectively and both are related by clear isosbestic points at 396 and 490 nm indicative of absorbing species in equilibrium. After spectral deconvolution (Figure 4.13-4.14), the equilibrium constants were estimated from the spectral areas and a Van't Hoff analysis gave a ΔH (0.06) kcal $^{-1}$ and ΔS = -3.4 (0.2) eu (Figure 4.15). These values are in excellent agreement with those determined from the analysis of 1D FTIR spectra described above.
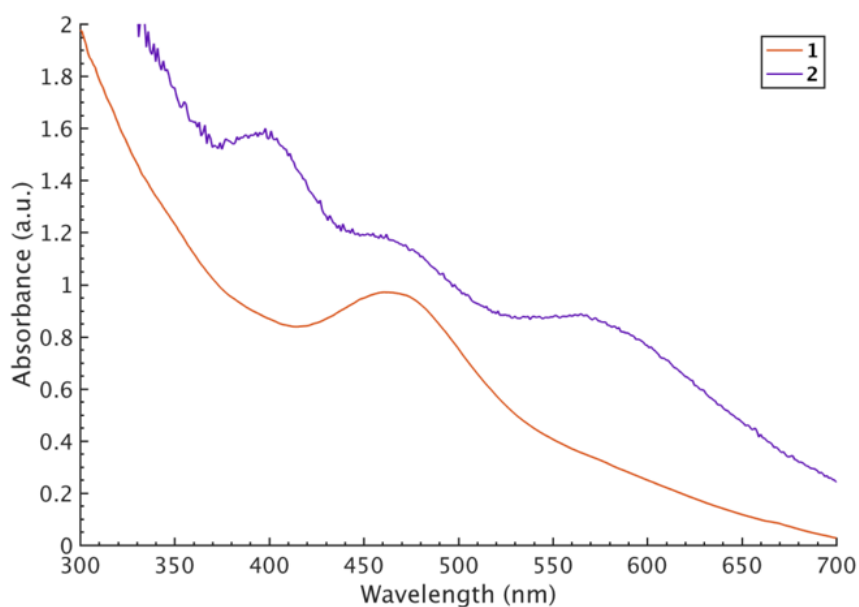
Figure 4.11: Solid state UV/vis spectroscopy taken in a KBr pellet. The orange isomer has a single absorbance maximum at 466 nm, while the violet isomer has three absorbance maxima at 396, 460, and 571 nm.

The most closely related examples of transition metal complexes undergoing dynamic ex-
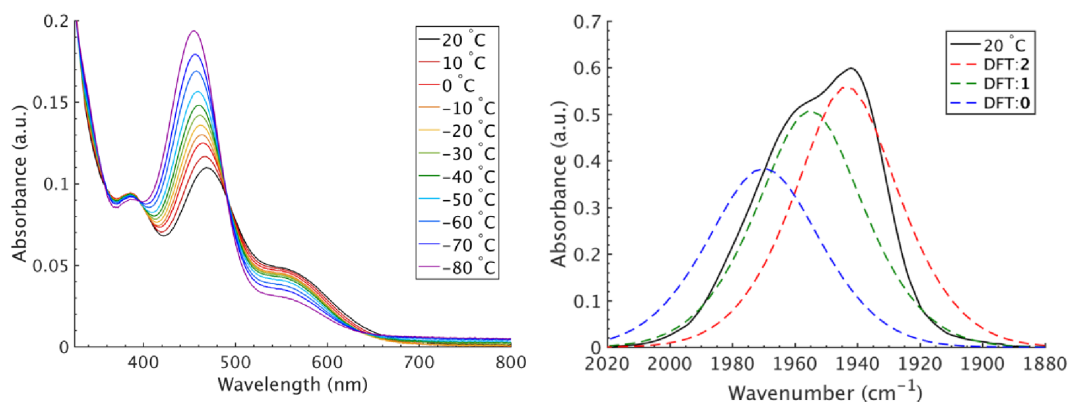
Figure 4.12: (left) VT-UV/vis spectroscopy in DCM ranging from 20 to -80 °C. The absorbance maximum at 470 nm is attributed to the apical isomer (2) while the maxima at 385 and 561 nm are attributed to the equatorial isomer (1). (right) Experimental FTIR and predicted IR from DFT calculation.

change on the IR timescale can be found in both $[(\eta^4\text{-diene})Fe(CO)_3]$ complexes and $Co_2(CO)_8$. [133] In the former $[(\eta^4\text{-diene})Fe(CO)_3]$ complexes, the three carbonyl ligands exchange through a very low barrier, turnstyle type, Berry pseudorotation.[122, 124, 168–171] This corresponds to a degenerate self-exchange, quite different from the exchange between populations of two structurally different isomers, sharing an observable intermediate as observed in both $Ru(S_2C_2(CF_3)_2)(CO)(PPh_3)_2$ (vide supra) and $Co_2(CO)_8$.[133] An Arrhenius analysis (Eq. 4.2) provides the barrier heights of the observed exchange process.

$$k = Ae^{\frac{-E_a}{RT}} \tag{4.2}$$

Using the determined rate constants from 2D IR and an estimate of the exponential prefactor (A) to be on the order of 10^{13} s^{-1},[122, 124, 139, 168, 169] the barrier to exchange from **1** to **0** was found to be 2.2 (0.2) kcal mol^{-1}, while the barrier to exchange from **0** to **2** was found to be 2.4 (0.1) kcal mol^{-1} (Table 4.1, Figure 4.7). These values are sufficiently low to be expected to produce the dynamic exchange coalesced lineshapes, like those observed in the 1D FTIR spectra.[124, 169] We also note that careful examination of the structures and application of simple principles of least motion would predict that isomerization between **1** and **0** would
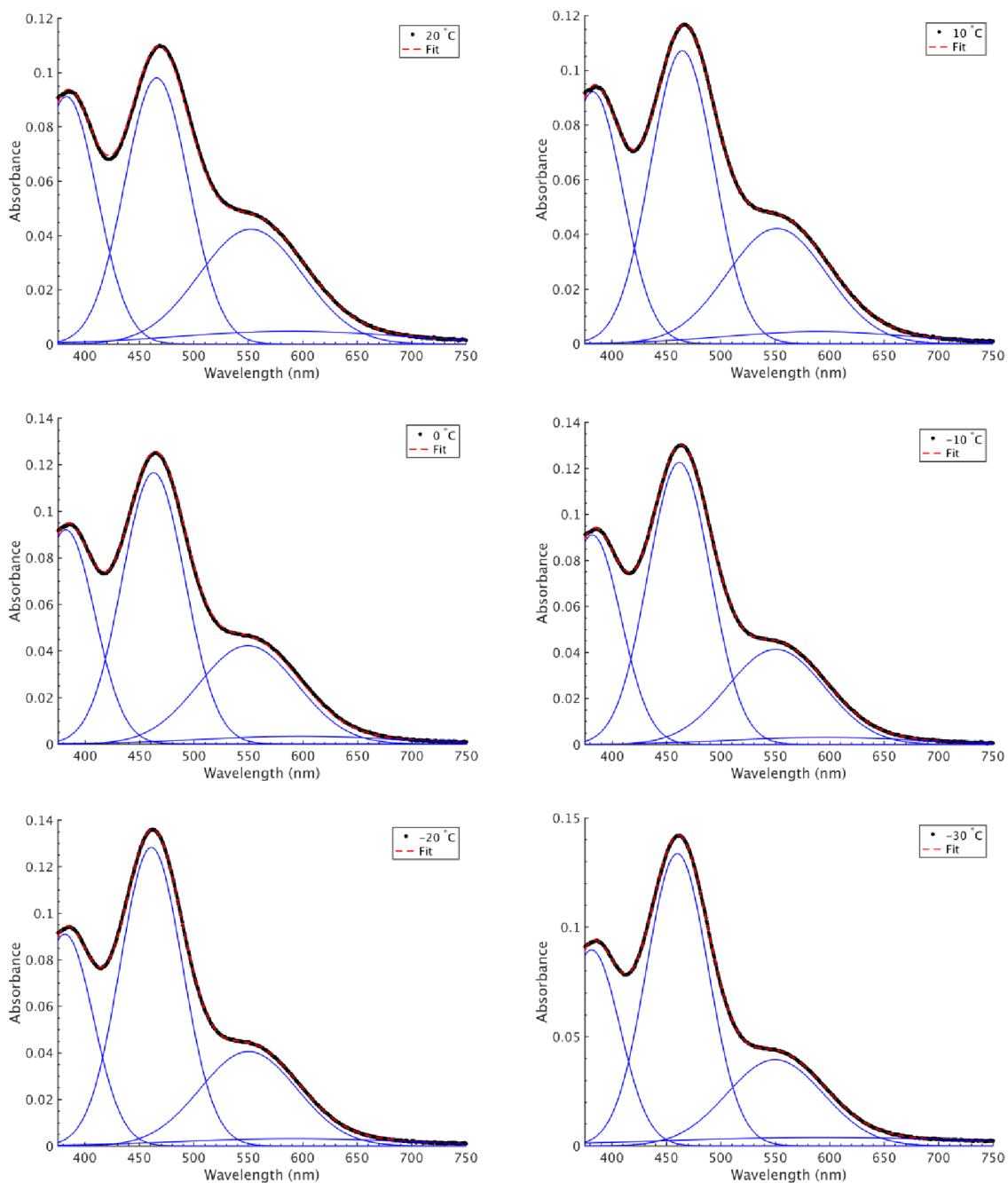
Figure 4.13: VT–UV/vis fits of 1 (385 and 561 nm), and 2 (470 nm) ranging from 20 to -30 °C in DCM. Black traces are experimental data while the red traces are the sum of the Gaussian functions use to fit the absorbance bands.
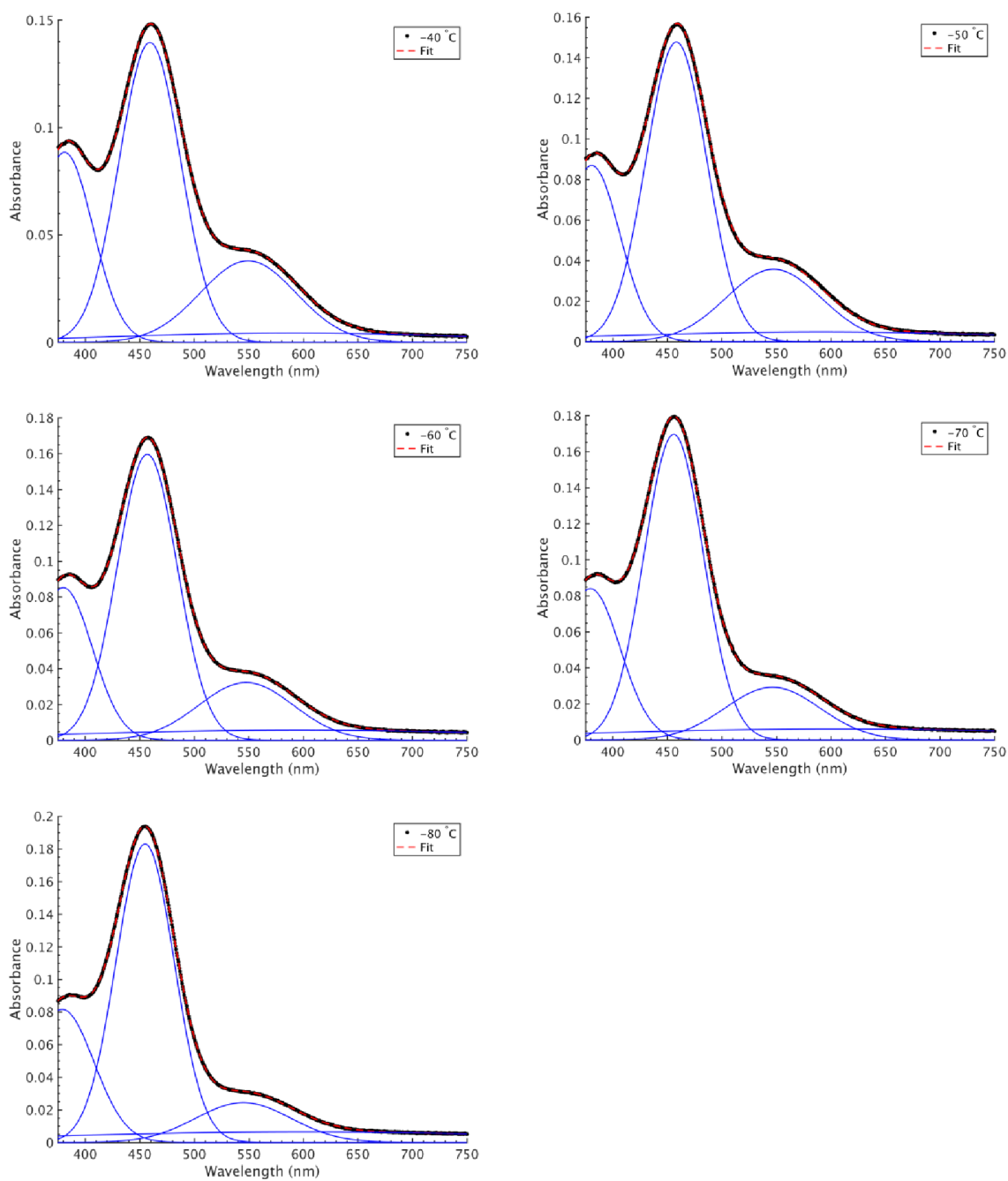
Figure 4.14: VT–UV/vis fits of 1 (385 and 561 nm), and 2 (470 nm) ranging from -40 to -80 °C in DCM. Black traces are experimental data while the red traces are the sum of the Gaussian functions use to fit the absorbance bands.
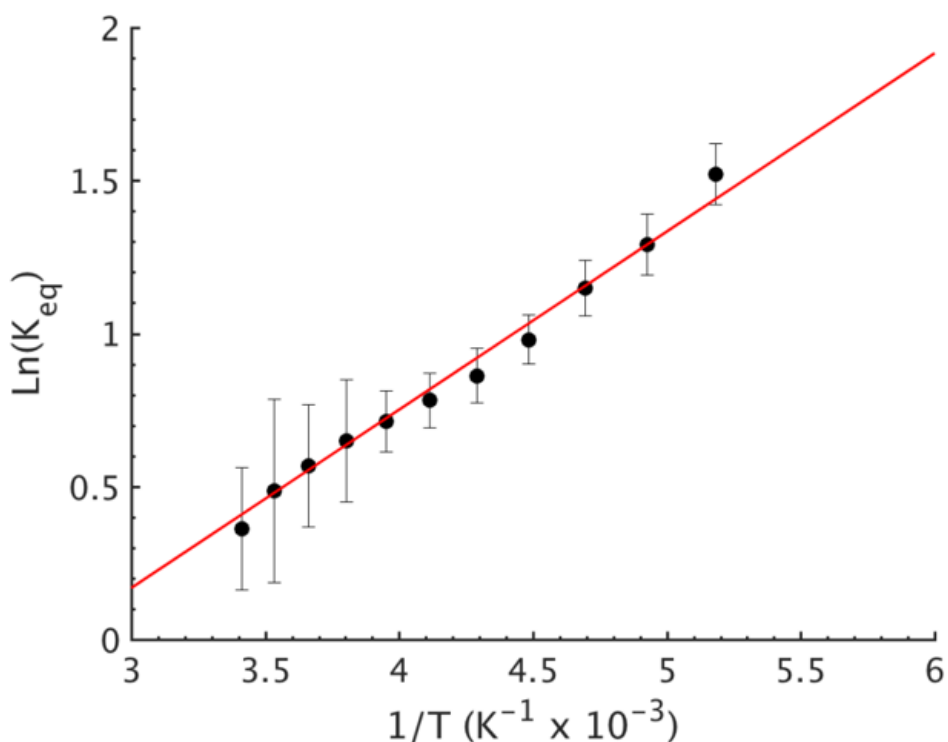
Figure 4.15: Plot of $Ln(K_{12})$ vs 1/T as obtained from UV/vis spectral analysis. ΔH and ΔS were found to be -1.21 kcal mol^{-1} (0.04) and -3.4 (0.2) eu respectively.

require less rearrangement than that required to proceed between **0** to **2**, consistent with the experimentally determined barriers.

The isomers are believed to exchange from **1** to **0** by movement of a phosphine ligand in **1** from an equatorial to axial position (Figure 4.7). Isomerization between **0** and **2** then occurs following twisting the dithiolene ligand in **0** to place the dithiolene ligand in the equatorial plane. Calculated structures and frequency calculations were obtained using density functional theory (DFT) at the BP86 level of theory with basis sets def2-TZVP (Ru, S, P, and O) and def2-SVP (H and C) for the isolated molecules. The reported crystal structure data for **1** and **2** were used for the initial geometries,[172, 173] while the TBP (**0**) isomer was adapted from the reported crystal structure of **1**. After geometry optimization, frequency calculations were performed at the same level of theory to verify optimized geometries as minima. The predicted FTIR spectrum from

Table 4.1: Equilibrium, exchange constants, and thermochemical data at 20 °C in DCM.

	K_{eq}	ΔH (kcal/mol)	ΔS (eu)	τ_f (ps)	E_a (kcal/mol)
IR	K_{10} = 0.35 (0.03)	0.84 (0.08)	0.6 (0.4)	4.3 (1.5)	2.2 (0.2)
	K_{02} = 2.9 (0.2)	-2.18 (0.06)	-5.3 (0.3)	6.3 (1.6)	2.4 (0.1)
	K_{12} = 1.0 (0.1)	-1.3 (0.1)	4.8 (0.5)	8.6 (2.0)	2.6 (0.1)
UV-vis	K_{12} = 1.4 (0.3)	-1.3 (0.1)	-3.4 (0.2)	—	—

the DFT frequency calculation was in excellent agreement with that observed experimentally (Figure 4.12, ν(CO) DFT: **0** = 1975 cm^{-1}; **1** = 1955 cm^{-1}; **2** = 1940 cm^{-1}) supporting the experimental observation of the TBP isomer. These ideas of isomerization are further supported by consideration of the vibrational normal modes as calculated from the DFT frequency analysis.

4.4   Conclusions

The fact that a relatively large transition metal complex undergoes isomerization at rates comparable to the rotational isomerization reactions of small organic molecules is surprising.[33, 125, 139, 174] To our knowledge, this is the first observation of an ultrafast dynamic equilibrium involving two distinct structural isomers and the intermediate connecting them. This work confirms that the ground states of five-coordinate transition metal complexes can have remarkably low kinetic barriers for axial-equatorial exchange. This study also validates the mechanism of Berry pseudorotation and clearly demonstrates its dynamical time scale. This work presents new opportunities for potential molecular device applications based on switching between three distinct states of a system exhibiting electronic tri-stability on the ps time scale.

Chapter 4, in full, is a reprint of the material as it appears in Chemical Science, 2018. Tyler M. Porter; Jiaxi Wang; Yingmin Li; Bo Xiang; Catherine Salsman; Joel S. Miller; Wei Xiong; Clifford P. Kubiak., Royal Society of Chemistry, 2018. The dissertation author was the primary investigator and author of this paper.

Chapter 5

Conformational Dynamics in Zero-valent CoL$_4$ Complexes Revealed by 2D IR Spectroscopy

5.1   Introduction

Reactive unsaturated organometallic species serve as important intermediates in catalytic reactions. Probing structures and dynamics of these intermediate species is at the heart of understanding the mechanism of catalytic reactions. Despite its importance, it remains challenging to experimentally follow catalytic intermediates. The reasons are two folds: first, unsaturated organometallic species are unstable. Second, there are often ground states that are closely spaced in energy, which makes these intermediates convert at relatively fast time scale and short lived in some cases. Fast dynamic processes cause broadened spectral signatures. As a result, it can be challenging to extract useful structural and dynamics information of intermediates by spectroscopic techniques without ultrafast time resolution.

Despite 2D IR has been widely used to study dynamics of organometallics,[133, 134,

136, 175, 176] there is little progress in studying unstable species, here we focus on studying an analogue of $Co(CO)_4$, which is not only an important intermediate of hydroformylation and hydrogenation catalysis, but also a great example of challenges in organometallic catalytic research discussed in the paragraph above.[177–188] $Co(CO)_4$ is a well-known, short lived $S = 1/2$ metalloradical observed only in low temperature matrices, known to be generated by Co-Co bond homoleptic cleavage from $Co_2(CO)_8$ through Co-Co bond homoleptic cleavage.[189, 190] Its geometric/electronic structures have been long debated due to near-thermoneutral nature of its C_{3v} and D_{2d} ground states.[191] So far, these species have been well studied by static spectroscopic methods under cryogenic or gas phase conditions, which have concluded that the method of observation directly affects the geometric preference.[189, 192–195] These studies, coupled with computational evidence, have indicated that there exists fast exchange between isomers. However, this exchange has never been observed under ambient conditions (or those related to catalysis) in a direct, time resolved manner. With the advent of both kinetically stabilized model complexes of $Co(CO)_4$ and ultrafast time-resolved 2D spectroscopic techniques, the question of dynamic conformational changes in such reactive species can now be directly interrogated.

The tetraisocyanide complex, $Co(CNAr^{Mes2})_4$ (Ar^{Mes2} = 2,6-$(2,4,6-Me_3C_6H_2)_2C_6H_3$), serves as a crystallographically characterized, thermally stable isocyano analogue of the reactive binary carbonyl $Co(CO)_4$.[196, 197] Through our recent studies,this compound mimics well the electronic structure of $Co(CO)_4$ due to the isolobal analogues between carbomonoxide (CO) and isocyanides (CNR).[196, 198–204] A combination of static X-ray crystallography, EPR and FTIR experiments suggested that more than one conformation of $Co(CNAr^{Mes2})_4$ could be observed, however, the evidence lead to interconversion between such conformations was not conclusive. For example, temperature dependent X-ray crystallographic collections show that slight geometry distortion occurs at different temperatures, which indicates the possible dynamic feature in $Co(CNAr^{Mes2})_4$.

2D IR spectroscopy provides an avenue to visualize this kinetic process. 2D IR spec-

troscopy is a time resolved technique that can follow chemical exchange occurring from hundreds of femtosecond to picosecond time scales. The 2D IR pulse sequence labels and probes vibrational modes before and after a waiting period t_2, respectively. (Figure 5.3b). Therefore, any changes occurred during t_2 are encoded in vibrational bands that are studied. Furthermore, because vibrational modes in organometallic compounds are mostly local, by selectively probing vibrational modes that are near the metal center, dynamics around metal center can be tracked, which is mostly relevant to catalytic intermediates of interests. These unique advantages make 2D IR uniquely useful to resolving conformations and following structural dynamics of organometallic compounds and other molecules. While the combination of kinetically stable analogues of $Co(CO)_4$ and ultrafast 2D IR can potentially shed light of the unknown conformation exchanges of the catalytic intermediates, it is an open question on whether the bulky ligands in $Co(CNAr^{Mes2})_4$ would slow down its dynamics away and do not mimicking $Co(CO)_4$.

5.2 Methods

5.2.1 Synthesis Procedures

All manipulations were carried out under an atmosphere of dinitrogen using standard Schlenk and glovebox techniques.[205] Unless otherwise stated, reagent grade starting materials were purchased from commercial sources and either used as received or purified by standard procedures. Solvents were dried and deoxygenated according to standard procedures.[206] Benzene-d_6 and Toluene-d_8 were dried with Na/K and Benzophenone followed by distillation and stored on molecular sieves (4 Å) for 3 days prior to use. The compounds $Co(CNAr^{Mes2})_4$ and $Co(CNtBu)(CNAr^{Mes2})_3$ were prepared by previously reported methods.[196]

5.2.2 FTIR Experiemnts, Data Collection, and Analysis.

FTIR of $Co(CNAr^{Mes2})_4$ and $Co(CNtBu)(CNAr^{Mes2})_3$. All spectra were recorded on a Thermo-Nicolet iS10 FTIR spectrometer. Samples were prepared as solutions injected into a Thermo-Fisher solution cell equipped with KBr windows. For solution FTIR spectra, solvent peaks were digitally subtracted from all spectra by comparison with an authentic spectrum obtained immediately prior to that of the sample.

VT-FTIR of $Co(CNAr^{Mes2})_4$ and $Co(CNtBu)(CNAr^{Mes2})_3$. Variable temperature infrared spectra were collected on a Bruker Equinox 55 FTIR spectrometer using a SPECAC flow through optical cryostat (model, 21525) with a 1.12 mm path length (determined from infringing pattern), CaF_2 windowed cell enclosed in a vacuum jacketed housing.

FTIR spectrum at each temperature is fitted with four Gaussian functions, each representing a peak component. The center wavelengths of the Gaussian functions are 2008 ± 2 cm^{-1}, 1960 ± 2 cm^{-1}, 1936 ± 2 cm^{-1}, and 1916 ± 2 cm^{-1}.

5.2.3 Obtaining Chemical Exchange Rate Constants at Different Temperature from 2D IR

2D IR spectra were collected in pump-probe geometry.[116, 117] 2D IR experimental setup, data collection and analysis is described in details in Section 3.1

VT-2DIR experiments were taken under 268K, 278K, 288K, 298K, and 308K with the same SPECAC flow through optical cryostat (model, 21525) for VT-FTIR.

To obtain exchange rate constant from 2D IR, the volume of each peak with respect to t_2 was obtained from the t_2-dependent 2D IR spectra.[27, 32] As shown in Figure 5.1, multiple Gaussian functions were used to fit the 2D IR spectral cut along the probe axis at the peak 2 frequency ($\approx$1940 cm^{-1}) on the pump axis. All 2D IR spectra at different t_2 times were fit following the same method. Each Gaussian function represents one species in the 2D IR spectrum.

For example, at $t_2 = 0$ fs, the single Gaussian was used to fit the positive peak of the spectral cut corresponding to the fundamental transition of diagonal peak 2. Similarly, at $t_2 = 900$ fs, three Gaussians were needed to account for the cross peaks resulting from chemical exchange. Peak volumes for each species were obtained from the Gaussian fitting parameters, assuming a circular 2D Gaussian distribution for each peak component. In the generalized transition of a species A to B, the lower corner cross peak of the diagonal peak ratios in the 2D IR spectrum can be expressed as functions of t_2.[22]

$$\frac{S_{BA}}{S_{AB}} = \frac{1 - e^{-(k_{AB}+k_{BA}) \cdot t_2}}{1 + \frac{k_{AB}}{k_{BA}} \cdot e^{-(k_{AB}+k_{BA}) \cdot t_2}} = \frac{1 - e^{-k_{sum} \cdot t_2}}{1 + K_{eq(A \leftrightarrow B)} \cdot e^{-k_{sum} \cdot t_2}} \tag{5.1}$$

Given the Keq from VT-FTIR data, k_{for} and k_{rev} can be calculated separately for each temperature. Based on Erying plot, the forward and reverse activation energy barrier between D_{2d} and C_{3v} can be obtained as 0.5 ± 0.1 kcal/mol and 1.9 ± 0.4 kcal/mol, respectively.

5.2.4   Computational Studies

Computational details. Density Functional Theory (DFT) calculations were carried out on both C_{3v} and D_{2d} geometry of CoL_4 (L = CO, CNMe, CNXyl, $CNAr^{Ar2}$ and $CNAr^{Mes2}$). All C_{3v} calculations were accomplished by freely refined the coordinates. D_{2d} calculations were achieved by starting from the coordinates of $[Ni(CNAr^{Mes2})4]OTf$ molecule which shows D_{2d} geometry in the crystal structure,[207] with constrains at the core angles. Also, calculation on $Co(CNtBu)(CNAr^{Mes2})_3$ was obtained by starting from the crystal structure coordinates. Calculations were all carried out with the Gaussian 09 software package.[208] Geometry optimizations, frequency and single point energy calculations were performed using the B3LYP functional, with the 6-31g(d) basis set for H, C, O and N atoms and the LANL2DZ basis set plus f-type polarization functions for cobalt atoms. Viewing of optimized structures and rendering of molecular
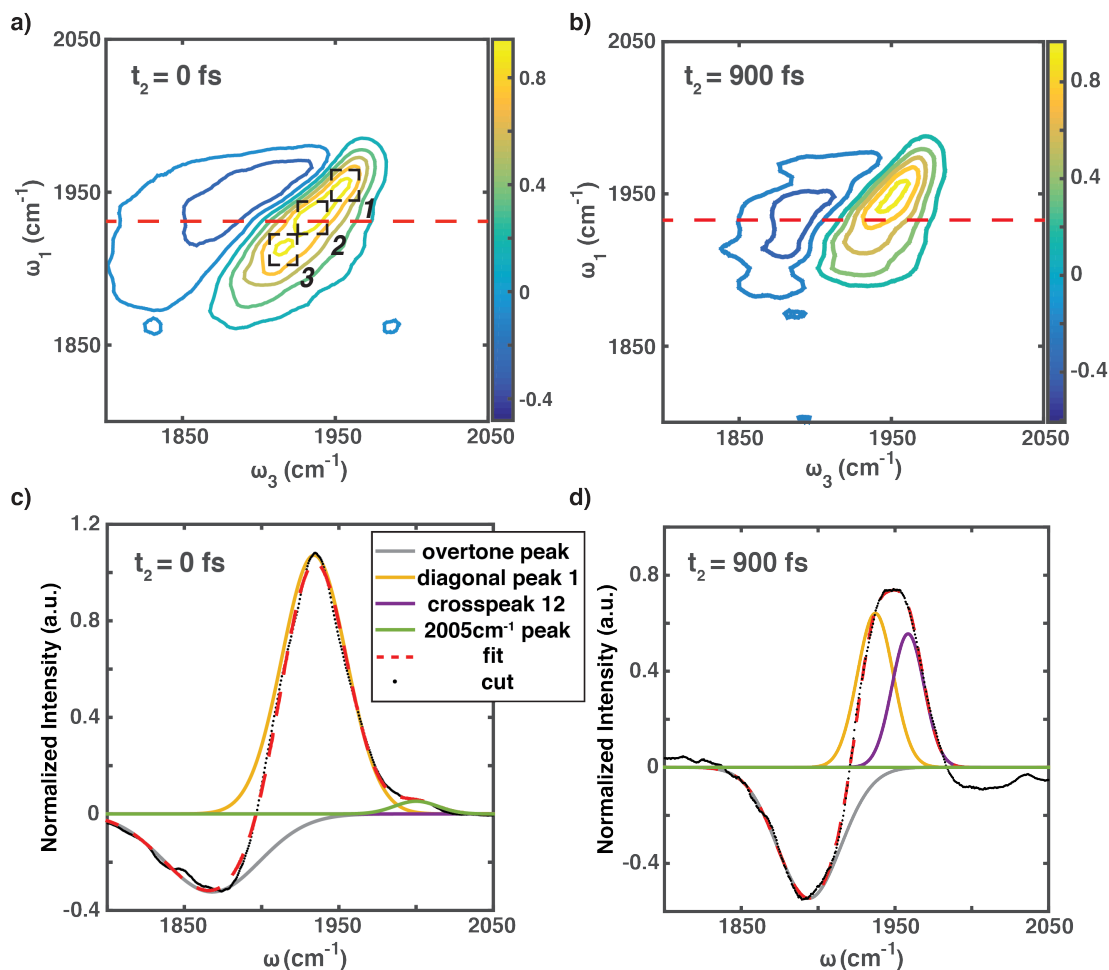
Figure 5.1: 2D IR spectrum at a) t_2=0 fs and b) t_2=900 fs c) take cut along ω_3 axis at red dash line in a) and fit with gaussian peak components d) take cut along ω_3 axis at red dash line in b) and fit with gaussian peak components.

orbitals was performed using the program Chemcraft, see Figure 5.2. The calculated core bond angles of Co(CNAr^{Mes2})$_4$ in D$_{2d}$ and C$_{3v}$ geometries are shown in Table 5.1

Simulated IR studies of fixed core angle geometries. Frequency calculations were carried out on both C$_{3v}$ and D$_{2d}$ geometry of Co(CNAr^{Mes2})$_4$, with two additional geometries for each isomer achieved from twisting the molecule without changing the core angles (C-Co-C). (Figure 5.7 and 5.9) By fixing the core geometry at either C$_{3v}$ or D$_{2d}$, we observed that the outer sphere of the molecule does not affect the isocyanide stretching frequencies (νCN) shown in Figure 5.8 and 5.10. In other words, only the core angles decide the CN vibrations of the molecule.
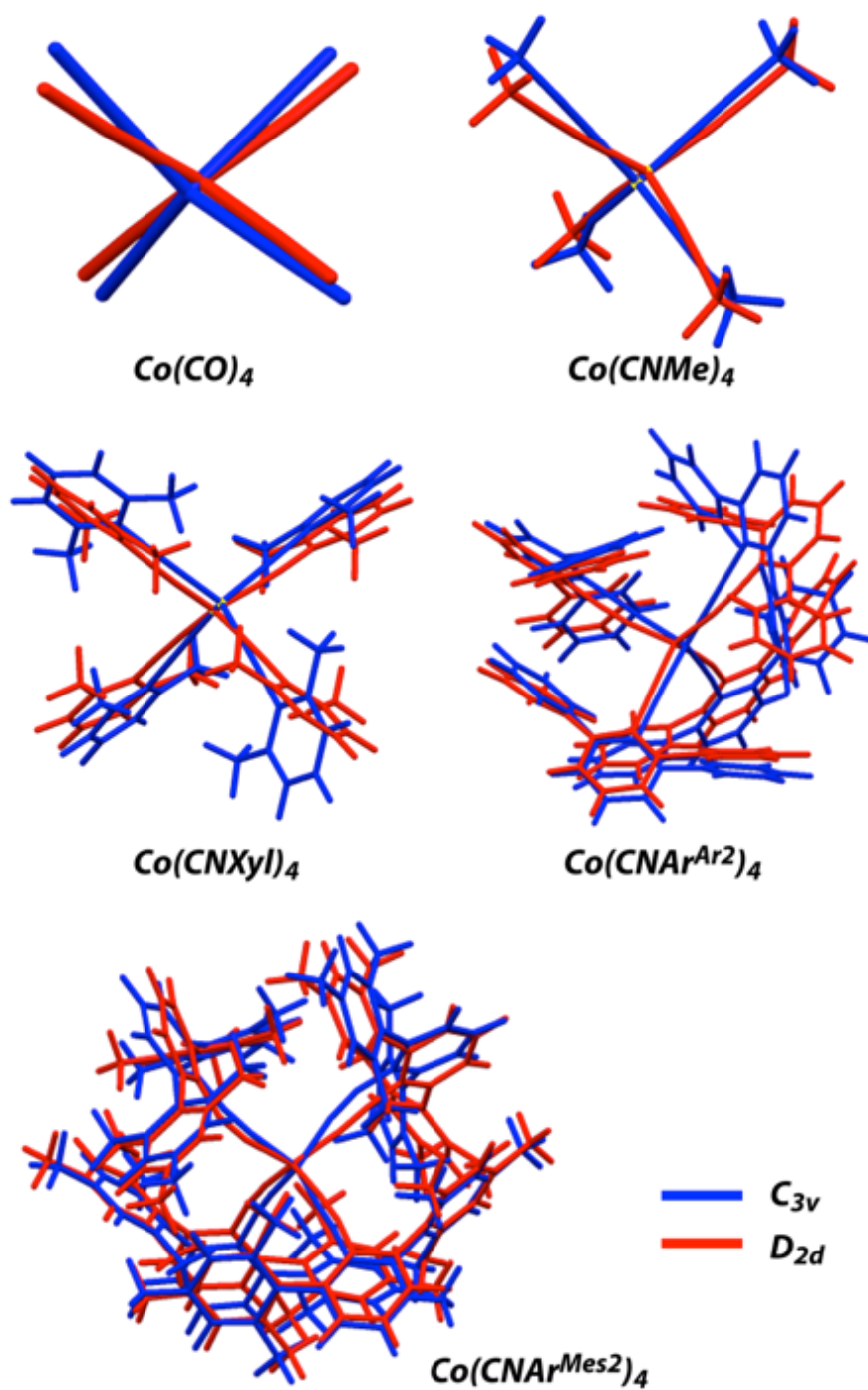
Figure 5.2: Structural overlap images of optimized CoL4 (L = CO, CNMe, CNXyl, CNAr^{Ar2} and CNAr^{Mes2})

Table 5.1: Calculated core bond angles of Co(CNAr^{Mes2})$_4$ in D$_{2d}$ and C$_{3v}$ geometries

Symmetry	Angle	Bond angle (°)
C$_{3v}$	C1-Co-C2	101
	C1-Co-C3	107
	C1-Co-C4	95
	C2-Co-C3	118
	C3-Co-C4	116
	C4-Co-C1	114
D$_{2d}$	C1-Co-C2	130
	C4-Co-C3	125
	C1-Co-C4	104
	C2-Co-C3	103
	C1-Co-C3	97
	C2-Co-4	98

5.3 Results and Discussion

The FTIR spectrum of Co(CNAr^{Mes2})$_4$ shows a broad main peak with lower frequency shoulder at 1940 cm^{-1} plus a separate small peak at higher frequency ($\approx$2005 cm^{-1}) (Figure 5.3d). These peaks correspond to the isocyanide CN vibrations. It is noticeable that the main peak has about 80 cm^{-1} full-width-at-half-max, which is 3-5 times broader than the linewidth of any typical carbonyl or isocyanide vibration peaks. One possible explanation is that this broad

feature contains multiple peaks. In agreement with the statement that both C_{3v} and D_{2d} isomers exist, as indicated from its EPR spectra at 100 K.
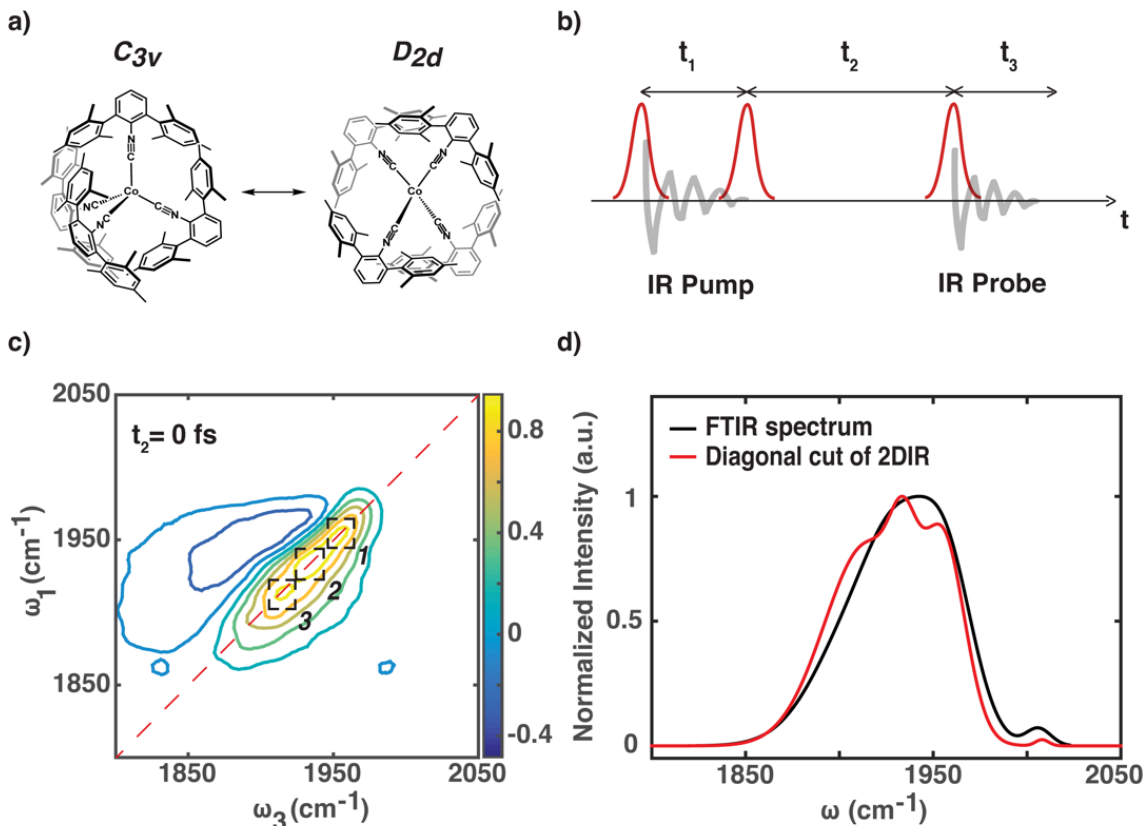
Figure 5.3: a) Molecular Structure of Co(CNAr^{Mes2})$_4$ in D_{2d} and C_{3v} geometries. b) pulse sequence in 2D IR experiment. c) 2D IR spectrum of Co(CNAr^{Mes2})$_4$ at $t_2 = 0$ fs, diagonal peaks labeled as 1, 2, and 3. d) FTIR spectrum (black) of Co(CNAr^{Mes2})$_4$, and diagonal cut of 2D IR spectrum in c) (red).

Indeed, 2D IR spectrum of Co(CNAr^{Mes2})$_4$ shows a clear signature of multiple peaks (Figure 5.3c). This is because 2D IR is proportional to the vibrational transition dipole moment to the fourth order, μ^4, comparing to the μ^2 dependence of linear IR spectroscopy.[22] The 4th order dependence in μ makes 2D IR able to distinguish convoluted spectral peaks. The peaks along diagonal of 2D IR spectrum clearly displays at least three pairs of closely spaced peaks, labeled as peak 1 ($\approx$1960 cm^{-1}), peak 2 (($\approx$1938 cm^{-1}), and peak 3 ($\approx$1915 cm^{-1}). For each

pair, the positive peak that resides along diagonal line is the fundamental vibrational transition, whereas the negative peak that is redshifted relative to the positive one is the overtone transition. Interestingly, by taking cut along the diagonal line of a 2D spectrum we show high frequency peak at 2005cm^{-1} is rather "hidden" than "missing" in the 2D contour due to its weak intensity - the diagonal cut of 2D spectrum is consistent with FTIR data (Figure 5.3d). These multiple peaks span across the linewidth of corresponding FTIR spectrum, which supports that multiple absorption peaks are responsible for the extremely broad peak in FTIR.

Temperature dependent FTIR spectroscopy confirms that these peaks are originated from different isomers, such as C_{3v} and D_{2d} geometries, rather than they could be different normal modes of the same isomers. The FTIR spectra of $Co(CNAr^{Mes2})_4$ in d8-toluene at different temperature shows that the intensity of peak 2 increases in relative to peak 1 and 3 as temperature decreases from 308K to 268K (Figure 5.4a). At this temperature variation range, it is unlikely that the transition dipoles vary significantly. Thus, the different temperature dependence between peak 2, and peaks 1 or 3 must be due to that peak 2 belongs to a different conformer from peak 1 and 3, and the two conformations have different free energy. To further identify the two conformations and examine our interpretation of temperature dependent FTIR results, we conducted DFT calculation on both C_{3v} and D_{2d} geometries and simulate corresponding IR spectra. After applying proper scale factor, the calculated peak positions agree with experimental measurements well. Peaks 1 and peak 3 correspond to the E and B2 modes of D_{2d} geometry respectively, whereas peak 2 is from the double-degenerated E modes of C_{3v} (Figure 5.5b). The calculations also predict that for C_{3v} geometry at higher frequency there should be another peak with lower intensity, which matches well with the high frequency small peak shown in FTIR and diagonal cut spectrum of 2D IR (Figure 5.3d).

With two conformations identified, we further examined the dynamics between these conformations by measuring 2D IR spectral cross peak at a series t_2 time delay. The cross peaks in 2D IR spectra are features that have different frequency positions onto ω_1 and ω_3 axes. The t_2
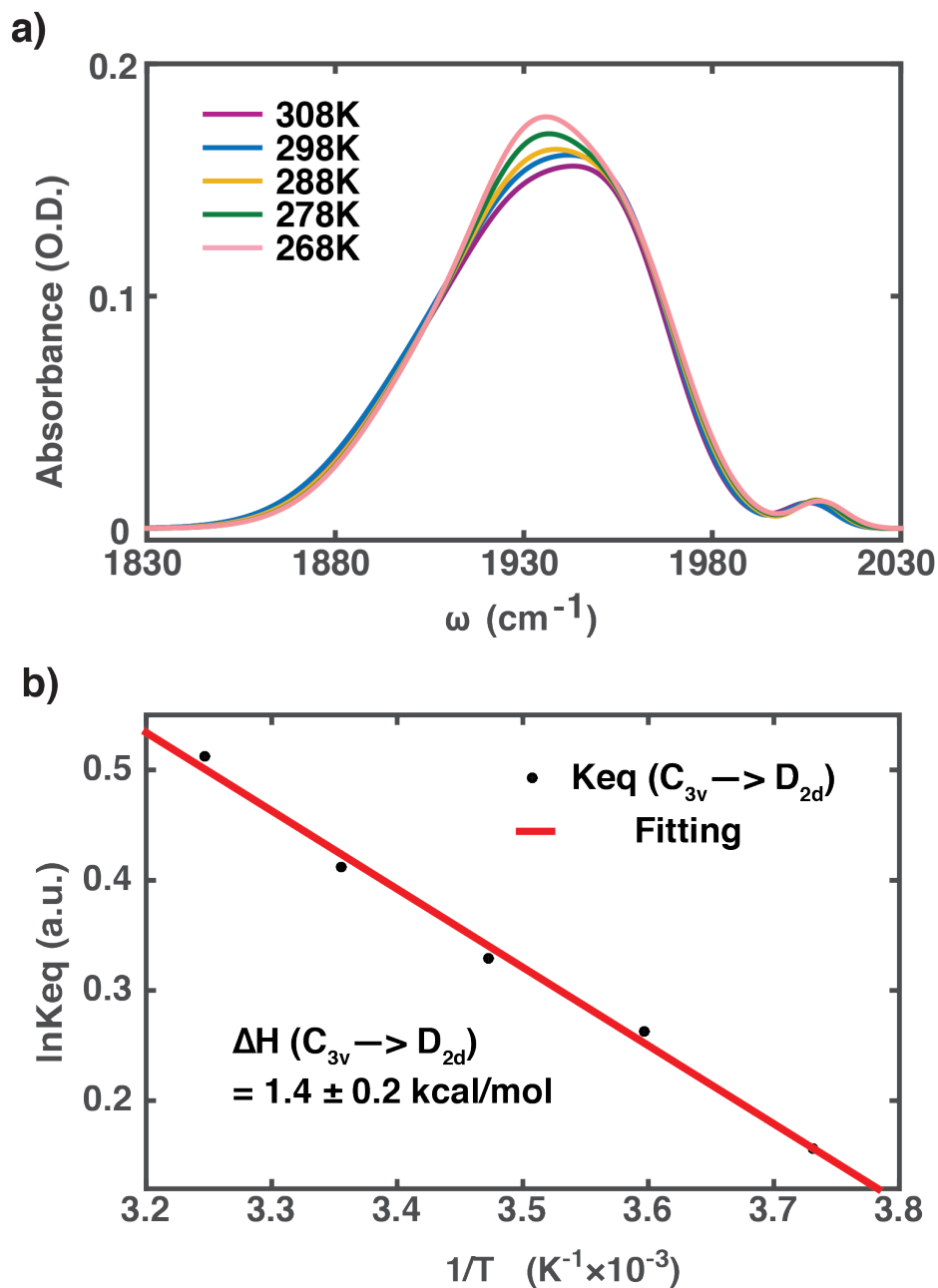
Figure 5.4: a) VT-FTIR spec of Co(CNAr^{Mes2})$_4$ and b) van't hoff plot of lnKeq vs 1/T between C$_{3v}$ and D$_{2d}$.

dependence of cross peak intensity encodes exchange dynamics. For conformation exchanges, as it occurs, vibrational motions are carried from one isomer to another, meanwhile the peak frequency also transits from one frequency to the other. When these frequency transformations
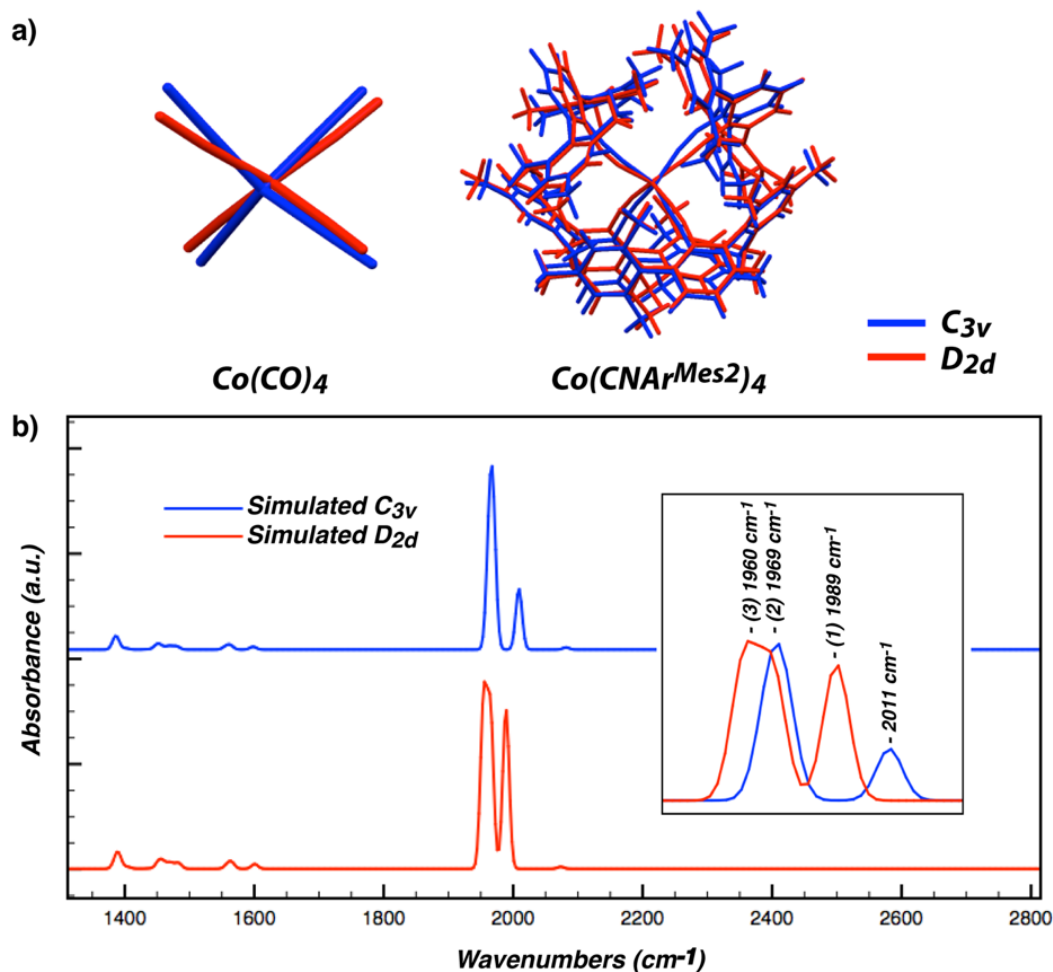
Figure 5.5: a) Molecular overlap of DFT calculated both C_{3v} (blue) and D_{2d} (red) geometries of CoL_4(L=CO, $CNAr^{Mes2}$). b) Simulated IR spectrum of both C_{3v} (blue) and D_{2d} (red) $Co(CNAr^{Mes2})_4$ using b3lyp/6-31g(d):lanl2dz. Wavenumbers are scaled with scaling factor of b3lyp/6-31g(d)=0.9614.

are plotted as a two-dimensional correlation map, these exchange events manifest as cross peaks. For $Co(CNAr^{Mes2})_4$, we observe cross peak growth which manifest as appearance of shoulder peaks when t_2 increases. For instance, at t_2 = 900 fs, the weight of 2D IR spectrum shifts from diagonal to corners (Figure 5.1b), where cross peaks locate at. By taking spectral cuts along ω_3 axis, cross peaks can be better identified from each other and diagonal peaks (Figure 5.1c and d). Constrained by vibrational lifetime of isocyanide mode, we measured early stage cross peak dynamics (0 to 1500 fs, in a step of 150 fs). The normalized cross peak dynamics (Figure

5.6a) show that cross peaks between 1 and 2, 2 and 3 increase their intensity, whereas cross peak between 1 and 3 remain constant. This result agrees with the diagonal peak assignments: cross peak between 1 and 2, and 2 and 3 represents the dynamic conformational exchange between the C_{3v} and D_{2d} isomers.
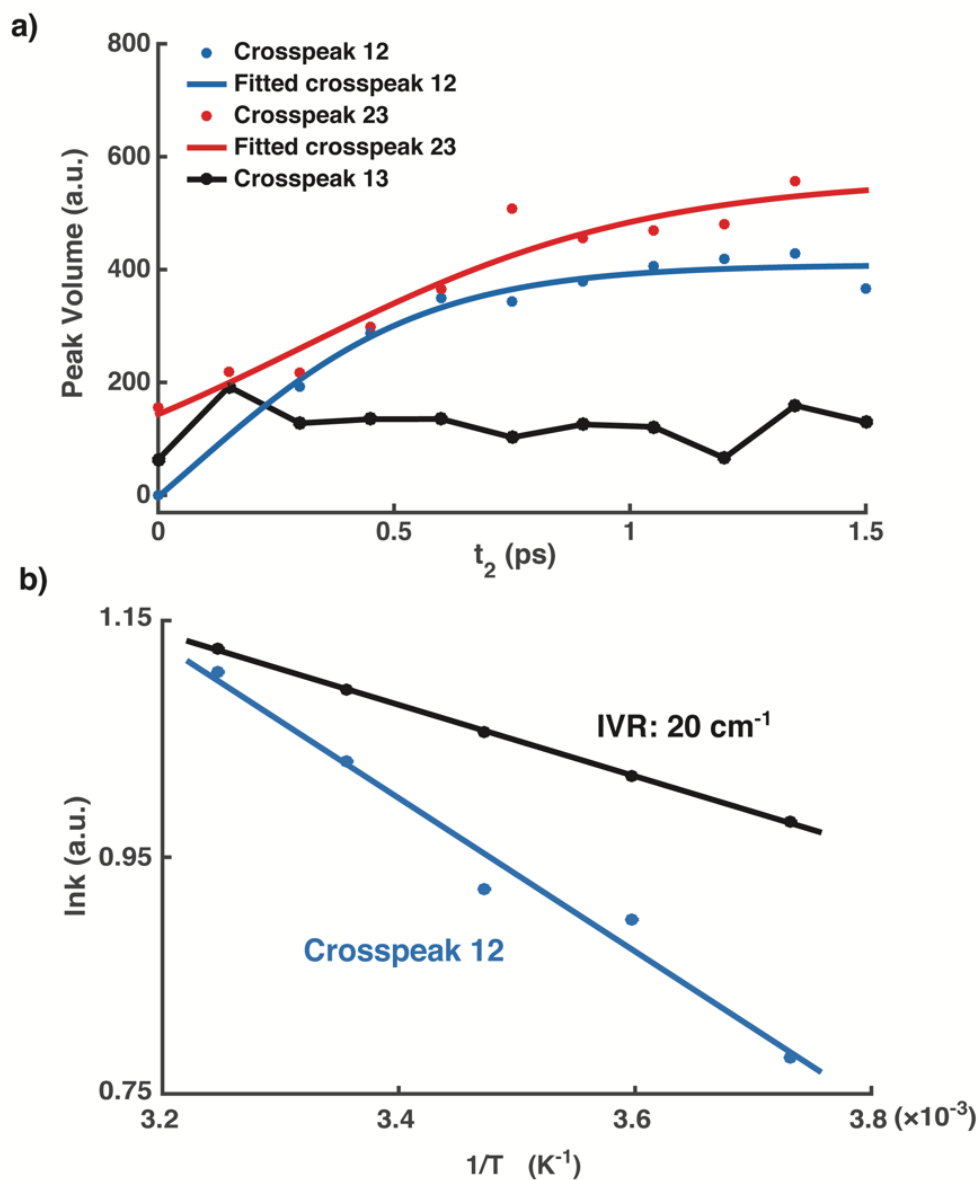
Figure 5.6: a) Dynamics traces of different cross peaks as functions of t_2. b) Plot of ln(k) vs. 1/T. Rate of cross peak growth and rate of IVR (when mode energy difference is $20 cm^{-1}$) have different temperature dependent.

Despite the consistency between peak assignments and cross peak dynamics points to what we observed is conformation exchanges, we still examined the other possibility of cross peak dynamics – intramolecular vibrational redistribution (IVR), by measuring 2D IR cross peak dynamics at different temperature. IVR and conformational exchanges have different temperature dependence.[25, 143–145] We found the rate of cross peak growth slows down steadily as temperature decreases (Figure 5.6b, details in Section 5.2.3). This trend agrees better with the strong temperature dependence of conformation exchange, whereas IVR between two vibrational modes with $\approx 20 \text{ cm}^{-1}$ energy difference has weaker temperature dependence - for IVR to happen it requires energy from solvent bath as in phonon modes to match with the energy difference between two vibrational modes.[136] From the temperature dependence of cross peaks dynamics, we determined the exchange activation energy barrier of conformation exchanges to be $\Delta Ea(D_{2d}\text{-}C_{3v}) = 0.5 \pm 0.1$ kcal/mol, while $\Delta Ea(C_{3v}\text{-}D_{2d}) = 1.9 \pm 0.4$ kcal/mol.

We therefore conclude that the observed cross peak dynamics is originated from conformation exchange. However, the time scale of the dynamics is unexpectedly fast considering the bulky ligands (about 0.5 to 1 ps depending on temperature). For example, previous research on $Fe(CO)_5$ measured 2.5 kcal/mol activation energy barrier and less than 10 ps cross peak dynamics.[136] $Co(CNAr^{Mes2})_4$, on the other hand, are coordinated with bulky m-terphenyl ligands, which intuitively should slow down conformational exchanges comparing to Berry pseudorotation of $Fe(CO)_5$. Therefore, an important scientific question to address is how ultrafast conformation exchanges could occur in $Co(CNAr^{Mes2})_4$?

This surprising result could be understood by considering the nature of molecular vibrational transitions in 2D IR spectroscopy. Because the CN group directly attach to Co, its vibrational frequency probes the electronic structures of the Co metal core, whereas the fluctuation and structural rearrangement of the outer sphere m-terphenyl ligands–Ar^{Mes2} should only have minor effect to the CN vibrational modes. Detailed DFT calculations agree that as long as the $Co(CNAr^{Mes2})_4$ core symmetry remains the same, twisting outer sphere geometry does not affect
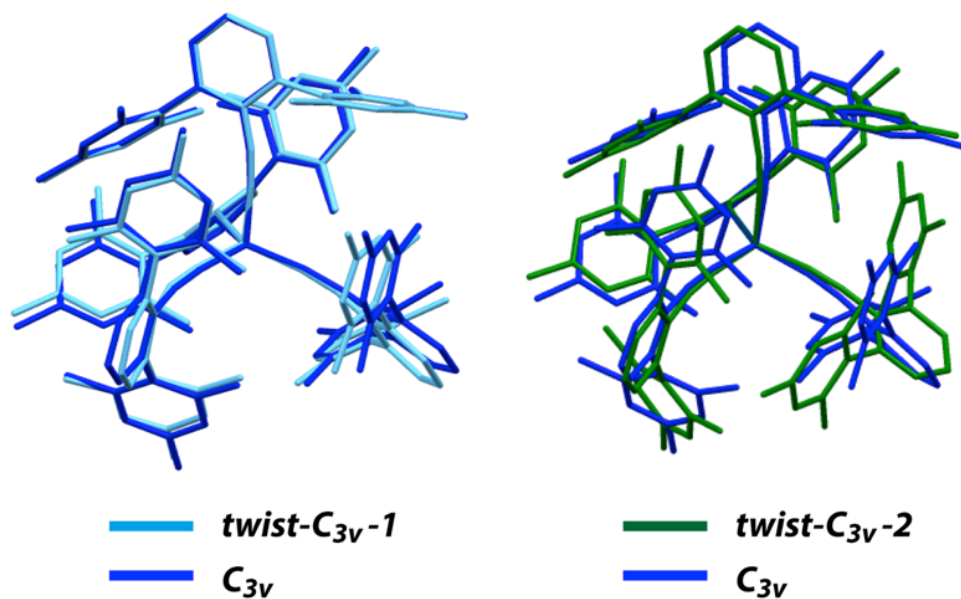
Figure 5.7: Optimized C_{3v} Co(CNAr^{Mes2})$_4$ geometry and C_{3v} Co(CNAr^{Mes2})$_4$ geometries with twisted ligands (core angles fixed at optimization).
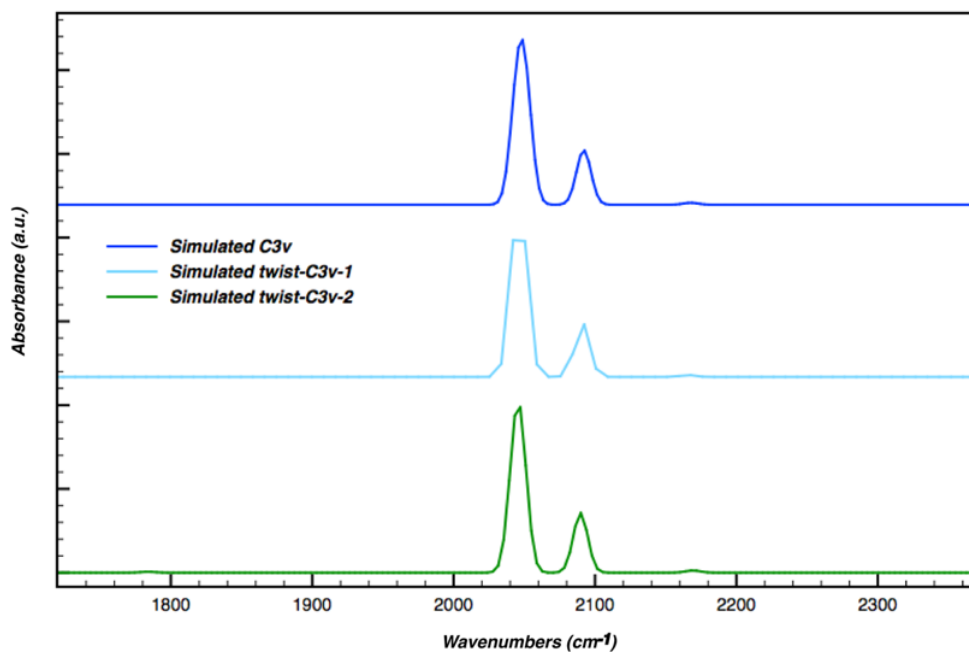
Figure 5.8: Simulated IR spectrums of optimized C_{3v} Co(CNAr^{Mes2})$_4$ geometry and C_{3v} Co(CNAr^{Mes2})$_4$ geometries with twisted ligands (core angles fixed at optimization).

the IR spectrum of CN stretches (Figure 5.7 -5.10.). This preferential sensitivity of CN group makes 2D IR measures the isomerization of electronic structure near the Co core (C-Co-C), rather than the isomerization of the entire molecule. In other words, the slow motion of the bulky ArMes2 ligands at outer sphere does not matter: even if they are still in the original positions, as long as the core changed symmetry and its corresponding electronic structures changes, this Co core isomerization is measured by 2D IR.
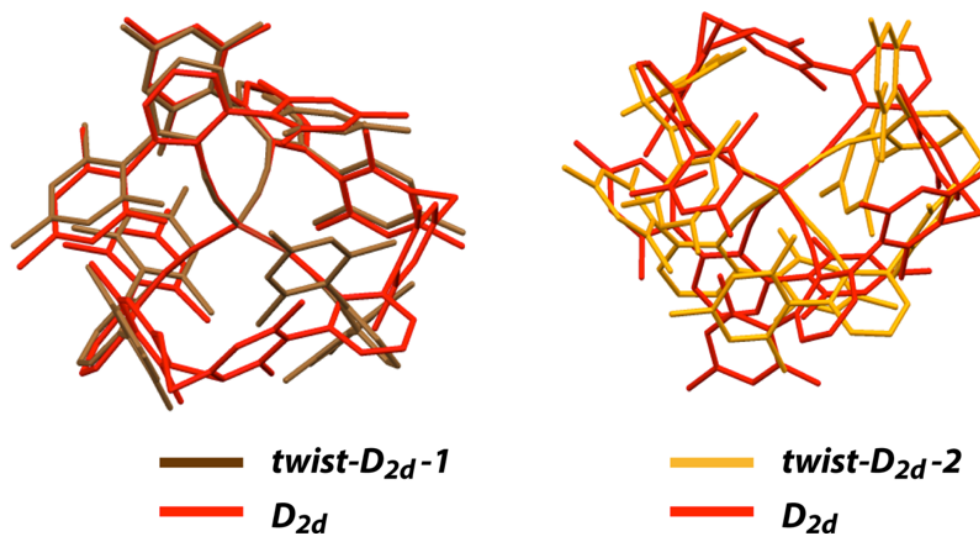
Figure 5.9: Optimized D_{2d} Co(CNAr^{Mes2})$_4$ geometry and D_{2d} Co(CNAr^{Mes2})$_4$ geometries with twisted ligands (core angles fixed at optimization).

From detailed DFT studies, it appears only a few degrees of core-ligands movements are enough to change of electronic structure associated with C_{3v} to D_{2d} exchange, which is the essential of the core isomerization. The calculated C_{3v} and D_{2d} isomers of CoL$_4$ (L= CO, CNAr^{Mes2}) are very similar in geometry even though they are different electronic structures (Figure 5.5a). Unlike the case of Fe(CO)$_5$, whose CO swings 90 degree in isomerization, isomerization of CoL$_4$ only involves small angle changes. Therefore, the mechanical movements of ligands (and imaginary frequency of the transition states) should not be the limiting factor for isomerization, and instead, the electronic structure of Co core at different geometry and activation energy of Co isomerization should be the key factor, and the latter has been determined to be
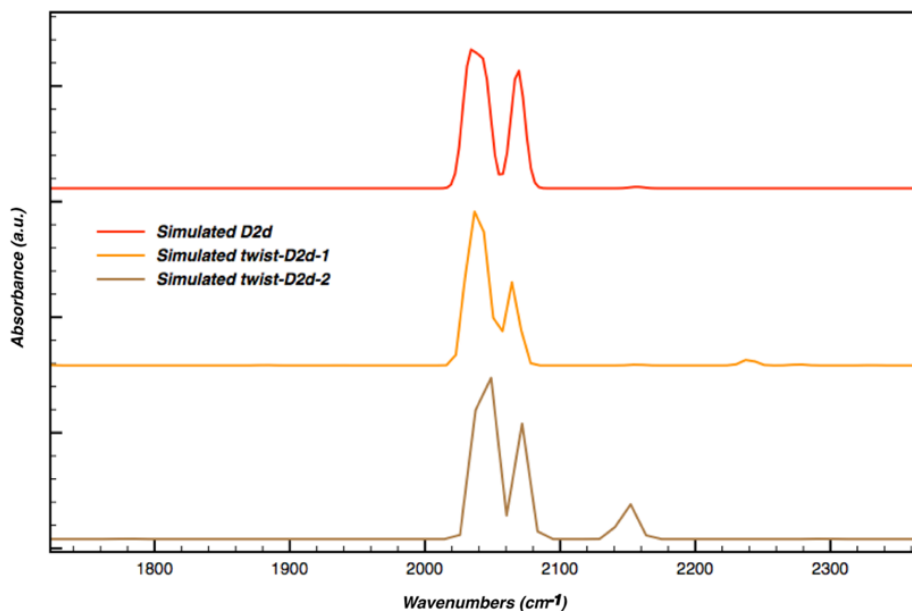
Figure 5.10: Simulated IR spectrums of optimized D_{2d} Co(CNAr^{Mes2})$_4$ geometry and D_{2d} Co(CNAr^{Mes2})$_4$ geometries with twisted ligands (core angles fixed at optimization).

small $\Delta Ea(D_{2d}-C_{3v}) = 0.5 \pm 0.1$ kcal/mol, while $\Delta Ea(C_{3v}-D_{2d}) = 1.9 \pm 0.4$ kcal/mol.

A complete the energy schematic of conformation exchanges is further estimated from both experimental and theoretical results. From the VT-FTIR, we estimate ΔH to be 1.4 ± 0.2 kcal/mol (Figure 5.4b). The experimental results suggest that these two isomers may be equi-energetic as has been traditionally proposed for Co(CO)$_4$. DFT calculation on all CoL$_4$ (L=CO, CNMe, CNXyl, CNAr^{Ar2}, CNAr^{Mes2}) isomers results ΔH in the range of 1-4.5 kcal/mol with C$_{3v}$ lower in energy at all cases. (Table 5.2) The presence of increased steric encumbrance resulted in larger ΔH. It is interesting to note that the experimental determined value of Co(CNAr^{Mes2})$_4$ is closer to the DFG computational ΔH of CoL$_4$. One possibility is steric hindrance of the bulky ligands creates local minimums, which lies higher in energy than the fully relaxed geometry and also experience smaller activation energy for isomerization - agree with the experimental measured ΔEa. This picture of equi-energetic states rationalizes the solid-state structure of Co(CNAr^{Mes2})$_4$, which is likely to be an intermediate geometry between C$_{3v}$ and D$_{2d}$ and can be affected by low-energies on the order of crystal packing forces.

Table 5.2: Calculated Energy Differences Between CoL$_4$ (L= CO, CNMe, CNXyl, CNAr^{Ar2}, CNAr^{Mes2}) C$_{3v}$ and D$_{2d}$ Isomers Using 6-31g(d):lanl2dz basis sets. All C$_{3v}$ in lower energy

Ligand (L)	ΔH (kcal/mol) b3lyp	ΔH (kcal/mol) b3lyp/PCM(C6H6)	ΔH (kcal/mol) bp86
CO	3.53		1.29
CNMe	3.73		1.34
CNXyl	3.45		0.34
CNAr^{Ar2}	6.91	7.07	2.80
CNAr^{Mes2}	8.88	8.97	4.48

Finally, does the observed ultrafast conformation exchange of Co(CNAr^{Mes2})$_4$ also represents the isomerization of Co(CO)$_4$ We argue because experimentally we showed that the bulky outer sphere ligands matter little and it is the core electronic structure dictating the isomerization dynamics of metal core, the Co(CNAr^{Mes2})$_4$ isomerization dynamics measured here should closely mimic the dynamics of catalytic intermediate Co(CO)$_4$, due to their similarity in electronic structures. This is a significant implication, because many bulky ligands stabilized isoelectronic molecules similar to Co(CNAr^{Mes2})$_4$ can be used to not only learn electronic structure of unstable unsaturated catalytic intermediates, but also their structural dynamics.

5.4   Conclusions

Despite 2D IR has been used successfully for studying ultrafast conformation exchanges of organometallic compounds, this is the first time a kinetically stabled unsaturated compound being investigated. Surprisingly, ultrafast conformation exchange dynamics is observed, irrespective

to the presence of bulky ligands at outer spheres. Combining this result with detailed DFT calculations, we show that 2D IR probes the electronic structure change accompanied with the isomerization at Co core, whereas the bulky ligands position matter little. This result confirms the long-time speculated dual-conformations and exchange dynamics exists for $Co(CNAr^{Mes2})_4$ and likely, in $Co(CO)_4$.

Chapter 5, in full, is currently being prepared for submission for publication of the material. Jiaxi Wang; Chinglin Chan; Yingmin Li; Bo Xiang; Joshua Figueroa; Wei Xiong. The dissertation author was the primary investigator and author of this paper.

Chapter 6

Short Range Catalyst-Surface Interactions Revealed by Heterodyne Two Dimensional Sum Frequency Generation Spectroscopy

6.1 Introduction

Materials based on a molecular monolayer adsorbed onto a solid surface have drawn significant attention in the field of catalysts,[209] electronics,[210] and biotechnology,[211] because of the possibility to precisely control the function of the molecular monolayers. To improve these materials, it is necessary to understand not only the molecular structures, but also the interactions between the molecules and the surfaces.

In the areas of solar fuels and artificial photosynthesis, the development of catalysts to produce fuels by carbon dioxide reduction reaction (CO_2RR) poses a considerable challenge.[209, 212] One important strategy to prepare new catalysts is the attachment of molecular catalysts to surfaces. Surface attached catalysts offer the promise of high selectivity and tunability of homogenous molecular catalysts, and the robustness and the ease of separation of heterogeneous

61

catalysts. However, the subtle interactions between the catalysts and the surface can significantly change the structure and dynamics of the catalyst and will likely impact the performance of the catalyst.[213] Therefore, it is necessary to understand how catalysts attach to the surface and how they interact with the surfaces. Currently, such information is determined using X-ray or photoelectron spectroscopies,[214–216] which rely on spectral peak position shifts to infer surface interactions, and are typically limited to systems under vacuum. One dimensional sum frequency generation spectroscopy is another powerful approach to investigate surface under working condition,[87–89] but the intrinsic spectral broadening makes extracting surface interactions difficult from either peak positions or lineshapes.[97]

To better reveal the molecular orientation and the interaction with surfaces, we implement surface-sensitive heterodyne 2D sum frequency generation (HD 2D SFG) spectroscopy[91, 96, 98, 101] to study a model surface catalyst for CO_2 reduction, which are composed by a monolayer of Re(diCN-bpy)(CO)$_3$Cl (referred as **1**, diCN-bpy = 4,4'-dicyano-2,2'-bipyridine) on a gold surface. A complete description of the synthesis, characterization and X-ray structures of **1** will be described in a separate report. Similar Re-bpy complexes have been extensively studied in homogenous solution phase using 2D IR spectroscopy,[217–219] where charge and solvent dynamics of ground and electronic excited states are investigated. The corresponding monolayers have only been investigated by Lian using time-resolved SFG spectroscopy[220] for vibrational relaxations and by Fayer using 2D IR spectroscopy[140] for spectral diffusion. To the best of our knowledge, there have been no surface spectroscopic studies that focus on the adsorbate-substrate interactions using HD 2D SFG.

HD 2D SFG spectroscopy[91, 96, 98, 101] can be view as a surface sensitive version 2D IR. It is able to resolve homogeneous and inhomogeneous dynamics, and molecular orientation on molecular submonolayers including air/water interfaces,[91, 101] electrode surfaces,[98] and surface bound biomolecules,[96] which makes it an ideal technique to probe molecules on surfaces. The surface sensitivity of HD 2D SFG is because it is a 4th order non-linear optical

signal. Similar to 2nd order signals such as second harmonic generation or sum frequency generation, 4th order signals can be only generated from non-centrosymmetric media, such as interfaces. The ability to distinguish dynamics in both fast and slow time scales is because HD 2D SFG measures the same 3rd order vibrational response function, as 2D IR does, which tracks the vibration mode evolution as a function of time, from femtoseconds to hundreds of picoseconds. In particular, comparing to 1D SFG, which determines dynamics from linewidth and peak positions alone, HD 2D SFG provides many additional lineshape parameters — center line slope,[112] nodal line slope,[113] diagonal and antidiagonal linewidth, etc. — making it more sensitive to subtle dynamic changes. Furthermore, heterodyne detection can reveal the phase of the 2D SFG spectra, which is related to the orientation of surface adsorbate molecules, and also improve its sensitivity to low coverage surfaces,[121] thanks to its linear dependence on surface coverage.[90, 97, 121]

6.2   Methods

6.2.1   Sample Preparation

The synthesis, characterization, and X-ray structure of Re(4,4'-dicyano-2,2'-bipyridine)-$(CO)_3Cl$ was reported in a separate publication.[221] Optically flat Au substrates consist of a layer of Cr (1-4nm) and Au (200-300nm) evaporated onto borosilicate glass slides. For surface attachment of the catalysts, the gold coated slide was cleaned using a Bunsen Burner method[222] before being immediately submerged in a 1 mM solution of the complex in chloroform for three days in the dark. The sample was then washed with pentane and dried under a stream of nitrogen before use.

6.2.2   HD 2D SFG Spectrometer

Detailed 2D SFG experimental set up is described in Section 3.3. In particular, SFG of bare gold was also collected as the reference for phase calibrations. The HD 2D SFG signal is measured at ppppp polarization, where the polarizations of all pulses are set to be p (in plane with the surface normal-incidence beam plane) to the sample, by pairs of waveplates and polarizers, and only p polarized signal is detected. We note in both our experiment and many other SFG experiments gold surfaces are used as the substrate, which generate the non-resonance SFG signal. In both experiments, the gold SFG signal can interfere with the SFG signal of interests. Therefore, in principle, both experiments are self-heterodyned. The difference between our heterodyne detection scheme and the other SFG experiments, is that the measured self-heterodyne spectrum is further phase corrected by the reference SFG spectrum from bare gold, following the methods by Tahara. In this way, we can extract both the real and imaginary part of the SFG spectra, whereas other experiments does not phase correct the spectrum and take advantage of this self-heterodyne scenario.The samples are constantly rastered between each scan ($\approx$10 mins) to avoid sample damaging. To improve signal to noise ratio, multiple scans are averaged for each time step.

6.2.3   2D IR Spectrometer

Detailed 2D IR experimental set up is described in Section 3.1. In brief, the 2D IR spectra are collected using the same pulse sequences of the HD 2D SFG spectrometer, in pump-probe beam geometry using a Ge-AOM based mid-IR pulse shaper. Both beams are focused by a 10cm parabolic mirror and collimated by another parabolic mirror. In order to be able to detect the 2D IR signal by the CCD camera and perform direct comparison to the HD 2D SFG spectra, the collimated 2D IR signal and the probe beam are upconverted by the same 800nm pulse in HD 2D SFG on a 5%Mg: LiNbO3 crystal.[118, 119] The upconverted signal is self-heterodyned and measured the same way as HD 2D SFG signal and the first vibrational coherences are also

measured the same way using the pulse shaper. The absorptive 2D IR spectra are then obtained by Fourier transform along t_1 axis.

6.2.4 Retrieving Pure Absorptive Spectra

To obtain absorptive HD 2D SFG spectra with calibrated phase, the non-resonance SFG signal from bare gold surface are collected for extraction of phase information.[90, 97, 121] Detailed data analysis methods are discussed in Section 3.3. Absorptive 2D IR spectra can be obtained by directly Fourier transforming along t_1 axis, without the phasing procedure described above for 2D SFG. In the pump-probe geometry, the phase matching condition for rephasing and non-rephasing spectra are collinear, which lead to absorptive lineshape after performing Fourier transforms.

6.2.5 Center-line slope determination

We first find the peak position along ω_3 axis at corresponds to each ω_1 cut — $P_{\omega_1}(\omega_1)$, where a range of $\omega_1 \pm 4$ cm^{-1} is chosen to avoid other diagonal peaks. The slope is find by fitting $P_{\omega_1}(\omega_1)$ vs ω_1 as a line. Enlarged HD 2D SFG and 2D IR spectra with the CLS fitting are shown in Figure 6.3.

6.2.6 Cross Peak Simulation

The cross peak lineshape simulation is done based on the theory presented in Ge, Zanni and Hochstrasser's paper.[223] We assume no spectral diffusion between the vibrational modes. Since in our experiment, t_2=0, there should be no spectral diffusion. We simulate the 3rd order response function in time domain at a step of 4 fs, from 0 to 4 ps. The parameters used in the simulation are listed in Table 6.1.

Table 6.1: Parameters used in the cross peak simulation.

	$\omega_1(cm^{-1})$	$\omega_2(cm^{-1})$	$T_{2,1}(fs)$	$T_{2,2}(fs)$	$\sigma(fs-1)$	$\sigma(fs-1)$
Scenario 1	1900	2028	2000	2000	0.002	0.004
Scenario 2	1900	2028	500	2000	0.002	0.002

6.2.7 Vibrational population dynamics

The lifetime of the vibrational modes are measured by mid-IR pump, SFG probe spectroscopy (Figure 6.5). The dynamics are fitted into single exponential. The low-signal to noise is due to that the scan was acquired in short exposure time and average. Nevertheless, the signals can show that the vibrational lifetime between the A'(1) and the A" /A'(2) modes are different, where the lifetime of A"/A'(2) peak is shorter, which lead to broader homogenous broadening and agree with the trend we observed in HD 2D SFG. We note that vibrational lifetime is only one part of the homogeneous linewidth, since the pure dephasing dynamics also contribute to the homogenous linewidth, which is why HD 2D SFG is a more comprehensive way to determine how surface interactions influence spectral lineshapes.

6.2.8 Determine tilt angle of the surface molecule by Polarization dependent IRRAS

To determine the orientation of surface molecules, we need to determine the tilt angle of vibrational vectors in both lab frame and molecular frames. The tilt angles of vibrational vectors with respect to surface normal in lab frame are measured with polarization dependent Infrared Reflection Absorption spectroscopy (IRRAS). Polarization dependent IRRAS were taken at fixed incidence angle of $45°$ (Bruker Tensor 37 FTIR, Pike Technology 45Spec). Four different

polarization angles were used: 0° (s polarization), 20°, 45°, 70°. Following the procedure in [140, 223], we determined the ratio between A_β / A_s, listed in Table 6.2. With known angle of incidence (α), polarization angle (β), the tilt angles (θ) of transition dipole moments from the surface normal can be calculated from the following equation:

$$\frac{A_\beta}{A_s} = \frac{((\frac{\cos^2\beta}{2} + \frac{\cos^2\alpha\sin^2\beta}{2} - \sin^2\alpha\cos^2\beta)\sin^2\theta - \sin^2\alpha\sin^2\beta)}{\frac{1}{2}\sin^2\theta} \quad (6.1)$$

Table 6.2: A_β / A_s of the vibrational modes

A_β / A_s	A'(1)	A"	A'(2)
20°	1.08	0.94	0.93
45°	1.30	1.14	1.09
70°	1.37	1.20	1.14

A'(1) can either point up or down, but A'(2) and A" need to be point to the opposite directions. The calculated angles have two possibilities, which are listed in Table 6.3.

To know the tilt angle of vibrational modes in molecular frame, we implemented DFT calculation using B3LYP/LanL2DZ in Gaussian. The xyz coordinate of the vibration modes and key atoms are summarized in Table 6.4.

By performing Euler rotation, the vibrational modes in molecular frame can be transformed to lab frame. Accordingly, the molecules are also rotated to the lab frame. The two

Table 6.3: Angle relative to surface normal determined from IRRAS.

	A'(1)	A"	A'(2)
Orientation 1	68 ± 11°	118 ± 4°	121 ± 7°
Orientation 2	112 ± 11°	62 ± 4°	59 ± 7°

Table 6.4: Coordinates of vibrational modes and atoms in molecular frame, determined by DFT calculation.

	X (Å)	Y (Å)	Z (Å)
Vibrational modes			
A'(1)	0	0	0.28
A"	0	-0.18	0
A'(2)	0.29	0	0
Atoms			
Re	0	0	0
Cl	-2.14	0	-1.20
C	-0.71	-1.36	1.22
C(axial)	1.68	0	0.77
N	0.70	-1.33	-1.63
N	0.70	1.33	-1.63
C	-0.71	1.36	1.22

possible orientations are illustrated in Figure 6.6. The angles between the Re-Cl and surface normal are 45° and 135° for the two orientations.

6.3 Results and Discussion

We show that the center-line slopes[112] (CLS, red circles in Figure 6.1) of HD 2D SFG spectra are uniquely sensitive to the short-range interactions between vibrational modes of surface

molecules and surface substrates. HD 2D SFG peaks of **1** have different CLSs, which can be induced by either different homogenous or inhomogeneous broadening experienced by these vibrational modes. It is often difficult to distinguish which of these mechanisms causes the changes of CLS. By analyzing the spectral tilts of cross peaks, we unambiguously determine that the origin is homogenous broadening. This approach provides a new and straightforward protocol to disentangle various sources of lineshape broadening, in comparing to the standard but more complicated lineshape fitting methods based on either Kubo or more advanced models. We further attribute this homogenous broadening difference to the distinct amount of interactions between vibrational transition dipoles and the image dipole on the surface.[224, 225] Our findings then allow the determination of the ensemble-averaged molecular orientations from HD 2D SFG and Infrared Reflection Absorption (IRRAS) spectra.

To learn the impact of surface attachment, we compare the HD 2D SFG spectrum of the CO vibrational modes of **1** on a gold surface and 2D IR spectrum of the same modes from **1** in solution. In the HD 2D SFG spectrum of **1** on gold (Figure 6.1a, Figure 6.2 for sketches of the vibration modes), the diagonal peaks at $\omega_1 = 2020$ cm^{-1} correspond to the fundamental transitions of A'(1) carbonyl stretch. The out-of-phase peak that is redshifted from the diagonal peak is the corresponding overtone transition. The peak sets between 1950 and 1890 cm^{-1}, correspond to the A" and A'(2) modes of the CO ligands,[140, 217] which is also composed of the fundamental and overtone doublet. In the 2D IR spectrum of the same complex in DMSO (Figure 6.1b), the two sets of peaks at 2020 cm^{-1} and 1919 cm^{-1} originate from the fundamental transition of A'(1) and A" modes. The A'(2) mode and the overtone of A" mode are out of the spectral window in the 2D IR spectrum, because both of them manifest large redshifts (see FTIR, right panel of Figure 6.1b) in solution phase comparing to on the surfaces.

A careful inspection of the HD 2D SFG spectrum in Figure 6.1a, reveals that the A'(1) peak and lower frequency peak sets of A" and A'(2) have different lineshapes. Although all diagonal peaks are elongated in HD 2D SFG spectrum, which indicates molecules are inhomogeneously
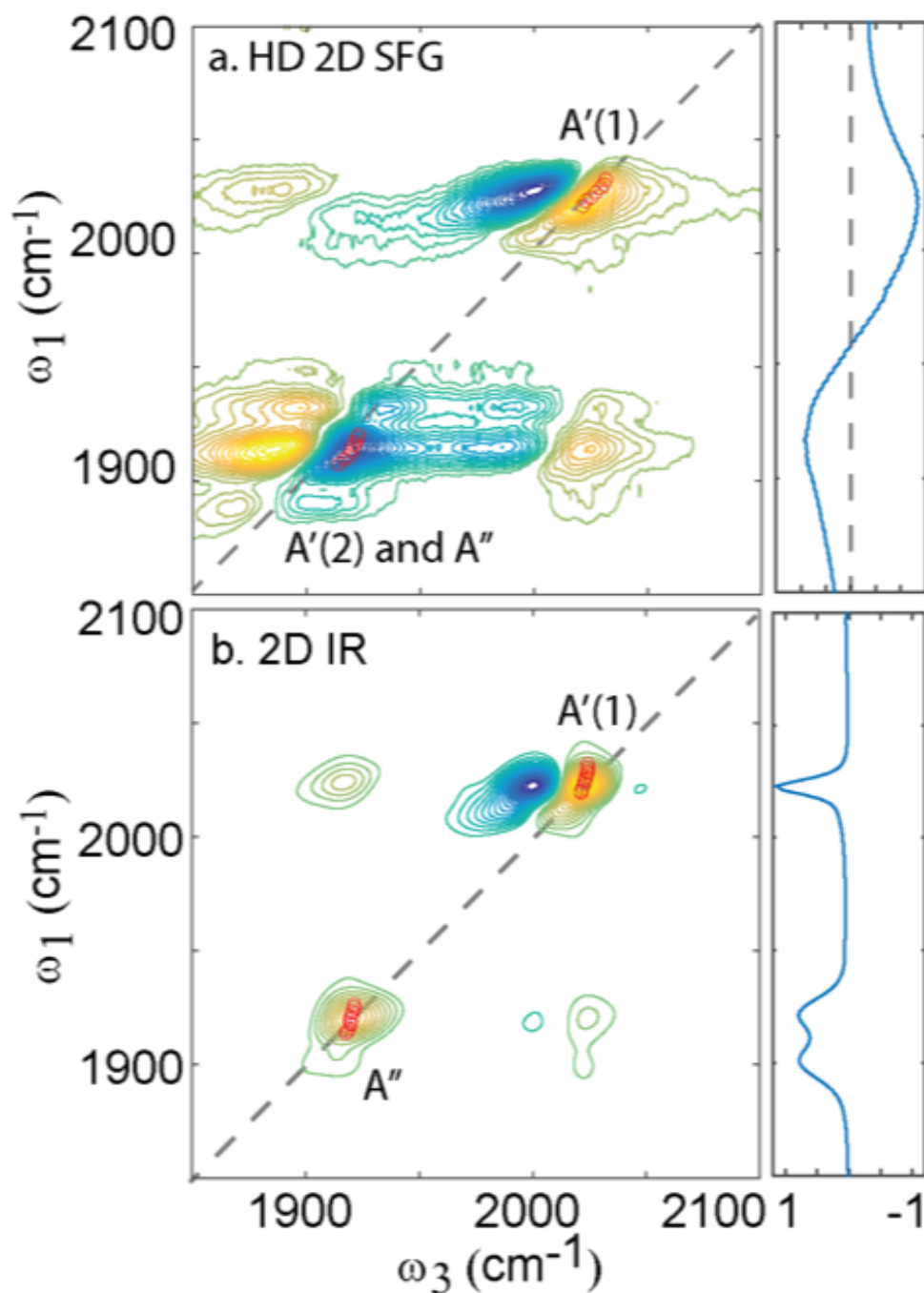
Figure 6.1: Multidimensional vibrational spectra of **1**. (a) HD 2D SFG spectrum. Right panel of a: HD SFG spectrum of the same sample. (b) 2D IR spectrum of **1** in DMSO. Right panel of b: FTIR.

distributed on the surface, the lower frequency peaks are less tilted along the diagonal than the

A'(1) peak. This is in sharp contrast to the 2D IR spectra, where both peaks are round and
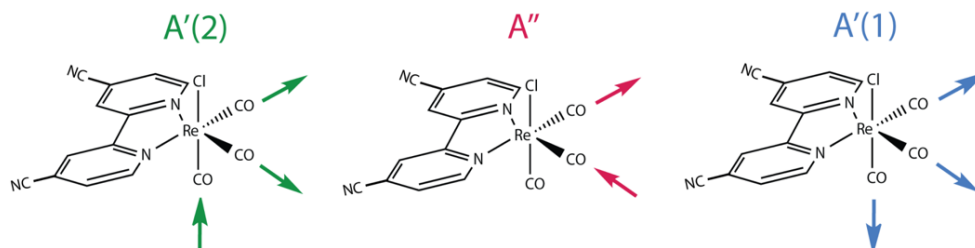
Figure 6.2: The carbonyl vibrational modes in the Re-complex studied here. A" is the asymmetric vibrational modes, A'(1) is the symmetric mode and A'(2) is the out of phase symmetric mode

lie along the vertical line, which indicates the molecular vibrational dynamics are dominated by homogenous broadening dynamics, such as solvent interactions. To make a quantitative comparison, we extract the CLS of both the A'(1) peak and the lower frequency peak set in 2D IR and HD 2D SFG spectra (Figure 6.1, see Section 6.2.5 for methods and Figure 6.3 for enlarged figures). While there are several methods to quantify the spectral tilt, we choose CLS because the method is not sensitive to one dimensional apodization,[112] and in our experiment the ω_3 axis was apodized during the SFG upcoversion process. We fit the slope around the center position of the diagonal peak, ± 7 cm^{-1}, to avoid the influence caused by multiple peaks from different conformations on the surface or in solution. Clearly, in the 2D IR spectrum of the solution-phase sample, the CLSs of both peaks are similar (A'(1): 0.23 ± 0.07, A'(2) and A" : 0.25 ± 0.04), which indicate a homogenous environment. This result agrees previous published results.[140] It indicates both vibrational modes of **1** experience the same microenvironments and solvent dynamics, which leads to the same amount of homogenous broadening. However, in the HD 2D SFG spectrum of the surface sample, the lower frequency peak set has a smaller CLS (A'(2) and A": 0.72 ± 0.16) than the A'(1) peak (1.03 ± 0.06). This difference is notable and indicates these two sets of normal modes experience different dynamics or environments on the surface.

CLS indicates the balance between the inhomogenous and homogenous broadenings - how much inhomogeneous broadening contributes to the lineshape. As the samples approach fully inhomogeneous, the spectra are tilted along diagonal line and CLS equals to one. On the other
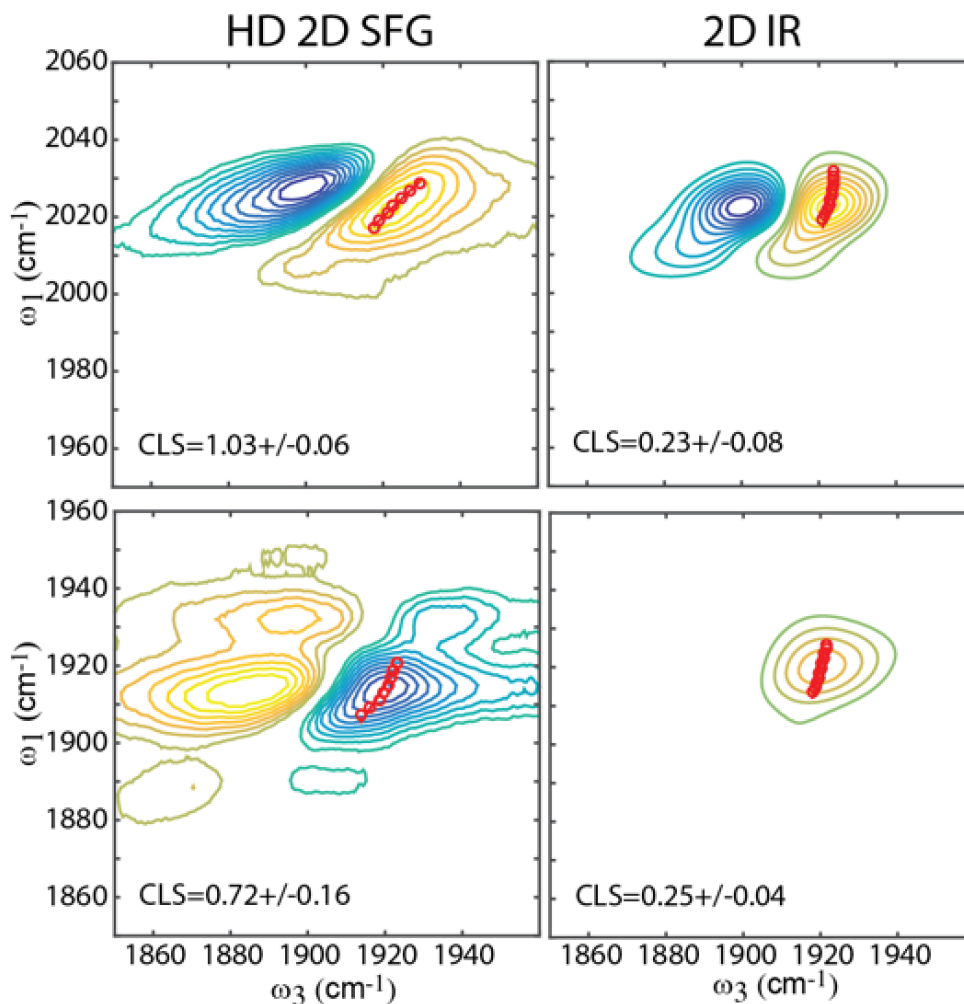
Figure 6.3: CLS fit to the diagonal peaks of HD 2D SFG and 2D IR spectra

hand, when homogenous broadening dominates the lineshape, the spectra are tilted vertically, and CLS equals to zero. Therefore, the differences in CLS can be caused by two scenarios: All the modes experience the same amount of homogenous broadening, but the A'(1) mode is more inhomogeneous than the A" and A'(2) modes (Scenario 1), or that all experience the same inhomogeneous broadening, but the A" and A'(2) modes are more homogenously broadened than the A'(1) mode (Scenario 2).

Although it is difficult to distinguish between these two scenarios from the diagonal peak features alone, we show here it is straightforward to determine which scenario leads to the CLS

difference when we inspect the cross peaks. The cross peaks are due to strong intramolecular coupling. They appear as pairs of out of phase doublets at the corners of both 2D spectra, which are determined by the frequency of two coupled vibrational peaks. To inspect the cross peaks of the HD 2D SFG more clearly, they are plotted in Figure 6.4a and d, where the red line indicates their CLSs. The upper left cross peak (Figure 6.4) is tilted along the diagonal (dashed gray line) but also broadened along ω_3, whereas in Figure 6.4d the lower right cross peaks is less tilted along diagonal but more along the ω_1 axis. This striking contrast in CLS is the key to differentiate the two scenarios.
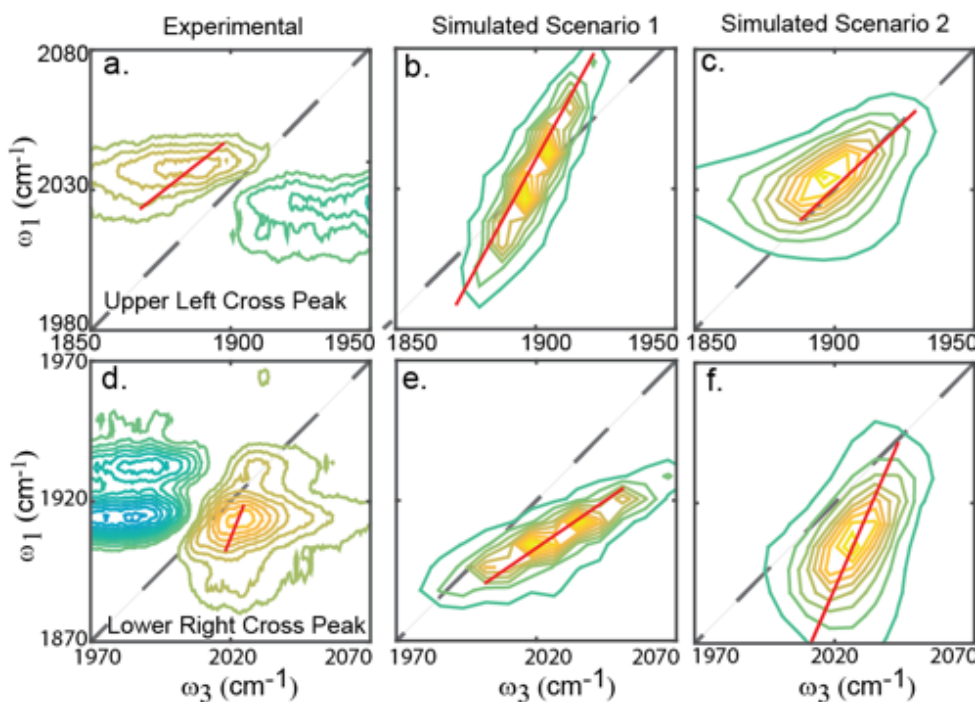
Figure 6.4: Cross peaks of HD 2D SFG of **1**. (a and d) Cross peaks measured in experiment. (same as Figure 6.1, zoomed in for clarity). (b and e) Simulated cross peaks for Scenario 1. (c and f) Simulated cross peaks for Scenario 2. Red lines indicate the center line slopes

To show how the cross peak CLS is sensitive to the different contributions of lineshape broadening, we simulated the cross peaks[223] corresponding to the two scenarios mentioned above (Section 6.2.6 for details). Under the harmonic oscillator approximation, both fundamental

and overtone peaks should have the same lineshape.[22] Therefore, in the simulation we only simulated the lineshape of the fundamental peaks. We note our intention is not to quantitatively fit the experimental spectra and retrieve lineshape broadening parameters but to show how a simple inspection of the CLSs of cross peaks can reveal whether the vibrational modes experience homogenous or inhomogeneous broadening.

In Scenario 1, where the A'(1) mode is more inhomogeneous, we found that upper-left peak (Figure 6.4) is stretched along ω_1, and tilted more towards the ω_1 axis, whereas the lower-right peak (Figure 6.4e) is tilted towards the ω_3 axis. This is opposite from the cross peaks lineshape in measured spectrum. In Scenario 2 (Figure 6.4c and f), where A'(2) and A" modes are more homogenously broadened than the A'(1) mode, the upper left cross peak is broadened along ω_1 axis and tilted along diagonal, whereas the lower right peak is tilted towards ω_1 axis. This trend from Scenario 2 matches well to the CLSs of measured spectra in Figure 6.4a and d. Therefore, we conclude that the A" and A'(2) modes experience extra interactions that causes more homogenous broadening but all three modes are similarly inhomogeneously broadened. This also suggests that homogenous broadening is more sensitive to the local environment than inhomogeneous broadening, which agrees with previous results. In the 2D IR spectra of a similar Re complex measured by Fayer and co-workers, they observed that spectral inhomogeneity is not sensitive to the chain length of linker groups between the Re complex and the solid surface.[226] Our results demonstrate that the CLSs of HD 2D spectra is an unambiguous way to reveal subtle interactions or dynamics changes, when other parameters such as spectral peak positions or linewidths might not be sensitive to the changes because of spectral convolutions.

Because the gold surface is the only material that is brought close to compound **1**, the difference in homogenous broadening should be caused by short-range interactions between the molecules vibrational modes and the gold surface, where the interactions strongly depend on the relative direction and distance of the transition dipole moments to the surface. We rule out the possibility of intermolecular interactions, since it has been shown in previous studies

that the coupling between molecules in a similar Re-complex monolayer is negligible.[226] Among these short range interactions, contributions to homogenous broadening that require the molecules to be chemisorbed on gold surface can be ruled out as well because the CO modes do not directly attach to the gold surface through either chemi- or physi-adsorptions. These interactions include the non-adiabatic charge transfer interaction[227] and the coupling to low frequency modes,[228, 229] such as hindered rotation and translation.

Therefore, the most likely origin of the adsorbate-surface interaction in play is coupling between vibrational modes and image dipoles.[224, 230–238] From early surface IR spectroscopy research[224] it is known that the image dipole interaction is the dominant vibrational decay mechanism on adsorbate-metal interfaces when the vibrational modes do not directly attach to and is ¡10 nm away from the surface. This interaction depends on both relative orientation and distance of the vibrational modes to the surface. As we reveal below, the ensemble-averaged angle of the three modes to surface normal are very similar (only directions are different), and therefore, we argue that the orientation influence on the image dipole interaction is similar to all three modes. The lifetime of vibrational modes depends on the relative distance between the vibrational modes and the surface to the 4th power,[224] which means that small changes in distance can cause large difference in vibrational lifetimes. Typically, shorter vibrational lifetime further broaden the homogenous linewidth. For the molecules we investigate here, since A'(2) and A" modes are more homogenously broadened (vibrational life time of A' (1) is 26 ps and of A'(2) / A" is 20 ps, see Figure 6.5 and Section 6.2.7 for details), this suggests that the A'(2) and A" modes are closer to the surface.

Combined with sign of HD 2D SFG peaks, our knowledge that the A'(2) and A" modes are closer to the surface can help to precisely determine the ensemble-averaged molecular orientation. In HD 2D SFG, the sign of the diagonal peak is different between the A'(1) and the other two modes. This difference of signs in HD 2D SFG indicates that A'(1) mode's direction is opposite from A"(2) and A' modes.[91, 98] However, this information is usually not enough to determine

75
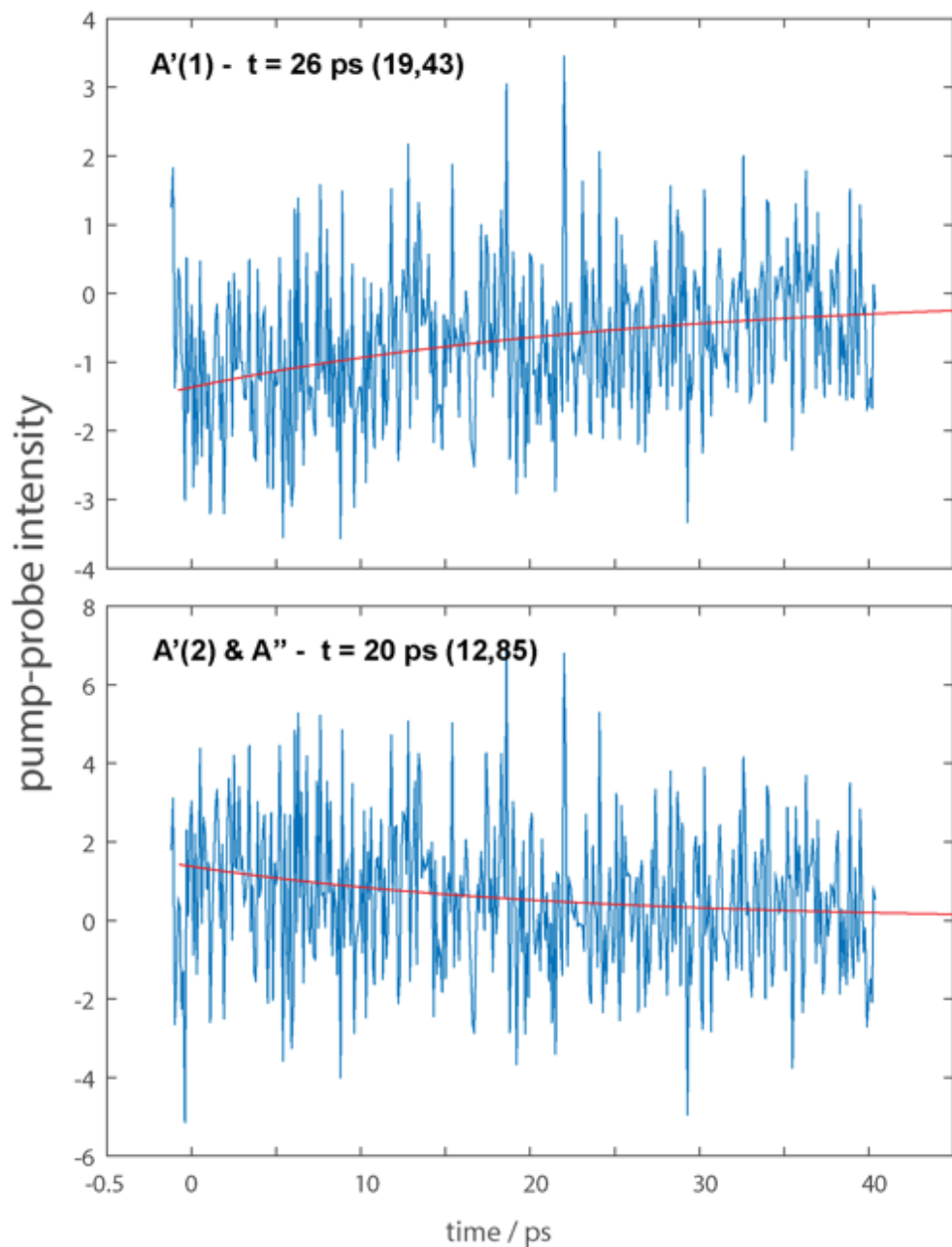
Figure 6.5: Vibrational lifetimes of A'(1) and A'(2)/A'' modes. The A'(2)/A'' peaks have shorter lifetimes — 20 ps (the numbers in the parenthesis are the 95% confidence range

the absolute orientations of the molecule, since the phase of the local oscillator, which is the non-resonance signal from gold surface, can be either $0°$ or $180°$.[87] Therefore, it could either be that A'(1) mode is directed upwards and the other two are downwards, or the opposite. Since we know that the A'(2) and A'' modes are closer to the surface, they must be the modes that point

downwards, which makes them closer to the surface, and therefore A'(1) is upwards.
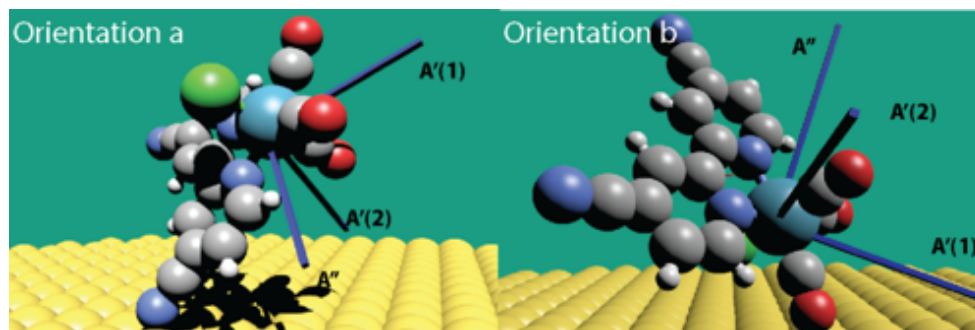
Figure 6.6: Orientations of **1** on gold surface determined from HD 2D SFG and IRRAS measurements, simulated using DFT. Orientation a is preferred. Blue sticks represent the vibrational modes direction

We can further unambiguously determine how the molecules reside on gold surface, using the ensemble-averaged orientation determined from the polarization dependence from IRRAS spectra. IRRAS is a reflection mode IR spectroscopy, which has been used to study thin molecular layers on surfaces. Vibrational modes with various relative angles to the surface normal respond differently to the IR beam with different polarizations. It is established that by measuring the spectral intensity of IRRAS at various IR polarization angles, the ensemble-averaged vibrational modes angle relative to surface normal can be determined.[140] Combining IRRAS and the vibrational modes direction learned from HD 2D SFG, we determine these angles relative to the surface normal in lab frame for A'(1), A'(2) and A" are 68 ± 11, 118 ± 4, $121 \pm 7°$, respectively (SI for details). The vibrational mode angles relative to molecular frame are obtained from B3LYP/LanL2DZ DFT calculation. By rotating **1** from molecular frame to lab frame to match these measured angles, we found that **1** resides on the surface with its Re-Cl axis $45°$ relative to surface normal (SI), where the Cl atom points up and the molecule is anchored through one CN group (orientation a in Figure 6.6). To compare, we also plotted the other "possible" orientation with A'(1) pointing downward (orientation b in Figure 6.6). It is clear that in this configuration neither of the CN groups is close enough to the surface to interact with gold, which suggests this is an unfavorable orientation. This comparison further confirmed our conclusion that the A" and

A'(2) modes point towards to the gold surface and have stronger interactions with the surface.

6.4   Conclusions

In summary, we observed that vibrational peaks from the Re-complex **1** on a gold surface in HD 2D SFG have different center-line slopes, which is caused by that the various vibrational modes experience distinct homogenous broadening but similar inhomogeneous broadening. The drastic difference in homogenous broadening is attributed to the interaction with the image dipole on gold surface, which is highly sensitive to the relative distance of the vibrational modes to the surface. Combining the knowledge of relative distance of vibrational modes to the surface and the polarization dependence of IRRAS spectra, we conclude that the Re-complex should attach on the surface with the Cl atom pointing away from the gold surface. Structure-activity relationships of surface catalysts will be described in our future studies.

Since the adsorbate-metal surface interactions exist in many metal surface based molecular monolayers, we expect HD 2D SFG spectroscopy can be used to determine the ensemble-averaged orientation of the molecules and the strength of the adsorbate-surface interactions on many molecular/metal interfaces. Moreover, since other interactions on interfaces, such as hydrophobic/hydrophilic interactions, or H-bond,[37, 239, 240] can also influence 2D spectral lineshape, we expect similar approaches using HD 2D SFG can also be extended to those interfaces as well. We acknowledge that at least two vibrational modes are needed to be measured to determine the ensemble-averaged orientations, which becomes much easily accessible with the current broadband IR generation techniques.[241, 242] This capability to determine molecular orientation on surfaces and the sensitivity to local interactions with surfaces are expected to provide important new knowledge about a wide range of materials, including notably the area of surface catalysis.

Chapter 6, in full, is a reprint of the material as it appears in The Journal of Physical

Chemistry Letters, 2015. Jiaxi Wang; Melissa L. Clark; Yingmin Li; Camile L. Kaslan; Clifford P. Kubiak; Wei Xiong, American Chemistry Society, 2015. The dissertation author was the primary investigator and author of this paper.

Chapter 7

Solving the "Magic Angle" Challenge in Determining Molecular Orientation Heterogeneity at Interfaces

7.1   Introduction

Molecular orientation at complex interfaces, including heterogeneous catalysts,[243–245] energy materials[246] and biological membranes,[247, 248] is often heterogeneous. The surface molecules can form an ordered monolayer with all molecules tilted at the same angle, monolayers with randomly orientated molecules, or monolayers with complicated orientational distributions. Understanding the complex molecular orientation at these interfaces is critical to reveal the surface structure-function relationships. For example, when enzymes, such as hydrogenase and glucose oxidase, are immobilized onto electrodes to form surface electrocatalysts, it is critical to control their orientations and the corresponding distributions, in order to optimize their charge transfer rate and the mass transportation of reactants and products, for the best activities.[249] Another example is that in biological lipid membranes, lipids adopt new orientations when antimicrobial

peptides intrude into the lipid membranes. Measuring the change of lipid orientation can elucidate the microscopic pictures of how the membrane morphologies respond to the invading peptides, which could have important implications for drug designs.[248]

To describe the molecular orientation of monolayers, a Gaussian distribution is a common model to use. More complex orientational distribution model could exist, but the Gaussian distribution model provides a basic description of the orientation heterogeneity of the molecular monolayers. In the Gaussian distribution model, two physical quantities need to be measured — the mean tilt angle θ_0 and the orientational distribution σ which we refer to as the (θ_0, σ) pair or orientation heterogeneity hereafter.

It is a challenge to measure orientation heterogeneity. For decades, surface-specific vibrational sum frequency generation spectroscopy (referred to as 1D VSFG hereafter)[89, 121, 250–256] has been used to determine the mean tilt angle, under the assumption of a narrow orientational distribution. However, in this case, the knowledge of orientational distribution is lost, and the measured mean tilt angle can deviate from the real mean tilt angle when the orientational distribution is large, which is the well-known "magic angle" challenge.

This issue arises from that 1D VSFG measures an orientation parameter D_1 that is equal to Eq. 7.1:

$$D_1 = \frac{\langle \cos^3 \theta \rangle}{\langle \cos \theta \rangle} = \frac{\int_0^\pi \cos^3 \theta \cdot G(\theta; \theta_0, \sigma) d\theta}{\int_0^\pi \cos \theta \cdot G(\theta; \theta_0, \sigma) d\theta} \tag{7.1}$$

where θ is the angle between the surface normal and the molecular axis, and the bracket means orientational average (integrating the products of cosine functions and a modified Gaussian distribution $G(\theta; \theta_0, \sigma)$ from $0°$ to $180°$).[93, 257–260] Clearly, D_1 is a function of the (θ_0, σ) pair, so a single D_1 cannot warrant a unique solution to both θ_0 and σ.

When the orientational distribution is assumed to be narrow ($\sigma = 0°$), D_1 can be simplified

to $\cos^2\theta_0$, and the mean tilt angle (θ_0) can be calculated. While it works fine for well-ordered, self-assembled monolayers, for most molecular monolayers, this narrow angular distribution assumption is not always valid.[261] In the broad angular distribution case, each D_1 corresponds to many pairs of (θ_0, σ) (solid lines in Figure 7.1a). For instance, if D_1=0.600 is measured, the net orientation can either be $\theta_0 = 39.2°$ with a uniform distribution ($\sigma = 0°$) or any other mean tilt angle with a broad distribution ($\sigma = 90°$) (Figure 7.1b). This 39.2°, referred to as the "magic angle", represents the extreme case of ambiguities in determining orientation heterogeneity,[261] while similar ambiguity also remains for any other D_1 values. As Figure 7.1 has shown, Figure 7.1a: Orientational parameters D_1 (solid line) and D_2 (dashed line) as a function of orientational distribution θ_0 for a series of mean tilt angles θ_0. D_1 and D_2 are calculated based on a modified Gaussian function.[261] Details about this function are described in Section 7.3.4. Figure 7.1b When only D_1=0.600 is measured, it is unknown whether the surface has a uniform orientation distribution with $\theta_0 = 39.2°$ or a broad orientation distribution. However, the D_2 is different for these two scenarios.

In summary, the "magic angle" challenge results in two areas of uncertainty in determining orientation heterogeneity: first, the mean tilt angle measurement can be inaccurate, and second, the orientational distribution is unknown. Although this challenge has been well-known for more than a decade,[261–263] no general solutions to it have been proposed, to the best of our knowledge.

To determine the orientation heterogeneity, another independent quantity besides D_1 needs to be measured, often by using a second spectroscopy. For instance, by combining second harmonic generation (SHG) and another linear spectroscopic method, such as angle-resolved absorbance,[260] linear reflection,[264, 265] or polarization-resolved fluorescence detection,[266–269] the orientational distribution of molecules in thin films can be determined. These methods all rely on spectroscopies that are not intrinsically surface-sensitive and, therefore, have been mainly used to study thin film samples. There have been a few attempts to determine interfacial
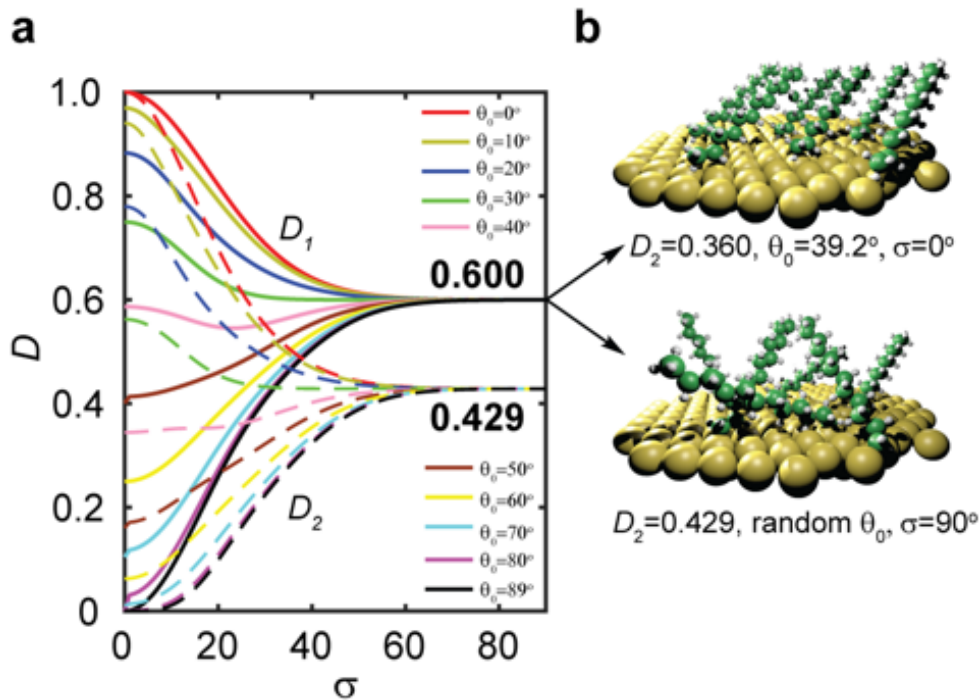
Figure 7.1: The "magic angle" challenge in determining molecular orientation and its solution by using a combination of D_1 and D_2

molecular orientation using non-linear optical methods. Eisenthal and co-workers modified the polarization-resolved SHG by adding a circularly polarized pump pulse. The pump pulse created a non-equilibrium population of surface molecules, which was used to determine the orientational distribution.[270] Also, by taking measurements at various beam incidence angles and carefully calculating parameters related to experimental setup, Wang and co-workers showed that it is possible to extract the molecular orientational distribution from the SHG measurements.[271]

In this work, using surface sensitive heterodyne two dimensional vibrational sum frequency generation (HD 2D VSFG) spectroscopy, we introduce a novel and general method to determine orientation heterogeneity and solve the "magic angle" challenge for surface science, based on a single measurement. In particular, we studied a surface catalytic system for CO_2 reduction as well as solar energy applications. The molecular structure and dynamics of this catalytic system have been investigated extensively with various spectroscopic methods,[140, 219, 221, 272, 273] but its surface molecular orientation heterogeneity has yet to be revealed, which is a critical step

to better understand the surface structure-function relationship. By measuring the orientation heterogeneity, we learned that the surface catalysts form a rigid, ordered monolayer, which could influence the conformational evolution of catalysts in a catalytic cycle. This information that is unavailable previously can shed new insight to the structure-function relationship and have new implications for rationale designs of surface catalysts.

7.2   Theoretical Framework of Orientational Analysis

7.2.1   Measuring Orientation Heterogeneity using HD 2D VSFG

To determine surface molecular orientation heterogeneity, the key is to measure a second independent orientation parameter along with D_1. We used HD 2D VSFG to determine the second orientation parameter $D_2 = \langle \cos^5 \theta \rangle / \langle \cos \theta \rangle$. Since D_1 and D_2 have different dependence on θ_0 and σ (Figure 7.1a), a unique pair of θ_0 and σ can be determined.

The recently developed HD 2D VSFG spectroscopy[96, 98, 99, 274, 275] is the core measurement that enables surface molecular orientation heterogeneity characterization. The experimental detail of this spectroscopic technique will be described in Section 3.3. Overall, fourth-order susceptibilities ($\chi_{eff}^{(4)}$) are measured in HD 2D VSFG. Similar to 1D VSFG, which measures second-order susceptibilities ($\chi_{eff}^{(2)}$), these even-order nonlinear optical signals only survive in non-centrosymmetric environments, such as interfaces. Therefore, both 1D and HD 2D VSFG spectroscopies are interface-specific vibrational spectroscopies whose signals depend on the molecular orientations.[96, 251, 257, 276]

The key relationship that enables HD 2D VSFG spectroscopy to measure surface molecular orientation heterogeneity is that $\chi_{eff}^{(2)}$ and $\chi_{eff}^{(4)}$ can be expressed as a linear combination of $\langle \cos \theta \rangle$, $\langle \cos^3 \theta \rangle$ and $\langle \cos^5 \theta \rangle$ (Eq. 7.2).

$$\chi_{eff,i}^{(2)} = a_i \langle \cos \theta \rangle + b_i \langle \cos^3 \theta \rangle$$

$$\chi_{eff,i}^{(4)} = c_i \langle \cos \theta \rangle + d_i \langle \cos^3 \theta \rangle + e_i \langle \cos^5 \theta \rangle$$

(7.2)

These equations resulted from a series of Euler transformations to convert molecular frame hyperpolarizabilities to lab frame susceptibilities, where a_i, b_i, c_i, d_i and e_i are constants that depend on the molecular hyperpolarizabilities of the ith vibrational mode (Section 7.3.3). Since heterodyne 1D VSFG is simultaneously measured as heterodyne 2D VSFG is taken, both $\chi_{eff}^{(2)}$ and $\chi_{eff}^{(4)}$ can be determined from the same HD 2D VSFG experiments.

By taking the ratios of χ_{eff} between two vibrational modes,[277] or ratios of χ_{eff} of a single vibrational mode under different polarization combinations,[257] we obtain the key formula (Eq. 7.3) to extract D_1, D_2 from $\chi_{eff}^{(2)}$ and $\chi_{eff}^{(4)}$:

$$\frac{\chi_{eff,1}^{(2)}}{\chi_{eff,2}^{(2)}} = \frac{a_1 + b_1 \langle \cos^3 \theta \rangle}{a_2 + b_2 \langle \cos^3 \theta \rangle} = \frac{a_1 + b_1 \cdot D_1}{a_2 + b_2 \cdot D_1}$$

$$\frac{\chi_{eff,1}^{(4)}}{\chi_{eff,2}^{(4)}} = \frac{c_1 + d_1 \langle \cos^3 \theta \rangle + e_1 \langle \cos^5 \theta \rangle}{c_2 + d_2 \langle \cos^3 \theta \rangle + e_2 \langle \cos^5 \theta \rangle} = \frac{c_1 + d_1 \cdot D_1 + e_1 \cdot D_2}{c_2 + d_2 \cdot D_1 + e_2 \cdot D_2}$$

(7.3)

D_1 and D_2 have different dependence on θ_0 and σ which is why θ_0 and σ can be solved from Ds. The dependence of D_1 and D_2 on θ_0 and σ is summarized as 3D surface plots (Figure 7.2), which we will use to demonstrate the graphic solution for searching (θ_0, σ) pairs below. The D-θ_0-σ surface plot can be roughly divided into two regions: region I with $\sigma \leq 40°$ and region II with $\sigma \text{¿} 40°$. In region I, because of the unique values of D_1 and D_2, the (θ_0, σ) pair can be unambiguously determined. In region II, D_1 and D_2 converge to 0.600 and 0.429 asymptotically, which makes them lose the one-to-one correlation with the (θ_0, σ) pair. Although the (θ_0, σ) pair cannot be uniquely determined in region II, the two asymptotic numbers (D_1=0.600 and

D_2=0.429) are unique signatures for broad orientational distribution. For instance, one important consequence of this asymptotic pair is solving the above-mentioned ambiguity of the "magic angle". When D_1 and D_2 are both measured, if the interfacial molecules all tilt at 39.2° with a narrow distribution, then D_1 should be 0.600 and D_2 should be 0.360 (when $\sigma = 0°$, $D_2 = D_1^2$); otherwise, with a broad angular distribution, D_1 and D_2 should be close to 0.600 and 0.429, respectively (Figure 7.1b). Therefore, the orientation disorder can be determined, and there is no "magic angle" ambiguity when D_1 and D_2 are measured together.
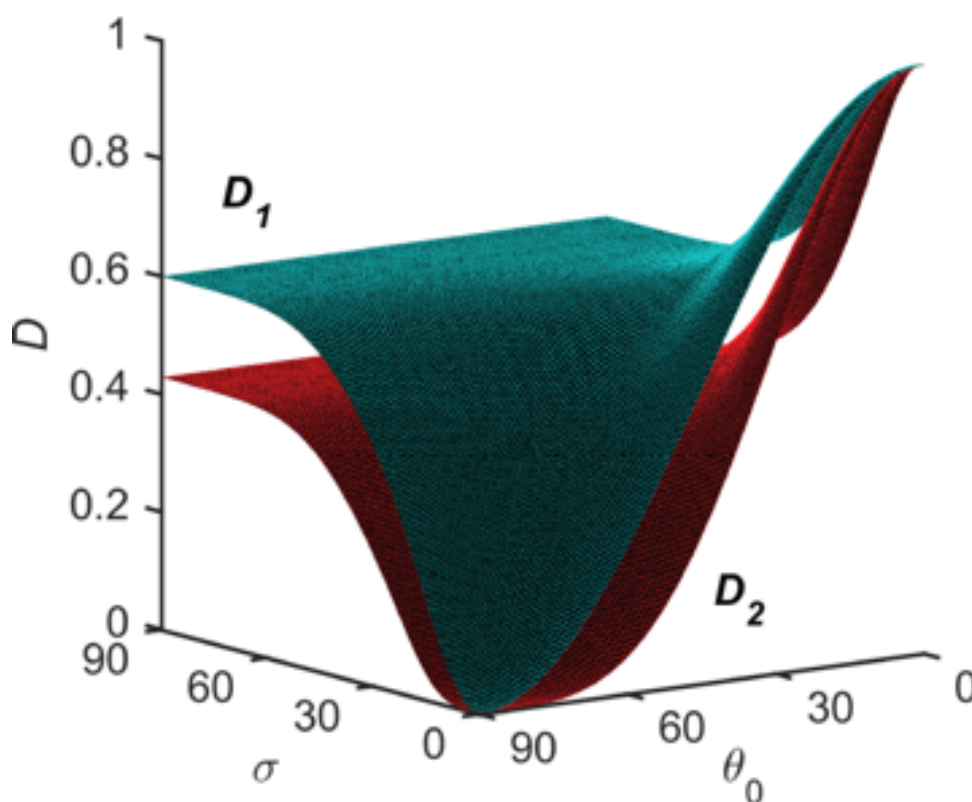
Figure 7.2: 3D surface of D_1 and D_2 as a function of mean tilt angle θ_0 and orientational distribution σ. D_1 is plotted in blue and D_2 in red. The projection of these surfaces on the D-σ plane is equivalent to Figure 7.1a

7.2.2 Calculation of molecular hyperpolarizability using Gaussian 09

The values of hyperpolarizabilities determines the coefficient in Eq. 7.2 and 7.3, The molecular hyperpolarizability tensor elements for A'(1) and A'(2) modes are determined based on the following equation:[86]

$$
\begin{aligned}
\beta_{ijk}^{q} &\propto \frac{1}{\omega_q} \cdot \frac{\partial \alpha_{ij}}{\partial Q_q} \cdot \frac{\partial \mu_k}{\partial Q_q} \\
\beta_{ijklm}^{q} &\propto \frac{1}{\omega_q} \cdot \frac{\partial \alpha_{ij}}{\partial Q_q} \cdot \frac{\partial \mu_k}{\partial Q_q} \cdot \frac{\partial \mu_l}{\partial Q_q} \cdot \frac{\partial \mu_m}{\partial Q_q}
\end{aligned}
\tag{7.4}
$$

where i, j, k, l, m = x, y, z; ω_q and Q_q are the vibrational frequency and the normal coordinates of the qth vibrational mode.

Energy and geometry optimization of Re-complex molecule were performed using B3LYP functional and LANL2TZ basis set with Gaussian 09. Dipole derivatives ($\partial \mu / \partial Q_q$) and polarizability derivatives ($\partial \alpha / \partial Q_q$) of each vibrational mode were obtained using the keyword 'polar' and 'iop(7/33=1)'. We calculated the hyperpolarizability and depolarization ratio using the following functional and basis set combinations: B3LYP/LanL2TZ, B3LYP/Def2QZVP, B3LYP/Def2TZVP, M06L/LanL2TZ, M06L/Def2QZVP and M06L/Def2TZVP. In orientational analysis, we used the values calculated from B3LYP/LanL2TZ, which have the best agreement with the experimental measured depolarization ratios.

7.3 Methods

7.3.1 SFG spectroscopy

The detailed description of HD 2D VSFG spectroscopy is described in details in Section 3.3. The HD 1D SFG spectra can be extracted by adding the two phase cycled pump probe

spectra together, where the 4th order signals cancel out and only leaves the 2nd order HD 1D SFG spectra.

7.3.2 Depolarization ratio measurement from Raman spectroscopy

We use the experimental depolarization ratio to compare with the calculated results in DFT, in order to determine the accuracy of the calculation and choose the best basis set/functional for the hyperpolarizability calculation.

Depolarization experiments were collected by Prof. Michael Tauber and his Ph.D. student Megan Stone. Polarized off-resonance Raman spectra were acquired with 647.09 nm (15,454 cm^{-1}) excitation, produced by a mixed krypton/argon gas-ion laser (Laser Innovations/Coherent; Innova 70C Spectrum). The wavelength was selected with an intracavity prism, and further isolated with a 647.1 nm bandpass filter (Semrock, MaxLine) placed in the beam path near the output of the laser. A right-angle geometry was used for the excitation and detection of scattered light. A spherical lens with focal length 80 mm was used to focus the laser beam into the bottom of a 1×1 cm fluorescence cuvette that contained solvents for calibrations, or solutions of Re(4,4'-dicyano-2,2'-bipyridine)(CO)$_3$Cl. Raman scattering was collected and collimated with an F/1.2 camera lens (Canon FD 85 mm). A doublet achromat with 300 mm focal length (CVI-Melles Griot, 01LAO667) focused the light at the entrance slit of the spectrograph. Three optics were placed between the 300 mm lens and the entrance slit. First, a dichroic polarizer (OptoSigma, 069-0120) mounted in a rotation stage was used to analyze the parallel (horizontally polarized) and perpendicular (vertically polarized) Raman scattered light. Second, a two-piece quartz wedge (OptoSigma, 068-6770) scrambled the polarization to compensate for different efficiencies of the spectrograph to parallel and perpendicular light. Third, a 647.1 nm long-pass filter (Semrock, RazorEdge) rejected the excitation line. The spectrograph (JY Horiba, iHR320) had a 320 mm focal length, and a single holographic grating with 1200 gr/mm groove density, 500 nm blaze. The detector was an open-electrode CCD (JY Horiba, Synapse). Raman shifts were

calibrated based on six emission lines from a neon lamp (Oriel), and several Raman bands,[278] from a 50:50 mixture of acetonitrile and toluene.

The rotation of the polarizer was optimized while collecting one-second spectra of carbon tetrachloride (Sigma Aldrich, $\geq$99.9% pure). The entrance slit of the spectrograph was set to 50 um (resolution $\approx$4 cm^{-1}). After optimized positions were found, perpendicular and parallel spectra were recorded. The depolarization ratio of the 314 cm^{-1} and 459 cm^{-1} bands were determined by integrating the bands (perpendicular/parallel) and were 0.75 and <0.01, respectively. These depolarization ratios matched known values.[279] Repeat measurements of CCl$_4$ before and after collection of the rhenium samples yielded consistent depolarization ratios. Additionally, to check the performance of the system further in the red ($\approx$720 nm), Raman spectra of benzene were collected and the 1585+1604 cm^{-1} bands were analyzed. This pair of bands had a depolarization ratio of 0.75, as expected.[278, 279]

The depolarization ratios of Re(4,4'-dicyano-2,2'-bipyridine)(CO)$_3$Cl were recorded in DMSO solution at two concentrations, 2 mM and 26 mM (Table 7.1, values are determined by integrating the bands of polarized Raman spectra acquired with 647.09 nm excitation). The laser power at the sample was 45 mW, and the entrance slit was 100 μm. Each polarization was collected for a total of 10-20 minutes, and solvent-only spectra were also acquired for the same time. Spectra were processed using Igor Pro (WaveMetrics). Peaks caused by cosmic rays were removed manually from 1- or 2-minute acquisitions, and the acquisitions for the full collection time were then averaged. The solvent bands were subtracted from the spectra of Re(4,4'-dicyano-2,2'-bipyridine)(CO)$_3$Cl solutions by appropriate scaled subtraction (Figure 7.3, The y-axis units are counts per 120-second acquisition time, and each of the two spectra are the average of 10 acquisitions (total collection time 20 minutes per spectrum). The perpendicular spectrum is offset +90,000 counts.). A broad luminescence background was removed from the solvent-free spectra using a spline fit.
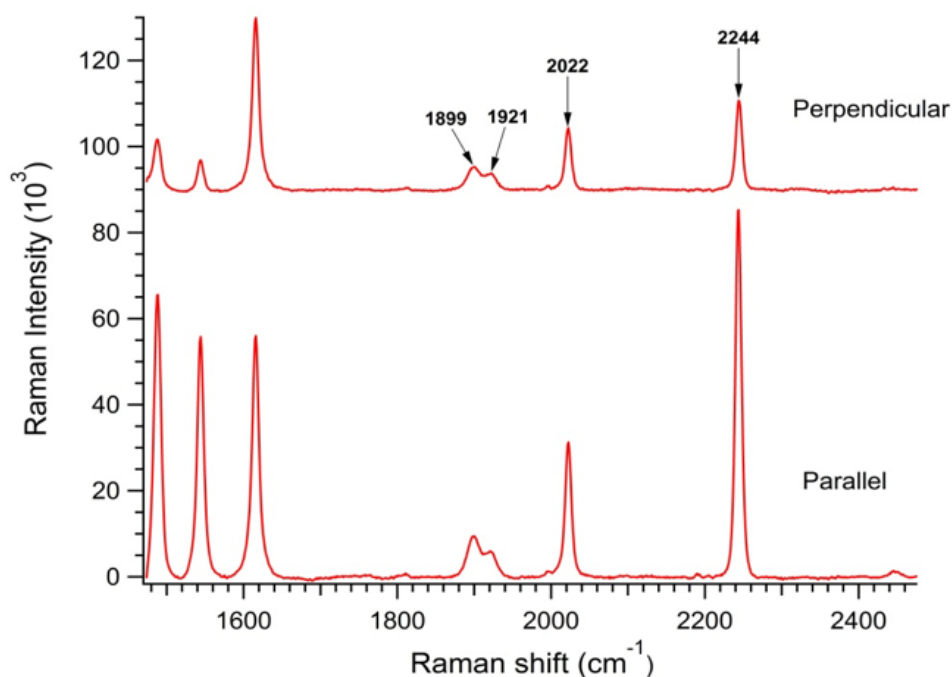
Figure 7.3: Polarized Raman spectra of Re(4,4'-dicyano-2,2'-bipyridine)(CO)$_3$Cl in DMSO (26 mM) acquired with 647.09 nm excitation. Spectra are shown after subtraction of solvent bands and a broad luminescence background.

Table 7.1: Depolarization Ratios of Selected Bands of Re(4,4'-dicyano-2,2'-bipyridine)-(CO)$_3$Cl at Two Different Concentrations.

	A'(2)	A"	A'(1)
2mM	0.55	0.58	0.44
26mM	0.59	0.57	0.45

7.3.3 Euler Transformation between Laboratory Coordinate Frame and Molecular Coordinate Frame.

The three stretching modes (Figure 4.6) related to carbonyls in the Re(4,4'-dicyano-2,2'-bipyridine)(CO)$_3$Cl molecule are labeled as A'(2), A" and A'(1) with center frequency of 1911,

1931 and 2020 cm^{-1} in 2D SFG spectra. A'(2) is an out-of-phase symmetric stretch, A' is an anti-symmetric stretch and A'(1) is an in-phase symmetric stretch.[74, 221] In this work we focus on analyzing A'(1) and A'(2) modes.

The three carbonyls in the Re-complex have an approximated C_{3v} symmetry, and the transition dipole moments of the three stretching modes are approximately perpendicular to each other. As shown in Figure 7.4, in the molecular coordinate frame, z axis is defined along the transition dipole moment of A'(1) mode, which also coincides with the approximated C_3 symmetry axis; molecular x and y axes are defined along the transition dipole moments of A'(1) and A' modes, respectively. In the laboratory coordinate frame, Z axis is defined along the surface normal and X axis is in the incidence plane perpendicular to Z. The relationship between XYZ and xyz frame are described by three angles: tilt angle θ, in-plane rotation angle ϕ and twist angle φ.

In the SFG measurements, all beams were held at p polarization. As the Fresnel factor is much larger in Z direction compared with those in X and Y directions for all beams, both effective second-order ($\chi^{(2)}_{eff}$) and fourth-order ($\chi^{(4)}_{eff}$) susceptibilities are dominated by singe susceptibility tensor element:

$$\chi^{(2)}_{eff} \approx L_{ZZ}(\omega_1)L_{ZZ}(\omega_2)L_{ZZ}(\omega_3)\sin\beta_1\sin\beta_2\sin\beta_3\chi^{(2)}_{ZZZ}$$
$$\chi^{(4)}_{eff} \approx L_{ZZ}(\omega_1)L_{ZZ}(\omega_2)L_{ZZ}(\omega_3)L_{ZZ}(\omega_4)L_{ZZ}(\omega_5)\sin\beta_1\sin\beta_2\sin\beta_3\sin\beta_4\sin\beta_5\chi^{(4)}_{ZZZZZ}$$

(7.5)

where $L_{ZZ}(\omega_i)$ and β_i are the Fresnel factor and incidence/reflection angle of the ith beam. $\chi^{(2)}_{ZZZ}$ and $\chi^{(4)}_{ZZZZZ}$ are related to second-order ($\beta^{(2)}$) and fourth-order ($\beta^{(4)}$) molecular polarizabilities through the following equations:

$$\chi_{ZZZ}^{(2)} = N\langle\beta^{(2)}\rangle = N\sum_{ijk}\langle R_{Zi}R_{Zj}R_{Zk}\rangle\beta_{ijk}^{(2)}$$

$$\chi_{ZZZZZ}^{(2)} = N\langle\beta^{(4)}\rangle = N\sum_{ijklm}\langle R_{Zi}R_{Zj}R_{Zk}R_{Zl}R_{Zm}\rangle\beta_{ijklm}^{(4)}$$

(7.6)

where i, j, k, l, m = x, y, z; N is the number density of Re-complex on the gold surface, bracket means taking orientationally averaged value, and R is the element of Euler transformation matrix based on the geometry defined in Figure 7.4.
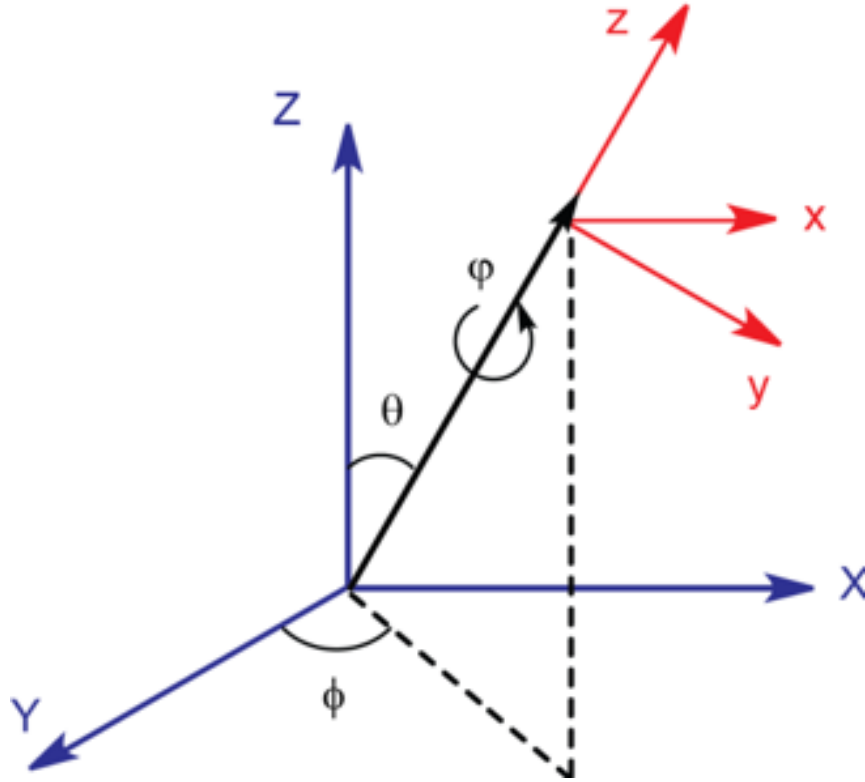
Figure 7.4: The relationship between XYZ frame and xyz frame.

Assuming Re-complex has uniform distribution in the in-plane rotation angle ϕ and twist angle φ, Eq. 7.6 can be simplified for mode A'(1) and A'(2), which are employed to determine the orientational parameters D_1 and D_2. For A'(1) mode and A'(2) mode, respectively:

$$\chi_{ZZZ}^{(2)}[A'(1)] = N[(\frac{\beta_{xxz}^{(2)} + \beta_{yyz}^{(2)}}{2})\langle\cos\theta\rangle + (\beta_{zzz}^{(2)} - \frac{\beta_{xxz}^{(2)} + \beta_{yyz}^{(2)}}{2})\langle\cos^3\theta\rangle]$$

$$\chi_{ZZZZZ}^{(2)}[A'(1)] = N[(\frac{\beta_{xxzzz}^{(4)} + \beta_{yyzzz}^{(2)}}{2})\langle\cos^3\theta\rangle + (\beta_{zzzzz}^{(4)} - \frac{\beta_{xxzzz}^{(4)} + \beta_{yyzzz}^{(4)}}{2})\langle\cos^5\theta\rangle]$$

(7.7)

$$\chi_{ZZZ}^{(2)}[A'(2)] = N[(\beta_{xzx}^{(2)})\langle\cos\theta\rangle + (-\beta_{xzx}^{(2)})\langle\cos^3\theta\rangle]$$

$$\chi_{ZZZZZ}^{(4)}[A'(2)] = N[(\frac{3\beta_{xzxxx}^{(4)}}{4})\langle\cos\theta\rangle + (-\frac{3\beta_{xzxxx}^{(4)}}{2})\langle\cos^3\theta\rangle + (\frac{3\beta_{xzxxx}^{(4)}}{4})\langle\cos^5\theta\rangle]$$

(7.8)

7.3.4 Modified Gaussian Distribution.

A modified Gaussian function proposed by Simpson and Rowlen was employed to describe the distribution of molecular orientation.[261] The representations are shown as follows:

$$f(\theta) = \frac{1}{\sqrt{2\pi}\sigma} e^{\frac{-(\theta-\theta_0)^2}{2\sigma^2}}$$

$$f'(\theta) = \sum_{n=-4}^{4} f(2\pi n + \theta) + f(2\pi n - \theta)$$

(7.9)

Where θ_0 is the mean tilt angle and σ describes the distribution width. The net distribution function $f'(\theta)$, which is valid in the range from 0 to π, is developed from the normal Gaussian function $f(\theta)$. The values of $\langle\cos\theta\rangle$, $\langle\cos^3\theta\rangle$ and $\langle\cos^5\theta\rangle$ at different (θ_0, σ) pairs are calculated using Matlab through the following equation:

$$\langle\cos^m\theta\rangle = \sum_0^\pi \cos^m\theta \cdot f'(\theta) \cdot \sin\theta d\theta$$

(7.10)

93

Where $\sin\theta$ is a weighting function accounting for the fact that molecules may orient in both XZ and YZ planes.

7.3.5   SFG Spectra Fitting.

The 1D and 2D SFG spectra shown in Figure 7.6 are fitted using the equation [280]:

$$\chi = \sum_{i=1}^{3} \frac{B_i \gamma_i}{(\omega - \omega_i)^2 + \gamma_i^2} \tag{7.11}$$

where B_i and γ_i represent the amplitude, center frequency and peak width of the ith vibrational mode, respectively. All fitting parameters are shown in Table 7.2. $\chi_{eff}^{(2)}[A'(1)]/\chi_{eff}^{(2)}[A'(2)]$ and $\chi_{eff}^{(4)}[A'(1)]/\chi_{eff}^{(4)}[A'(2)]$ are calculated using the following equation:

$$\frac{\chi_{eff}^{(2)}[A'(1)]}{\chi_{eff}^{(2)}[A'(2)]} = \left(\frac{B[A'(1)]}{\gamma A'(1)]}\right)/\left(\frac{B[A'(2)]}{\gamma A'(2)]}\right) \tag{7.12}$$

Table 7.2: Fitting Parameters for 1D and 2D Heterodyned SFG Spectra

Mode	A'(2)			A'(1)		
	B	ω	γ	B	ω	γ
1D	31.3(6)	1912	52.8(7)	-48.1(5)	2011	61.8(6)
2D	2.5(2)	1911	10.3(7)	-3.05(9)	2020	9.7(4)

7.3.6   Calculation of Molecular Hyperpolarizability Tensor Elements.

Energy and geometry optimization of Re-complex molecule were performed using B3LYP functional and LANL2TZ basis set with Gaussian 09. Dipole derivatives $(\partial\mu/\partial Q_q)$ and polarizability derivatives $(\partial\alpha/\partial Q_q)$ of each vibrational mode were obtained using the keyword 'polar' and 'iop(7/33=1)'. The and values for A'(2) (mode 74 in Gaussian log file) and A'(1) (mode 76) modes are shown in Table 7.3.

Table 7.3: Dipole Derivatives $(\partial\mu/\partial Q_q)$ and Polarizability Derivatives $(\partial\alpha/\partial Q_q)$ for A'(1) and A'(2) Modes Determined from ab initio Calculation

Mode 74 (A'(2))			
Dipole derivatives	3.07650D+01	3.89478D-03	-3.04117D+00
Polarizability derivatives	-0.988878D+00	0.505546D-03	0.241308D+01
	0.505546D-03	0.197090D+01	-0.338132D-03
	0.241308D+01	-0.338132D-03	0.228602D+01
Mode 76 (A'(1))			
Dipole derivatives	-4.24616D+00	1.33888D-03	-3.61394D+01
Polarizability derivatives	-0.970416D+00	-0.419215D-04	0.117419D+01
	-0.419215D-04	0.141946D+01	0.173584D-03
	0.117419D+01	0.173584D-03	0.440365D+01

7.4 Results and Discussion

Based on the theory and experiments presented above, we can extract the orientation heterogeneity of the Re(4,4'-dicyano-2,2'-bipyridine)(CO)$_3$Cl monolayer, self-assembled on a gold slide (Figure 7.5b. θ_0 is the angle between C$_3$ axis and surface normal.), from its HD 2D VSFG spectrum (Figure 7.5c. HD 2D VSFG spectra of the Re complex in the carbonyl stretch region.).[74] The peaks at 2020, 1931, and 1911 cm^{-1} along the diagonal of the HD 2D VSFG spectrum originate from the A'(1), A", and A'(2) modes of Re(CO)$_3$ moiety, respectively, which we can use to extract χ_{eff} and to reveal the orientation heterogeneity of the surface molecules. To extract χ_{eff}, we took diagonal cut of the HD 2D VSFG spectrum (Figure 7.5c), and extract heterodyne 1D VSFG spectrum directly from HD 2D VSFG raw data.
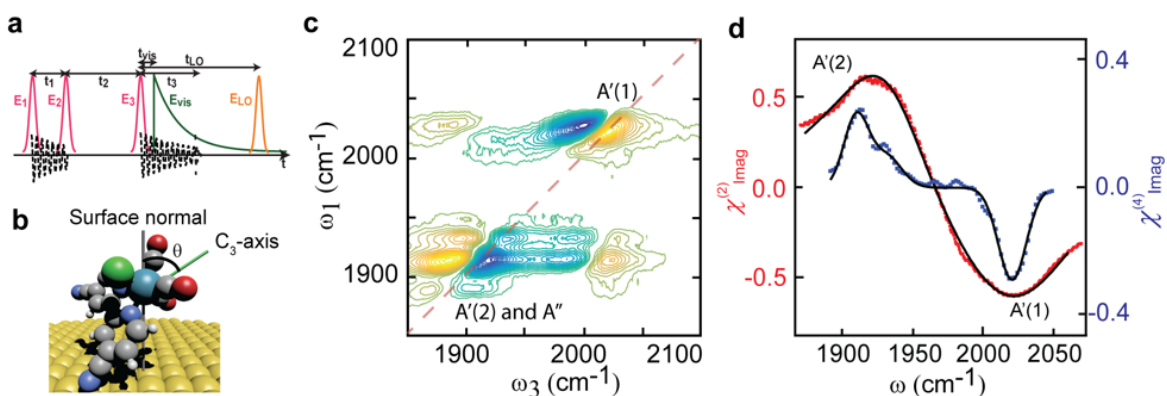
Figure 7.5: Illustration and results of HD 2D VSFG spectroscopy (pulse sequence) and the surface catalysis system. (Detailed description in main text)

We determined the χ_{eff} ratios of two vibrational modes by fitting the A'(1) and A'(2) peaks in both the heterodyne 1D VSFG spectrum and the diagonal cut of the HD 2D VSFG spectrum (Figure 7.5d. Heterodyne 1D (red dots) and diagonal cut of HD 2D (blue dots) VSFG spectra. The 1D spectrum has been significantly broadened by surface inhomogeneity. Solid lines represent theoretical fitting). From the fittings, we found $\chi_{eff}^{(2)}[A'(1)] / \chi_{eff}^{(2)}[A'(2)]$ = -1.31 $\pm$ 0.04 and $\chi_{eff}^{(4)}[A'(1)] / \chi_{eff}^{(4)}[A'(2)]$ = -1.3 $\pm$ 0.1. Since all beams were held at p polarization, and the

Fresnel factor on gold is strong in the Z direction, we found $\chi_{eff}^{(2)} \propto \chi_{ZZZ}^{(2)}$ and $\chi_{eff}^{(4)} \propto \chi_{ZZZZZ}^{(4)}$. For the case of Re-complex on gold surface, we derived the equation of $\chi_{ZZZ}^{(2)}$ and $\chi_{ZZZZZ}^{(4)}$, by taking a uniform distribution in the in-plane rotation and twist angles, and can be written explicitly as Eq.7.7 and Eq.7.8

By substituting Eq.7.7 and Eq.7.8 into Eq.7.3 and using the numerical value of hyperpolarizabilities calculated by density functional theory (DFT) (B3LYP/LANL2TZ basis set, details in supporting information),[277] we derived the numerical relationships between $\chi_{ZZZ,1}^{(2)}$ / $\chi_{ZZZ,2}^{(2)}$, $\chi_{ZZZZZ,1}^{(4)}$ / $\chi_{ZZZZZ,2}^{(4)}$ and D_1, D_2. We found that $D_1 = 0.364 \pm 0.008$ and $D_2 = 0.14 \pm 0.02$.

Next, we used the measured D_1 and D_2 to extract all the qualified (θ_0, σ) pairs from the D_1 and D_2 surfaces. With $D_1 = 0.364$ and $D_2 = 0.14$, we drew two planes that were parallel to the θ_0-σ plane at D'= 0.364 and D''= 0.14 to intersect the D_1 and D_2 surfaces (Figure 7.6a and b), respectively. The projections of intersecting lines on the θ_0-σ plane represent the qualified (θ_0, σ) pairs that have D_1=D' and D_2=D'' (Figure 7.6c, the projections of both intersecting lines on the θ_0, σ plane), and the results agree with our previous statement that there are many combinations of (θ_0, σ) pairs to match a single D_1 value. However, there is only one intersection point (θ_0=53°, σ=5°) between the intersecting lines of D_1 and D_2 that represents the unique (θ_0, σ) pair that satisfies both D_1=D' and D_2=D''.

When taking into account the uncertainty of measured D_1 and D_2, the projected intersecting lines of D_1 and D_2 become stripes on the θ_0-σ plane. Thus the unique intersection point turns into an intersection region, shown as the shaded area in Figure 4d. As a result, θ_0 was found to be in the region of 52-57°, while the range of σ was different for each θ_0 value. The maximum uncertainty of σ is $\pm 4°$, when θ_0 is about 53.4°. This result of θ_0=53°, σ=5° suggests that the Re-complex forms a well-ordered layer. In this case, if assuming a narrow orientational distribution, the mean tilt angle is calculated to be 53°, same as what is determined by our new method, but the orientational distribution information is missing. Most recently, the Lian, Batista and Kubiak research groups studied the orientation of the same molecule self-assembled on a gold
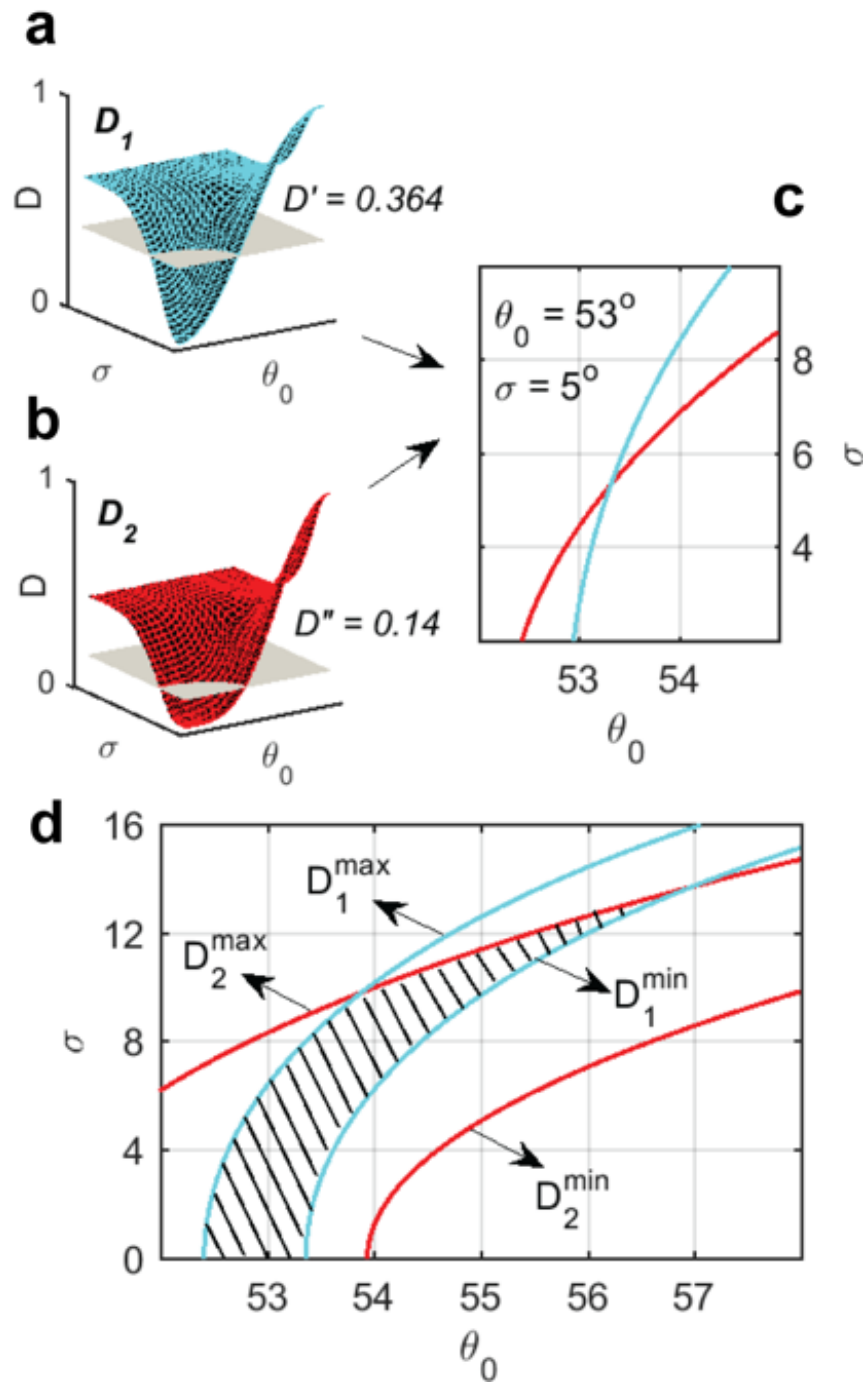
Figure 7.6: Determination of the unique (θ_0, σ) pair for $D_1=0.364$ and $D_2=0.14$. $D'=0.364$ plane in D_1 surface (a) and $D''=0.14$ plane in D_2 surface (b). The region of qualified (θ_0, σ) pairs for $D_1 = 0.364 \pm 0.008$ and $D_2 = 0.14 \pm 0.02$ is marked in (d)

surface using a combination of 1D VSFG and DFT simulation, and the angle between the plane of the bi-pyridine ligand and surface normal was found to be 63°.[221] However, no information about orientation heterogeneity was reported.

The well-ordered monolayer revealed by our work indicates that there is one energetic favorable orientation for all the Re-complex on the gold surface. Because HD 2D VSFG measures a large ensemble average of interfacial molecules, under the ergodic condition, we can conclude that the Re-complexes undergo very small orientation fluctuations over time and are relatively rigid. This could be originated from that the Re-complexes use very short CN groups as the anchoring moieties. Short anchoring groups are often used to increase charge transfer rate, by reducing the electrode-catalysts distance, but they could lead to little flexibility for the catalysts to sample various orientations, as observed from our measurement. It is important for catalysts to be flexible to accommodate different conformations to facilitate reactions.[213] Thus, an optimized anchoring group selection could exist to balance the charge transfer rate, and the flexibility of catalysts. Our work shows the potential of using HD 2D SFG to assess the flexibility of the surface catalysts.

Although the orientaional distribution of the Re-catalysts studied here is narrow and the mean tilt angle measured using HD 2D VSFG is essentially the same as the result from heterodyne 1D VSFG when a narrow distribution is assumed, we note that the discrepancy of the mean tilt angle determined by using our method and the 1D SFG method can be large. For instance, in a hypothetical scenario, when $D_1=0.415$ is measured and the narrow distribution is assumed, the calculated mean tilt angle is 50°. However, if, with the same sample, $D_2=0.23$, then the angle would be 67° with distribution of 27°, which means that the angle determined from the narrow distribution assumption has a systematic error of 25%.

There are three important aspects that are influential to the orientation heterogeneity measurement. First, to properly measure surface molecular orientation heterogeneity, it is important to implement heterodyne detection, rather than homodyne detection. In heterodyne and

homodyne detections, the measured 2D VSFG signals can be expressed as:[98]

$$S_{heterodyne} \approx E_{2DSFG} \cdot E_{LO} \propto \chi_{eff}^{(4)}$$

$$S_{homodyne} \approx E_{2DSFG} \cdot E_{1DSFG} \propto \chi_{eff}^{(4)} \cdot \chi_{eff}^{(2)}$$

(7.13)

When heterodyne detection is used, the measured signal is proportional to $\chi_{eff}^{(4)}$, but when homodyne detection is used, the 1D VSFG signal essentially acts as a local oscillator to heterodyne the 2D VSFG signal. Therefore, the measured signal is proportional to $\chi_{eff}^{(4)} \times \chi_{eff}^{(2)}$. As a result, it is difficult to disentangle these two terms and determine the $\chi_{eff}^{(4)}$ ratio from homodyne 2D VSFG.

Second, the values of D_1 and D_2 are the keys to retrieving an accurate (θ_0, σ) pair, which is affected mostly by the signal-to-noise ratio (S/N) in the measurements. This becomes most apparent when σ is relatively large, making both D_1 and D_2 converge and a small change in the D values could lead to a large difference. In our measurements, the S/N of HD 2D VSFG is about 20, which leads to the same order of magnitude of uncertainty in the spectral fitting mentioned above. Therefore, the experimental noise does not lead to additional uncertainty in the orientation heterogeneity measurements. We note, however, that the relation between D_1 and D_2 is restricted. For instance, a Gaussian distribution requires that $D_1{}^2 \leq D_2 \leq D_1$. This relation has to be satisfied if a Gaussian distribution is appropriate to describe the orientation heterogeneity of the interfacial molecules; otherwise, other models have to be proposed.

Third, another source of uncertainty comes from the value of hyperpolarizability. Here, we used high level DFT calculations to determine the hyperpolarizability, which is a common approach used in Raman and 1D VSFG spectroscopic studies.[281–286] The accuracy of hyperpolarizability and the resulted (θ_0, σ) pair depends on the choice of basis sets. To evaluate that, we tested basis sets at different levels. The results of hyperpolarizability, Raman depolarization

ratio, and corresponding (θ_0, σ) pair is summarized in Table 7.4. We found the calculated hyper-polarizability converges to a level where the variation of hyperpolarizabilities from different basis sets does not make significant changes to the (θ_0, σ) pair. Another alternative for determining hyperpolarizability is to derive it from the experimental Raman depolarization ratio.[257] How-ever, this method is limited to symmetric vibrational modes with perfect C_{3v} or C_∞ symmetry. Since the vibrational modes of Re-complex studied here do not have a perfect C_{3v} symmetry, the Raman depolarization approach cannot be directly applied for our study. Nevertheless, a comparison between the experimental measured and the DFT calculated depolarization ratios could indicate the accuracy of the hyperpolarizability calculation. In our work, we found that the B3LYP/LanL2TZ functional/basis set calculates the depolarization ratio of the A'(1) and A'(2) modes to be 0.34 and 0.50, respectively, which matches with the experimental measured ratios - 0.44 and 0.55, best. (Table 7.4) Therefore, we chose to report the orientation heterogeneity determined from B3LYP/LanL2TZ as our best result. Further investigations of determining hyperpolarizabilities of complex molecules that are lack of rigorous symmetries is important, in order to accurately determine molecular heterogeneity, but it is out of the scope of this initial report.

7.5   Conclusions

The method in this work can be applied broadly to determine the orientation heterogeneity of interfacial molecules in systems consisting of water, solid state materials and biological molecules, many of which have been investigated by HD 2D VSFG spectroscopy.[96, 99, 101, 218, 274, 275, 287, 288] Therefore, the orientation analysis presented here can be directly applied to these spectral regimes. In addition, since only the diagonal cuts of HD 2D VSFG are analyzed to obtain the orientation heterogeneity, in principle, the same method can be applied to IR pump-SFG probe experiments[273] when there is no coupling between vibrational modes. This

Table 7.4: D_1, D_2, θ_0 and σ Determined Using Different Functionals and Basis Sets

	Experimental value	B3LYP/ LanL2TZ	B3LYP/ Def2QZVP	B3LYP/ Def2TZVP	M06L/ LanL2TZ	M06L/ Def2QZVP
$\rho A'(1)$	0.44	0.35	0.32	0.33	0.33	0.30
$\rho A'(2)$	0.55	0.50	0.49	0.50	0.51	0.51
D_1	—	0.364	0.335	0.337	0.336	0.331
D_2	—	0.14	0.13	0.13	0.14	0.12
θ_0	—	53°	56°	56°	58°	56°
σ	—	5°	9°	9°	12°	7°

extension enables the orientation heterogeneity measurement by a more established technique than HD 2D VSFG.

In summary, we demonstrate that the orientation heterogeneity of molecules at interfaces can be determined using HD 2D VSFG. In particular, we studied the monolayer of Re(4,4'-dicyano-2,2'-bipyridine)(CO)$_3$Cl on a gold electrode and found that it forms a fairly ordered structure, which has implications to the surface structure-function relationships. This new advancement solves the long-standing "magic angle" challenge in 1D VSFG spectroscopy. With the growing popularity of HD 2D VSFG spectroscopy in the surface science community,[74, 94, 96, 98, 99, 101, 104, 106, 218, 274–276, 287, 288] this new method will contribute significantly in determining the molecular conformations at interfaces.

Chapter 7, in full, is a reprint of the material as it appears in The Journal of Physical Chemistry C, 2016. Zhiguo Li; Jiaxi Wang; Yingmin Li; Wei Xiong, American Chemistry Society, 2016. The dissertation author was the primary investigator and author of this paper.

Chapter 8

Ultrafast Intercavity Polariton Nonlinear Interactions

8.1   Introduction

Polaritons—quasiparticles formed by photon cavity modes strongly coupling to molecular modes, are unique because polaritons possess not only both photon and molecular characters, but also a combination of them which can lead to novel properties that is exclusive to polaritons, e.g. room temperature condensations. Because of these unique properties, polaritons have potentials for ultrafast optical switches,[289] quantum communication,[290] and nonlinear interactions between polaritons are the key components for realization. Here, by taking advantages of both the delocalization of photon cavity modes and nonlinearity of molecular modes, e.g. a portion of molecules are coupled to multiple cavity modes adjacent to each other, we achieve nonlinear interactions between polaritons residing in adjacent cavities, referred as intercavity nonlinear interactions of polaritons. Thus, the intercavity nonlinear interaction between polariton is another novel property due to the combination of photon and molecule characters. Intercavity nonlinear interaction of polariton is desirable because it can enable interplay between independent cavities,

critical for propagating information on ultrafast time scale, and mimicking anharmonic interaction terms in quantum simulations, e.g. Hubbard-Mott Hamiltonian.[290, 291]

8.2 Methods

8.2.1 Fabrication of Dual Cavity Optical Mirror

In order to generate two cavity modes with certain frequency difference, two different path lengths need to be achieved within one pair of cavity mirror. A checkerboard pattern is designed and fabricated on CaF_2 window using photolithography, followed by sputtering deposition of a layer of ZnO and life-off of ZnO deposited on photoresist, thus leaving behind a layer of checkerboard patterned ZnO on CaF_2. Dielectric coatings are deposited to both flat CaF_2 window and CaF_2 window with patterned ZnO layer to obtain $\approx 96\%$ reflectivity at around 5um wavelength. In this work, a dielectric coated flat CaF_2 and a dielectric coated CaF_2 with patterned ZnO (≈ 300nm) are used in pair to generate dual cavity modes separated by ≈ 30 cm^{-1} at 5um. The frequency separation between the dual cavity modes can be tuned by varying the thickness of ZnO layer.

8.2.2 Sample Preparation

The $W(CO)_6$ (Sigma-Aldrich) /dual-cavity system is prepared in an IR spectral cell (Harrick) containing one flat dielectric CaF_2 mirror and one checkerboard patterned dielectric CaF_2 mirror described as above, separated by a 12.5 μm Teflon spacer and filled with $W(CO)_6$/hexane solution. The regular $W(CO)_6$ /cavity system is prepared in the same way in an IR spectral cell with two flat dielectric CaF_2 mirrors.

8.2.3 2D IR Spectrometer for Microcavity Systems

Two-dimensional infrared (2D IR) spectroscopy is applied to investigate the light-matter interaction of a $W(CO)_6$/microcavity system as described in Section 3.1. Briefly, a pump-probe geometry is adopted where three IR pulses interact with sample systems. The first IR pump pulse and probe pulse generate two coherent states in the system in t_1 and t_3, respectively, which will later be Fourier transformed to frequency domain as w1 (pump frequency) and w3 (probe frequency). The second IR pump pulse put the system in a population state during t_2. All 2D IR spectra in this work is taken at t_2 = 40ps to avoid interference between pump and probe pulses. One special requirement for this experiment is that the rotation axis of the stage needs to be parallel to the incidence plane formed by the pump and probe beams. In this way, we ensure that the in-plane wavevectors, k∥, of pump and probe pulses are the same (Figure 8.1). The particular k∥ value the of pump and probe beams are determined by checking the 1D transmission polariton spectra of the pump and probe pulses before and after 2D IR acquisitions.
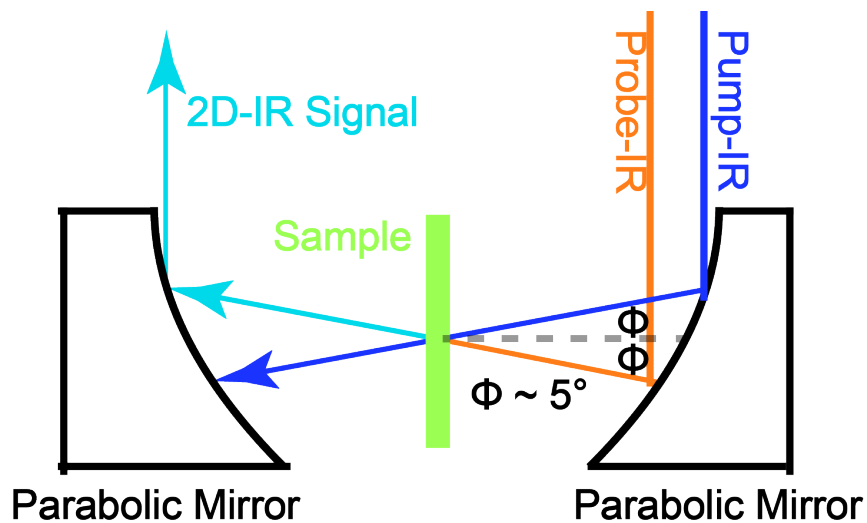
Figure 8.1: Illustration of configuration of IR pulses and sample cell in a microcavity system.

8.3 Results and Discussion

Molecular modes are a source of optical nonlinearity, but it is microscopic and local. On the other hand, photon cavity modes can be macroscopic and delocalized, but photons are lack of nonlinearity. The key idea for achieving delocalized optical nonlinearity, what we refer as intercavity polariton nonlinear interactions is to combine molecular nonlinearity with delocalized cavity modes. For example, a cavity would interact laterally to the neighboring cavities through delocalized evanescent wave. As a result, the molecular modes in the overlapping volumes between cavities can enable nonlinear interactions between polaritons in these cavity sites.

The design of experiment and FP cavity matrices is shown in Figure 8.2a and b: a checkerboard matrix is composed by individual square shape FP cavities, where cavities with two thickness alternates between each other. Therefore, cavities with two distinct transition frequency are aligned next to each other. The key idea for achieving intercavity polariton nonlinear interactions is: Through evanescent wave a cavity could couple laterally to the neighboring cavities, and therefore a shared molecular anharmonicity would enable nonlinear interactions between cavity sites. We used photolithography and lift-off methods to fabricate the checkerboard cavity matrix and an example SEM image of the cavity mirror is shown in Figure 8.2b, to show the shape and boundary of squares that define individual FP cavities. From experiments, we found the optimized cavity lateral dimension is 50 microns, which ensures a strong enough coupling between neighboring cavities, but not too strong to make the neighbor cavities indistinguishable. From linear IR transmission spectrum, two sharp cavity transitions can be identified at 1970 and 2000 cm^{-1} (bottom, Figure 8.2b), agreeing with expected cavity resonance separation.

We prepared the polariton systems by encapsulating a 40 mM $W(CO)_6$ in hexane solution in the coupled-cavity matrix. $W(CO)_6$ has a strong asymmetric stretch vibrational mode at 1983 cm^{-1}, and therefore is ideal for forming polaritons in the IR regime. From a naive perspective, if the molecular vibrational modes couple to the two cavity modes simultaneously, we would
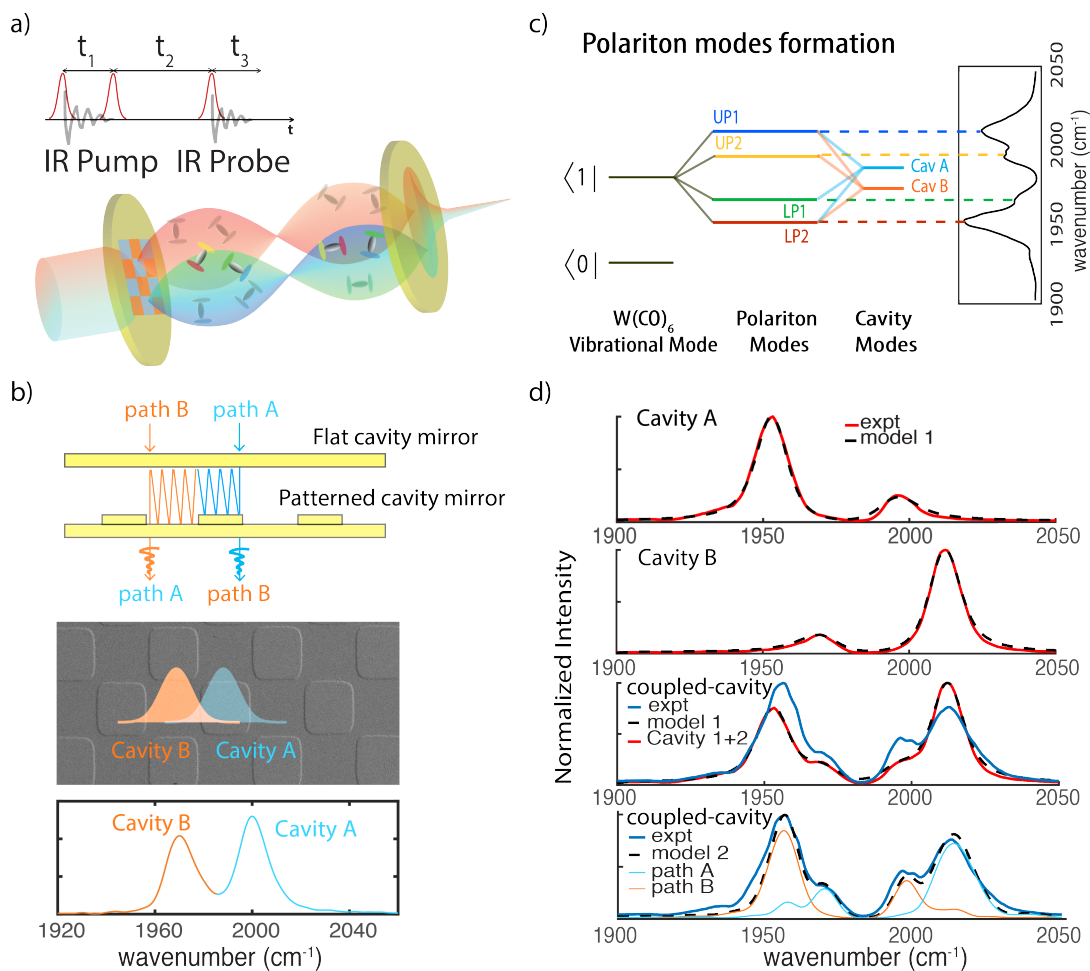
Figure 8.2: a) Cartoon of dual cavity and 2D IR pulse sequence. b) Two proposed paths of photons in a dual cavity c) Energy diagram of polariton modes formed by coupling of $W(CO)_6$ and dual cavity. d) Experimental and simulated linear IR of polaritons.

expect a system composed by three polaritons, and therefore three IR peaks. However, the linear IR spectrum of the coupled-cavity polariton shows a surprising four-peak feature (blue trace in Figure 8.2d). It seems to indicate that the molecular vibration couples to the two cavities separately, each forming two pairs of polaritons to compose the total four peaks. For example, the polariton of checkerboard cavity matrix can be view as a sum of two pairs of polaritons from two cavities at different detunings, e.g. UP1 and LP1 are from cavity A, and UP2 and LP2 are from cavity B. To test this idea, we use regular FP cavities to prepare two polariton systems separately,

with one matching the corresponding Rabi splitting and detuning of UP1 and LP1, and the other one matching UP2 and LP2 peaks (top two panels in Figure 8.2d). Then, we simply add the two spectra together, and compare the summed spectrum with the spectrum of the coupled-cavity polaritons. While the polariton positions match well with the coupled-cavity polaritons, the intensities do not (third panel in Figure 8.2d). Thus, it indicates that the coupling scenario of the coupled-cavity polaritons is neither molecular vibrations couple to two cavities simultaneously and equally, nor couples to them separately. We note the widely-used semiclassical model can reproduce the position and intensities of polariton peaks of these regular cavities very well (model 1 [292] (Eq. 8.1), dashed line in top two panels Figure 8.2d).

$$T_{model1}(\nu) = \frac{T^2 e^{-\alpha L}}{1 + R^2 e^{-2\alpha L} - 2Re^{-\alpha L}\cos(4\pi nL\nu + 2\varphi)} \tag{8.1}$$

where, T_{model1} describes the polaritons in a Fabry-Perot cavity, α and n is the frequency dependent absorption coefficient and refractive index of the material within the cavity, reflectivity, whereas T, R, L, and φ is the transmission, reflectivity, thickness, and phase shift of the cavity.

However, the existing semiclassical model (model 1) would only reproduce the polariton peak positions, but not the peak intensity of coupled-cavity polaritons, and a new model that can take into account the subtle coupling between cavities is necessary. This new model (model 2 in Figure 8.2d) shows that it is necessary to include a photon hopping process to describe the delocalization of cavity modes between sites, which couple cavities together. The essence of the new model is described in upper panel of Figure 8.2b: Upon entering cavity A, after a few round trips, photons can hop to cavity B, subsequently alter the mode and interact with molecular vibrations in cavity B (Path A). An alternative path (Path B) also should exist. In this model, the semi-classical description of cavity polariton evolve into Eq. 8.2

$$T_{model2} = [\frac{T_1 e^{(-\frac{1}{2}\alpha L_1)}}{1 - R_1 e^{i\Delta\varphi_1 - \alpha L_1}}(1 - R_1^n e^{-n\alpha L_1 + in\Delta\varphi_1}) + \frac{\sqrt{T_1 T_2} e^{-\frac{1}{2}\alpha L_1}}{1 - R_2 e^{i\Delta\varphi_2 - \alpha L_2}}$$

$$(R_1^{n-1} e^{-(n-1)\alpha L_1 + i(n-1)\Delta\varphi_1} R_2 e^{-\alpha L_2 + i\Delta\varphi_2})]^2 \qquad (8.2)$$

where, T_n, R_n, L_n, and φ_n are transmission, reflectivity, cavity thickness, and phase shift of cavity n, respectively, whereas α is the absorptive coefficient of molecules, and n represents the number of round trips before photon hopping to the adjacent cavity. Using model 2, we can reproduce the experimental measurements much better than the model 1 (bottom panel of Figure 8.2d). We find the measured linear IR spectra are in fact a combination of two sets of cavity polaritons: one set having photon entering cavity A first and then hop to cavity B (Path A), whereas the other one has the reversed entrance and exit (Path B) (Figure 8.2d). We notice, because of photon hopping, under model 2, in each cavity polariton set, there are three polariton peaks, instead of two (bottom panel of Figure 8.2d). The agreement between the simulated results of model 2 and experimental linear IR spectra suggest that it is important to include cavity mode delocalization in the semiclassical model to proper account the degrees of coupling between the adjacent cavities.

Next, we examine nonlinear interactions of the coupled-cavity matrix, by conducting 2D IR spectroscopy on the coupled-cavity polariton system. 2D IR measures the third order nonlinear response function of the systems of interests. The pulse sequence described in Figure 8.2a excites two vibrational coherences at various time incidences, and therefore can track the interaction and dynamics of vibrational quantum states of the systems. For example, when two modes are coupled to each other, e.g. through mechanical or electrostatic coupling, or sharing the same ground states, cross peaks appear at the corner defined by the resonance frequency of the two coupled modes. Thus, it is an ideal way to probe nonlinear interaction between polaritons in adjacent cavities.
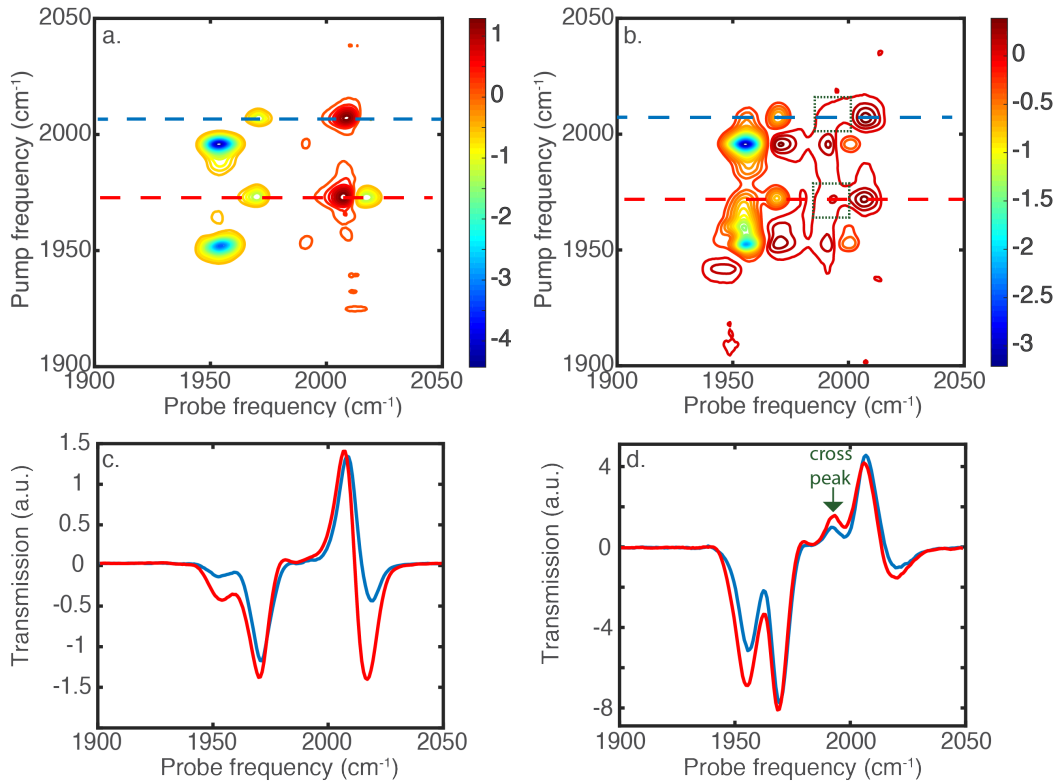
Figure 8.3: a) 2D IR of W(CO)$_6$/hexane in two uncoupled cavities (regular cavity A+B). b) 2D IR of W(CO)$_6$/hexane in coupled dual cavity. c) Pump spectral cuts of 2D IR in a) at UP1 and LP1. d) Pump spectral cuts of 2D IR in b) at UP1 and LP1 show cross peak features.

2D IR spectra of the coupled-cavity polariton systems show clear cross peaks (taken at t$_2$ = 40 ps, labeled in dotted green squares in Figure 8.3b and by arrows in Figure 8.3d), indicating that polaritons in adjacent cavities interact with each other. For example, the peak at 2010, and 1995 cm^{-1} is generated by pumping at UP1, and subsequently perturbing the polariton transition at UP2. To ensure the observed cross peaks are not because of other processes, we also performed 2D IR measurements of the two detuned regular FP cavities separately, and added their spectra together to simulate polaritons in two uncoupled cavities (Figure 8.3a and c). We find no cross peaks in this scenario, indicating lack of intercavity polariton nonlinear interactions.

To further extract quantitative insights, we take spectral cut of the 2D spectra at specific ω_1, which corresponds to pump probe spectra by pumping at specific quantum state at ω_1, and simulate the spectral cuts using model 2. In our and others' pervious publications,[292, 293] we

have revealed the origin of nonlinear signal of polariton system: the derivative signal near UP is due to Rabi splitting contractions, whereas the strong absorptive feature is originated from the overtone absorption of the dark modes in the cavity. Similar approach can be taken here, but using the modified semi-classical model 2 with photon hopping. To simulate the spectral cuts, aside from simulating the regular linear spectra, which equals to spectra with no IR pump, we also simulate another spectrum with a certain ground state population lifted to the excited vibrational states, to mimic the effect of an IR excitation. Then we take the difference of the two spectra to simulate pump probe spectra, equivalent to a 2D IR spectral cut at specific ω_1. The simulated spectra match with the experimental results reasonably well, capturing the derivative features on the UP side as well as double absorptive features in the LP side (Figure 8.4a is spectral cut at ω_1=1970 cm^{-1}, simulation of other spectral cuts are in Supplemental Materials). There are two peaks (at 1995 and 1955 cm^{-1} respectively) in the spectral cuts that could be the signatures of nonlinear interaction. However, as indicated from simulation, a signal from 2→3 transition of the dark modes can significantly contribute to the 1955 cm^{-1} peak, and therefore, only 1995 cm^{-1} peak is purely originated from nonlinear interactions between cavity polaritons (labeled by green arrow in Figure 8.3d).

The simulated 2D spectral cut can be decomposed into contributions from cavity A and B paths, to further learn the origin of the nonlinear interaction. It shows that the cross peak at 1995 cm^{-1} is mainly due polaritons of cavity B path (purple trace in Figure 8.4a), indicating a significant contribution to the nonlinear interaction coming from creating nonequilibrium molecular populations that interact with cavity B. However, because the spectral cut is a result of pumping the LP1 peak of cavity A, this result reflects that while LP1 is excited, a portion of these excited molecular population of LP1 resides in the overlapping volume between cavity A and B, and this shared excited molecular states generates a nonlinear response of polaritons in cavity B.

Further analysis indicates that both cavity delocalization and molecular nonlinearity are the key ingredients in generating intercavity nonlinear interactions between polaritons. To see

this, we turn off either of cavity delocalization or molecular nonlinearity (Figure 8.4b). When delocalization (hopping) is turned off, a spectrum similar to single cavity polaritons is created, and when molecular nonlinearity is off by setting anharmonicity to be zero, there is simply know nonlinear signals, because 2D IR measures only nonlinear optical responses. Only when both cavity delocalization and molecular nonlinearity co-exists, the experimental spectral signatures are well reproduced.

Lastly, we investigate how the intercavity polariton nonlinear interaction can be manipulated by molecular concentration and thereby Rabi splitting. It is found that the cross peak becomes stronger as concentration (coupling strength or Rabi splitting) is increased (Figure 8.4c), which indicates stronger nonequilibrium population in polariton of Path B is created, when transitions of polariton from Path A is excited. In other words, as Rabi splitting becomes larger, there are more shared molecular anharmonicity. In other words, as Rabi splitting becomes larger, more molecules are shared between cavity A and B. This trend is supported by a simply coupled oscillator model, in which each cavity strongly couples to the vibrational modes in its own volume, and weakly couples to the vibrational modes from adjacent cavity, through evanescent wave or photon hopping. When molecular concentration is increased, the coupling strength is enhanced, making the polariton modes contains more wavefunctions from molecular vibrations of the adjacent cavity and therefore more shared molecular anharmonicity. Therefore, controlling Rabi splitting would be critical for engineering intercavity polariton nonlinear interactions.

8.4   Conclusions

The demonstrated intercavity nonlinear interaction between polaritons is exclusively a result of joint merits of delocalization of cavity modes, e.g. photon hopping, and molecular nonlinearity. By combining the advantages of cavity and molecular modes, a unique new property is created which does not exist in neither mode by themselves, demonstrating that
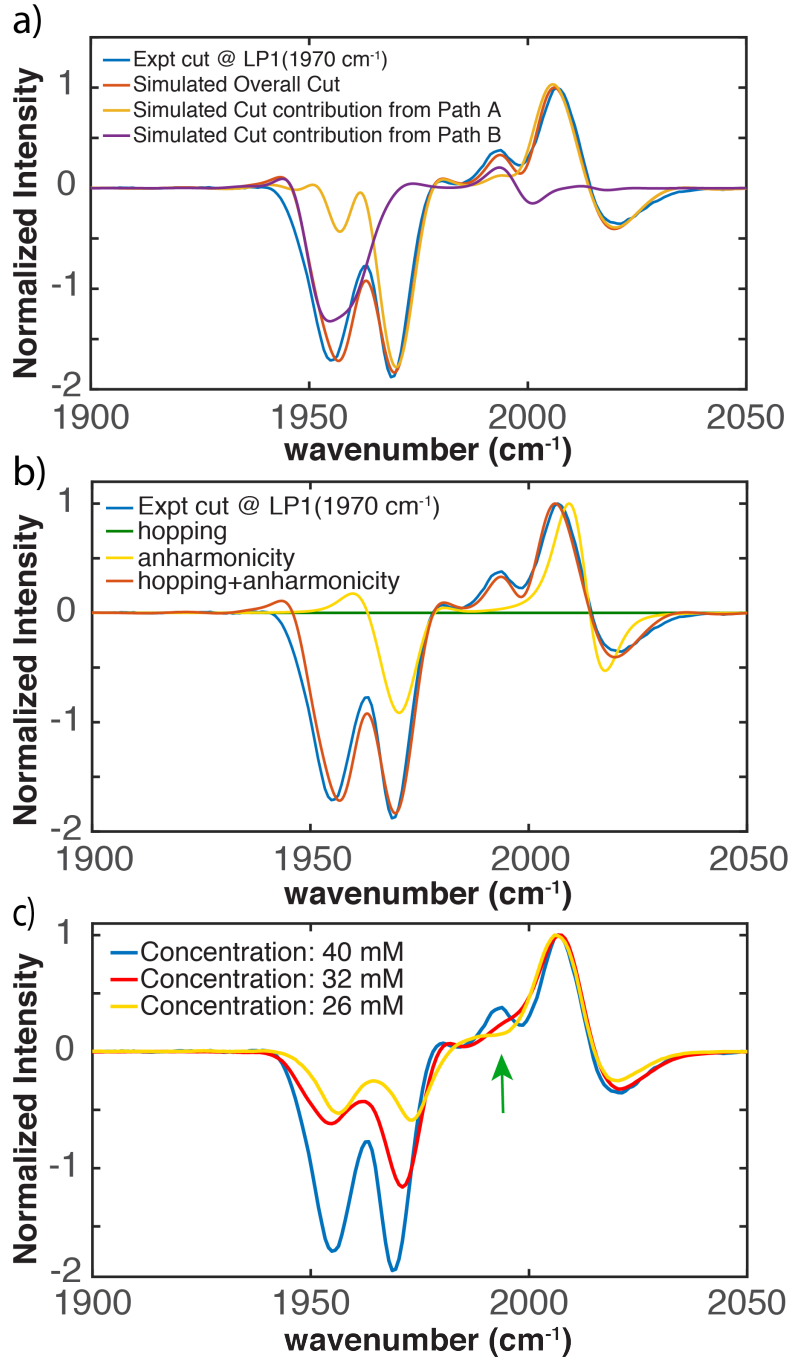
Figure 8.4: a) Experimental (blue) and simulated (red) spectral cut at LP1. b) Simulated cut spectrum with hopping (green), anharmonicity (yellow), hopping and anharmonicity (red). c) Experimental spectral cuts at LP1 of different $W(CO)_6$ concentrations (coupling strengths).

polariton can processes "the best of both worlds". More sophisticated photonic structures beyond this simple checkerboard coupled-cavity matrix can be designed to enhance the intercavity

nonlinear interaction. This demonstration adds spatial dimension into the parameter space for manipulating polariton nonlinear interactions. Using this initial demonstration as a foundation, further developments in demonstrating sophisticated operations, e.g. phase control, and nonlinear interaction over a longer distance, will push IR polariton into exciting applications, e.g. IR based chemical sensing, photonic circuitry and quantum information on a "2D chip".

Chapter 8, in full, is currently being prepared for submission for publication of the material. Jiaxi Wang; Bo Xiang; Wei Xiong. The dissertation author was the primary investigator and author of this paper.

Chapter 9

Conclusions and Outlook

2D IR spectroscopy for samples in solution is an established method in time-resolved spectroscopy. After almost two decades of technological development, 2D IR is capable of routinely resolving, for instance, ultrafast conformational changes,[30, 136, 175] structural diversity of biomolecules,[34, 294] drugbinding to enzymes.[295] Despite 2D IR has been used successfully for studying ultrafast conformation exchanges of organometallic compounds, our works have shown for the first time a kinetically stabled unsaturated compound being investigated, and the first observation of an ultrafast dynamic equilibrium involving two distinct structural isomers and the intermediate connecting them. Surprisingly, these relatively large transition metal complex undergoes isomerization at rates comparable to the rotational isomerization reactions of small organic molecules, irrespective to the presence of bulky ligands at outer spheres. We have also used 2D IR to observed the intercavity polariton-polariton ultrafast nonlinear interaction for the first time, which is essential in realizing optical switches, quantum communication and information.

Furthermore, we demonstrate that the surface specific version of 2D IR — 2D SFG is a powful tool for studying the structural orientation and dynamics for samples at surfaces and interfaces. We show that the orientation heterogeneity of molecules at interfaces can be

determined using HD 2D VSFG. In particular, we studied the monolayer of Re(4,4'-dicyano-2,2'-bipyridine)(CO)$_3$Cl on a gold electrode and found that it forms a fairly ordered structure, which has implications to the surface structure-function relationships, and porposed a new method will contribute significantly in determining the molecular conformations at interfaces. We have also shown by simulating the 2D lineshape that the different homogeneous broadening experienced by different vibraional modes is due to the substrate-absorbate interaction through image dipole on gold surface, which is highly sensitive to the relative distance of the vibrational modes to the surface.

To conclude, the range of future applications for ultrafast 2D vibrational spectroscopy is very broad and the possible impact of the methods can hardly be overrated. In particular, 2D vibrational spectroscopy at surfaces has opened up a completely new way of measuring ultrafast dynamics and spectral correlations in highly interesting and relevant samples since the initial reports about 10 years ago.[98, 102, 140] Among the most interested examples are related to vibrational dynamics in catalysis — photocatalysis and electrocatalysis,[63, 296–300] including potential applications regarding, e.g. water splitting,[66, 300–303] CO$_2$ reduction,[304–306] or wastewater treatment.[297, 307, 308] Surface sensitive 2D vibrational spectroscopy has great potential applicaiton in help establishing a correlation of the sample performance with in situ structural and dynamic information, which is key to gain a fundamental understanding of the systems and the underlying catalytic mechanisms.

Bibliography

[1] Kraack, J. P.; Hamm, P. Surface-Sensitive and Surface-Specific Ultrafast Two-Dimensional Vibrational Spectroscopy. *Chemical Reviews* **2017**, *117*, 10623–10664.

[2] Kuhs, C. T.; Luther, B. M.; Krummel, A. T. Recent Advances in 2D IR Spectroscopy Driven by Advances in Ultrafast Technology. *IEEE Journal of Selected Topics in Quantum Electronics* **2019**, *25*, 1–13.

[3] Khalil, M.; Demirdöven, N.; Tokmakoff, A. Coherent 2D IR Spectroscopy: Molecular Structure and Dynamics in Solution. *The Journal of Physical Chemistry A* **2003**, *107*, 5258–5279.

[4] Mukamel, S. Multidimensional Femtosecond Correlation Spectroscopies of Electronic and Vibrational Excitations. *Annual Review of Physical Chemistry* **2000**, *51*, 691–729.

[5] Jonas, D. M. Two-Dimensional Femtosecond Spectroscopy. *Annual Review of Physical Chemistry* **2003**, *54*, 425–463.

[6] Ernst, R. R.; Bodenhausen, G.; Wokaun, A. *Principles of nuclear magnetic resonance in one and two dimensions*; 1987.

[7] Aue, W. P.; Bartholdi, E.; Ernst, R. R. Two-dimensional spectroscopy. Application to nuclear magnetic resonance. *The Journal of Chemical Physics* **1976**, *64*, 2229–2246.

[8] Woutersen, S.; Hamm, P. Nonlinear two-dimensional vibrational spectroscopy of peptides. **2002**, *14*, R1035–R1062.

[9] Mukamel, S.; Piryatinski, A.; Chernyak, V. Two-Dimensional Raman Echoes: Femtosecond View of Molecular Structure and Vibrational Coherence. *Accounts of Chemical Research* **1999**, *32*, 145–154.

[10] CHO, M. *Advances in Multi-Photon Processes and Spectroscopy*; WORLD SCIENTIFIC, 1999; Vol. Volume 12; pp 229–300.

[11] Fourkas, J. T. HIGHER-ORDER OPTICAL CORRELATION SPECTROSCOPY IN LIQUIDS. *Annual Review of Physical Chemistry* **2002**, *53*, 17–40.

[12] Tominaga, K.; Maekawa, H. Investigation of Two-Dimensional Vibrational Spectrum by a Diagrammatic Approach. *Bulletin of the Chemical Society of Japan* **2001**, *74*, 279–286.

[13] Underwood, D. F.; Blank, D. A. Ultrafast Solvation Dynamics: A View from the Solvent's Perspective Using a Novel Resonant-Pump, Nonresonant-Probe Technique. *The Journal of Physical Chemistry A* **2003**, *107*, 956–961.

[14] Tanimura, Y.; Mukamel, S. Two-dimensional femtosecond vibrational spectroscopy of liquids. *The Journal of Chemical Physics* **1993**, *99*, 9496–9511.

[15] Kubarych, K. J.; Milne, C. J.; Lin, S.; Astinov, V.; Miller, R. J. D. Diffractive optics-based six-wave mixing: Heterodyne detection of the full χ(5) tensor of liquid CS_2. *The Journal of Chemical Physics* **2002**, *116*, 2016–2042.

[16] Zhao, W.; Wright, J. C. Spectral Simplification in Vibrational Spectroscopy Using Doubly Vibrationally Enhanced Infrared Four Wave Mixing. *Journal of the American Chemical Society* **1999**, *121*, 10994–10998.

[17] Zhao, W.; Wright, J. C. Doubly Vibrationally Enhanced Four Wave Mixing: The Optical Analog to 2D NMR. *Physical Review Letters* **2000**, *84*, 1411–1414.

[18] Deàk, J. C.; Rhea, S. T.; Iwaki, L. K.; Dlott, D. D. Vibrational Energy Relaxation and Spectral Diffusion in Water and Deuterated Water. *The Journal of Physical Chemistry A* **2000**, *104*, 4866–4875.

[19] Dlott, D. D. Vibrational energy redistribution in polyatomic liquids: 3D infrared–Raman spectroscopy. *Chemical Physics* **2001**, *266*, 149–166.

[20] Fayer, M. D. Dynamics of Liquids, Molecules, and Proteins Measured with Ultrafast 2D IR Vibrational Echo Chemical Exchange Spectroscopy. *Annual Review of Physical Chemistry* **2009**, *60*, 21–38.

[21] Cho, M. Coherent Two-Dimensional Optical Spectroscopy. *Chemical Reviews* **2008**, *108*, 1331–1418.

[22] Hamm, P.; Zanni, M. *Concepts and methods of 2D infrared spectroscopy*; Cambridge University Press, 2011.

[23] Hamm, P.; Lim, M.; Hochstrasser, R. M. Structure of the Amide I Band of Peptides Measured by Femtosecond Nonlinear-Infrared Spectroscopy. *The Journal of Physical Chemistry B* **1998**, *102*, 6123–6138.

[24] Naraharisetty, S. R. G.; Kasyanenko, V. M.; Rubtsov, I. V. Bond connectivity measured via relaxation-assisted two-dimensional infrared spectroscopy. *The Journal of Chemical Physics* **2008**, *128*, 104502.

[25] Rubtsov, I. V. Relaxation-Assisted Two-Dimensional Infrared (RA 2DIR) Method: Accessing Distances over 10 Åand Measuring Bond Connectivity Patterns. *Accounts of Chemical Research* **2009**, *42*, 1385–1394.

[26] Zheng, J.; Fayer, M. D. Solute-Solvent Complex Kinetics and Thermodynamics Probed by 2D-IR Vibrational Echo Chemical Exchange Spectroscopy. *The Journal of Physical Chemistry B* **2008**, *112*, 10221–10227.

[27] Zheng, J.; Kwak, K.; Asbury, J.; Chen, X.; Piletic, I. R.; Fayer, M. D. Ultrafast Dynamics of Solute-Solvent Complexation Observed at Thermal Equilibrium in Real Time. *Science* **2005**, *309*, 1338–1343.

[28] Kim, Y. S.; Hochstrasser, R. M. Chemical exchange 2D IR of hydrogen-bond making and breaking. *Proceedings of the National Academy of Sciences of the United States of America* **2005**, *102*, 11185.

[29] Zheng, J.; Fayer, M. D. Hydrogen Bond Lifetimes and Energetics for Solute/Solvent Complexes Studied with 2D-IR Vibrational Echo Spectroscopy. *Journal of the American Chemical Society* **2007**, *129*, 4328–4335.

[30] Zheng, J.; Kwak, K.; Chen, X.; Asbury, J. B.; Fayer, M. D. Formation and Dissociation of Intra-Intermolecular Hydrogen-Bonded Solute-Solvent Complexes: Chemical Exchange Two-Dimensional Infrared Vibrational Echo Spectroscopy. *Journal of the American Chemical Society* **2006**, *128*, 2977–2987.

[31] Asbury, J. B.; Steinel, T.; Stromberg, C.; Gaffney, K. J.; Piletic, I. R.; Goun, A.; Fayer, M. D. Hydrogen Bond Dynamics Probed with Ultrafast Infrared Heterodyne-Detected Multidimensional Vibrational Stimulated Echoes. *Physical Review Letters* **2003**, *91*, 237402–.

[32] Kwak, K.; Zheng, J.; Cang, H.; Fayer, M. D. Ultrafast Two-Dimensional Infrared Vibrational Echo Chemical Exchange Experiments and Theory. *The Journal of Physical Chemistry B* **2006**, *110*, 19998–20013.

[33] Zheng, J.; Kwak, K.; Xie, J.; Fayer, M. D. Ultrafast Carbon-Carbon Single-Bond Rotational Isomerization in Room-Temperature Solution. *Science* **2006**, *313*, 1951–1955.

[34] Asplund, M. C.; Zanni, M. T.; Hochstrasser, R. M. Two-dimensional infrared spectroscopy of peptides by phase-controlled femtosecond vibrational photon echoes. *Proceedings of the National Academy of Sciences* **2000**, *97*, 8219.

[35] Ishikawa, H.; Kwak, K.; Chung, J. K.; Kim, S.; Fayer, M. D. Direct observation of fast protein conformational switching. *Proceedings of the National Academy of Sciences* **2008**, *105*, 8619.

[36] Maekawa, H.; Toniolo, C.; Moretto, A.; Broxterman, Q. B.; Ge, N.-H. Different Spectral Signatures of Octapeptide 310- and α-Helices Revealed by Two-Dimensional Infrared Spectroscopy. *The Journal of Physical Chemistry B* **2006**, *110*, 5834–5837.

[37] Mukherjee, P.; Kass, I.; Arkin, I. T.; Zanni, M. T. Picosecond dynamics of a membrane protein revealed by 2D IR. *Proceedings of the National Academy of Sciences of the United States of America* **2006**, *103*, 3528.

[38] Hunt, N. T. 2D-IR spectroscopy: ultrafast insights into biomolecule structure and function. *Chemical Society Reviews* **2009**, *38*, 1837–1848.

[39] Zaera, F. Probing Liquid/Solid Interfaces at the Molecular Level. *Chemical Reviews* **2012**, *112*, 2920–2986.

[40] Madey, T. E.; Yates Jr, J. T. *Vibrational spectroscopy of molecules on surfaces*; Springer Science & Business Media, 2013; Vol. 1.

[41] Ibach, H. *Physics of surfaces and interfaces*; Springer, 2006; Vol. 12.

[42] Whitesides, G. M.; Laibinis, P. E. Wet chemical approaches to the characterization of organic surfaces: self-assembled monolayers, wetting, and the physical-organic chemistry of the solid-liquid interface. *Langmuir* **1990**, *6*, 87–96.

[43] Whitesides, G. M.; Ostuni, E.; Takayama, S.; Jiang, X.; Ingber, D. E. Soft Lithography in Biology and Biochemistry. *Annual Review of Biomedical Engineering* **2001**, *3*, 335–373.

[44] Somorjai, G. A.; Li, Y. Impact of surface chemistry. *Proceedings of the National Academy of Sciences* **2011**, *108*, 917.

[45] Somorjai, G. A. Modern Surface Science and Surface Technologies: An Introduction. *Chemical Reviews* **1996**, *96*, 1223–1236.

[46] Castner, D. G.; Somorjai, G. A. Surface structures of adsorbed gases on solid surfaces. A tabulation of data reported by low-energy electron diffraction studies. *Chemical Reviews* **1979**, *79*, 233–252.

[47] Yates, J. T. Surface chemistry at metallic step defect sites. *Journal of Vacuum Science & Technology A* **1995**, *13*, 1359–1367.

[48] Hiemenz, P. C.; Rajagopalan, R. *Principles of Colloid and Surface Chemistry, revised and expanded*; CRC press, 2016.

[49] King, D. A. *The chemical physics of solid surfaces and heterogeneous catalysis*; Elsevier, 2012; Vol. 5.

[50] Ertl, G. Reactions at Surfaces: From Atoms to Complexity (Nobel Lecture). *Angewandte Chemie International Edition* **2008**, *47*, 3524–3535.

[51] Zambelli, T.; Wintterlin, J.; Trost, J.; Ertl, G. Identification of the ¨Active Sites¨ of a Surface-Catalyzed Reaction. *Science* **1996**, *273*, 1688.

[52] Hess, C.; Funk, S.; Bonn, M.; Denzler, D. N.; Wolf, M.; Ertl, G. Femtosecond dynamics of chemical reactions at surfaces. *Applied Physics A* **2000**, *71*, 477–483.

[53] Kolasinski, K. W. *Surface science: foundations of catalysis and nanoscience*; John Wiley & Sons, 2012.

[54] Adamson, A. W.; Gast, A. P. *Physical chemistry of surfaces*; Interscience New York, 1967; Vol. 15.

[55] Somorjai, G. A.; Li, Y. *Introduction to surface chemistry and catalysis*; John Wiley & Sons, 2010.

[56] Zaera, F. Surface chemistry at the liquid/solid interface. *Surface Science* **2011**, *605*, 1141–1145.

[57] Love, J. C.; Estroff, L. A.; Kriebel, J. K.; Nuzzo, R. G.; Whitesides, G. M. Self-Assembled Monolayers of Thiolates on Metals as a Form of Nanotechnology. *Chemical Reviews* **2005**, *105*, 1103–1170.

[58] Ulman, A. Formation and Structure of Self-Assembled Monolayers. *Chemical Reviews* **1996**, *96*, 1533–1554.

[59] Ulman, A. *An Introduction to Ultrathin Organic Films: From Langmuir–Blodgett to Self–Assembly*; Academic press, 2013.

[60] Barth, J. V.; Costantini, G.; Kern, K. Engineering atomic and molecular nanostructures at surfaces. *Nature* **2005**, *437*, 671–679.

[61] Chechik, V.; Crooks, R. M.; Stirling, C. J. M. Reactions and Reactivity in Self-Assembled Monolayers. *Advanced Materials* **2000**, *12*, 1161–1171.

[62] Badia, A.; Lennox, R. B.; Reven, L. A Dynamic View of Self-Assembled Monolayers. *Accounts of Chemical Research* **2000**, *33*, 475–481.

[63] Fox, M. A.; Dulay, M. T. Heterogeneous photocatalysis. *Chemical Reviews* **1993**, *93*, 341–357.

[64] Somorjai, G. A.; Contreras, A. M.; Montano, M.; Rioux, R. M. Clusters, surfaces, and catalysis. *Proceedings of the National Academy of Sciences* **2006**, *103*, 10577.

[65] Bailey, D. C.; Langer, S. H. Immobilized transition-metal carbonyls and related catalysts. *Chemical Reviews* **1981**, *81*, 109–148.

[66] Maeda, K.; Domen, K. Photocatalytic Water Splitting: Recent Progress and Future Challenges. *The Journal of Physical Chemistry Letters* **2010**, *1*, 2655–2661.

[67] Schneider, J.; Matsuoka, M.; Takeuchi, M.; Zhang, J.; Horiuchi, Y.; Anpo, M.; Bahnemann, D. W. Understanding TiO2 Photocatalysis: Mechanisms and Materials. *Chemical Reviews* **2014**, *114*, 9919–9986.

[68] Bahnemann, D. Photocatalytic water treatment: solar energy applications. *Solar Energy* **2004**, *77*, 445–459.

[69] Kamat, P. V. Photophysical, Photochemical and Photocatalytic Aspects of Metal Nanoparticles. *The Journal of Physical Chemistry B* **2002**, *106*, 7729–7744.

[70] Pichat, P. Representative examples of infrared spectroscopy uses in semiconductor photocatalysis. *Catalysis Today* **2014**, *224*, 251–257.

[71] Auwärter, W.; Écija, D.; Klappenberger, F.; Barth, J. V. Porphyrins at interfaces. *Nature Chemistry* **2015**, *7*, 105 EP –.

[72] Mette, G.; Sutter, D.; Gurdal, Y.; Schnidrig, S.; Probst, B.; Iannuzzi, M.; Hutter, J.; Alberto, R.; Osterwalder, J. From porphyrins to pyrphyrins: adsorption study and metalation of a molecular catalyst on Au(111). *Nanoscale* **2016**, *8*, 7958–7968.

[73] Nguyen, S. C.; Lomont, J. P.; Caplins, B. W.; Harris, C. B. Studying the Dynamics of Photochemical Reactions via Ultrafast Time-Resolved Infrared Spectroscopy of the Local Solvent. *The Journal of Physical Chemistry Letters* **2014**, *5*, 2974–2978.

[74] Wang, J.; Clark, M. L.; Li, Y.; Kaslan, C. L.; Kubiak, C. P.; Xiong, W. Short-Range Catalyst–Surface Interactions Revealed by Heterodyne Two-Dimensional Sum Frequency Generation Spectroscopy. *The Journal of Physical Chemistry Letters* **2015**, *6*, 4204–4209.

[75] Arnolds, H. Vibrational dynamics of adsorbates-Quo vadis? *Progress in Surface Science* **2011**, *86*, 1–40.

[76] Heilweil, E. J.; Casassa, M. P.; Cavanagh, R. R.; Stephenson, J. C. Picosecond Vibrational Energy Transfer Studies of Surface Adsorbates. *Annual Review of Physical Chemistry* **1989**, *40*, 143–171.

[77] Gruebele, M.; Wolynes, P. G. Vibrational Energy Flow and Chemical Reactions. *Accounts of Chemical Research* **2004**, *37*, 261–267.

[78] Park, J. Y.; Baker, L. R.; Somorjai, G. A. Role of Hot Electrons and Metal–Oxide Interfaces in Surface Chemistry and Catalytic Reactions. *Chemical Reviews* **2015**, *115*, 2781–2817.

[79] Anthony, J. E. Functionalized Acenes and Heteroacenes for Organic Electronics. *Chemical Reviews* **2006**, *106*, 5028–5048.

[80] Bendikov, M.; Wudl, F.; Perepichka, D. F. Tetrathiafulvalenes, Oligoacenenes, and Their Buckminsterfullerene Derivatives: The Brick and Mortar of Organic Electronics. *Chemical Reviews* **2004**, *104*, 4891–4946.

[81] Zahn, D. R. T.; Gavrila, G. N.; Salvan, G. Electronic and Vibrational Spectroscopies Applied to Organic/Inorganic Interfaces. *Chemical Reviews* **2007**, *107*, 1161–1232.

[82] Bakulin, A. A.; Lovrincic, R.; Yu, X.; Selig, O.; Bakker, H. J.; Rezus, Y. L. A.; Nayak, P. K.; Fonari, A.; Coropceanu, V.; Brédas, J.-L.; Cahen, D. Mode-selective vibrational modulation of charge transport in organic electronic devices. *Nature Communications* **2015**, *6*, 7880 EP –.

[83] Wang, K.-X.; Li, X.-H.; Chen, J.-S. Surface and Interface Engineering of Electrode Materials for Lithium-Ion Batteries. *Advanced Materials* **2015**, *27*, 527–545.

[84] Armand, M.; Endres, F.; MacFarlane, D. R.; Ohno, H.; Scrosati, B. Ionic-liquid materials for the electrochemical challenges of the future. *Nature Materials* **2009**, *8*, 621 EP –.

[85] Palacín, M. R. Recent advances in rechargeable battery materials: a chemist's perspective. *Chemical Society Reviews* **2009**, *38*, 2565–2575.

[86] Boyd, R. W. *Nonlinear Optics (Third Edition)*; Academic Press: Burlington, 2008.

[87] Anfuso, C. L.; Xiao, D.; Ricks, A. M.; Negre, C. F. A.; Batista, V. S.; Lian, T. Orientation of a Series of CO_2 Reduction Catalysts on Single Crystal TiO2 Probed by Phase-Sensitive Vibrational Sum Frequency Generation Spectroscopy (PS-VSFG). *The Journal of Physical Chemistry C* **2012**, *116*, 24107–24114.

[88] Baldelli, S.; Mailhot, G.; Ross, P.; Shen, Y.-R.; Somorjai, G. A. Potential Dependent Orientation of Acetonitrile on Platinum (111) Electrode Surface Studied by Sum Frequency Generation. *The Journal of Physical Chemistry B* **2001**, *105*, 654–662.

[89] Shen, Y. R. Surface properties probed by second-harmonic and sum-frequency generation. *Nature* **1989**, *337*, 519–525.

[90] Nihonyanagi, S.; Yamaguchi, S.; Tahara, T. Direct evidence for orientational flip-flop of water molecules at charged interfaces: A heterodyne-detected vibrational sum frequency generation study. *The Journal of Chemical Physics* **2009**, *130*, 204704.

[91] Nihonyanagi, S.; Mondal, J. A.; Yamaguchi, S.; Tahara, T. Structure and Dynamics of Interfacial Water Studied by Heterodyne-Detected Vibrational Sum-Frequency Generation. *Annual Review of Physical Chemistry* **2013**, *64*, 579–603.

[92] Shen, Y. R.; Ostroverkhov, V. Sum-Frequency Vibrational Spectroscopy on Water Interfaces: Polar Orientation of Water Molecules at Interfaces. *Chemical Reviews* **2006**, *106*, 1140–1154.

[93] Zhuang, X.; Miranda, P. B.; Kim, D.; Shen, Y. R. Mapping molecular orientation and conformation at interfaces by surface nonlinear optics. *Physical Review B* **1999**, *59*, 12632–12640.

[94] Ghosh, A.; Ho, J.-J.; Serrano, A. L.; Skoff, D. R.; Zhang, T.; Zanni, M. T. Two-dimensional sum-frequency generation (2D SFG) spectroscopy: summary of principles and its application to amyloid fiber monolayers. *Faraday Discussions* **2015**, *177*, 493–505.

[95] Superfine, R.; Huang, J. Y.; Shen, Y. R. Phase measurement for surface infrared-visible sum-frequency generation. *Optics Letters* **1990**, *15*, 1276–1278.

[96] Laaser, J. E.; Skoff, D. R.; Ho, J.-J.; Joo, Y.; Serrano, A. L.; Steinkruger, J. D.; Gopalan, P.; Gellman, S. H.; Zanni, M. T. Two-Dimensional Sum-Frequency Generation Reveals Structure and Dynamics of a Surface-Bound Peptide. *Journal of the American Chemical Society* **2014**, *136*, 956–962.

[97] Laaser, J. E.; Xiong, W.; Zanni, M. T. Time-Domain SFG Spectroscopy Using Mid-IR Pulse Shaping: Practical and Intrinsic Advantages. *The Journal of Physical Chemistry B* **2011**, *115*, 2536–2546.

[98] Xiong, W.; Laaser, J. E.; Mehlenbacher, R. D.; Zanni, M. T. Adding a dimension to the infrared spectra of interfaces using heterodyne detected 2D sum-frequency generation (HD 2D SFG) spectroscopy. *Proceedings of the National Academy of Sciences* **2011**, *108*, 20902.

[99] Zhang, Z.; Piatkowski, L.; Bakker, H. J.; Bonn, M. Ultrafast vibrational energy transfer at the water/air interface revealed by two-dimensional surface vibrational spectroscopy. *Nature Chemistry* **2011**, *3*, 888 EP –.

[100] Bredenbeck, J.; Ghosh, A.; Nienhuys, H.-K.; Bonn, M. Interface-Specific Ultrafast Two-Dimensional Vibrational Spectroscopy. *Accounts of Chemical Research* **2009**, *42*, 1332–1342.

[101] Zhang, Z.; Piatkowski, L.; Bakker, H. J.; Bonn, M. Communication: Interfacial water structure revealed by ultrafast two-dimensional surface vibrational spectroscopy. *The Journal of Chemical Physics* **2011**, *135*, 021101.

[102] Bredenbeck, J.; Ghosh, A.; Smits, M.; Bonn, M. Ultrafast Two Dimensional-Infrared Spectroscopy of a Molecular Monolayer. *Journal of the American Chemical Society* **2008**, *130*, 2152–2153.

[103] Ghosh, A.; Smits, M.; Sovago, M.; Bredenbeck, J.; Müller, M.; Bonn, M. Ultrafast vibrational dynamics of interfacial water. *Chemical Physics* **2008**, *350*, 23–30.

[104] Ho, J.-J.; Skoff, D. R.; Ghosh, A.; Zanni, M. T. Structural Characterization of Single-Stranded DNA Monolayers Using Two-Dimensional Sum Frequency Generation Spectroscopy. *The Journal of Physical Chemistry B* **2015**, *119*, 10586–10596.

[105] Li, Z.; Wang, J.; Li, Y.; Xiong, W. Solving the "Magic Angle" Challenge in Determining Molecular Orientation Heterogeneity at Interfaces. *The Journal of Physical Chemistry C* **2016**, *120*, 20239–20246.

[106] Li, Y.; Wang, J.; Clark, M. L.; Kubiak, C. P.; Xiong, W. Characterizing interstate vibrational coherent dynamics of surface adsorbed catalysts by fourth-order 3D SFG spectroscopy. *Chemical Physics Letters* **2016**, *650*, 1–6.

[107] Ulness, D. J.; Albrecht, A. C. Theory of time-resolved coherent Raman scattering with spectrally tailored noisy light. *Journal of Raman Spectroscopy* **1997**, *28*, 571–578.

[108] Kirkwood, J. C.; Ulness, D. J.; Albrecht, On the Classification of the Electric Field Spectroscopies: Application to Raman Scattering. *The Journal of Physical Chemistry A* **2000**, *104*, 4167–4173.

[109] Loring, R. F.; Mukamel, S. Selectivity in coherent transient Raman measurements of vibrational dephasing in liquids. *The Journal of Chemical Physics* **1985**, *83*, 2116–2128.

[110] Kramer, P. L.; Nishida, J.; Giammanco, C. H.; Tamimi, A.; Fayer, M. D. Observation and theory of reorientation-induced spectral diffusion in polarization-selective 2D IR spectroscopy. *The Journal of Chemical Physics* **2015**, *142*, 184505.

[111] Demirdöven, N.; Khalil, M.; Tokmakoff, A. Correlated Vibrational Dynamics Revealed by Two-Dimensional Infrared Spectroscopy. *Physical Review Letters* **2002**, *89*, 237401–.

[112] Kwak, K.; Park, S.; Finkelstein, I. J.; Fayer, M. D. Frequency-frequency correlation functions and apodization in two-dimensional infrared vibrational echo spectroscopy: A new approach. *The Journal of Chemical Physics* **2007**, *127*, 124503.

[113] Roberts, S. T.; Loparo, J. J.; Tokmakoff, A. Characterization of spectral diffusion from two-dimensional line shapes. *The Journal of Chemical Physics* **2006**, *125*, 084502.

[114] Guo, Q.; Pagano, P.; Li, Y.-L.; Kohen, A.; Cheatum, C. M. Line shape analysis of two-dimensional infrared spectra. *The Journal of Chemical Physics* **2015**, *142*, 212427.

[115] Fenn, E. E.; Fayer, M. D. Extracting 2D IR frequency-frequency correlation functions from two component systems. *The Journal of Chemical Physics* **2011**, *135*, 074502.

[116] Shim, S.-H.; Strasfeld, D. B.; Fulmer, E. C.; Zanni, M. T. Femtosecond pulse shaping directly in the mid-IR using acousto-optic modulation. *Opt. Lett.* **2006**, *31*, 838–840.

[117] Shim, S.-H.; Zanni, M. T. How to turn your pump–probe instrument into a multidimensional spectrometer: 2D IR and Vis spectroscopiesvia pulse shaping. *Physical Chemistry Chemical Physics* **2009**, *11*, 748–761.

[118] Nee, M. J.; McCanne, R.; Kubarych, K. J.; Joffre, M. Two-dimensional infrared spectroscopy detected by chirped pulse upconversion. *Optics Letters* **2007**, *32*, 713–715.

[119] Rock, W.; Li, Y.-L.; Pagano, P.; Cheatum, C. M. 2D IR Spectroscopy using Four-Wave Mixing, Pulse Shaping, and IR Upconversion: A Quantitative Comparison. *The Journal of Physical Chemistry A* **2013**, *117*, 6073–6083.

[120] HOMMEL, E. L.; ALLEN, H. C. Broadband Sum Frequency Generation with Two Regenerative Amplifiers: Temporal Overlap of Femtosecond and Picosecond Light Pulses. *Analytical Sciences* **2001**, *17*, 137–139.

[121] Stiopkin, I. V.; Jayathilake, H. D.; Bordenyuk, A. N.; Benderskii, A. V. Heterodyne-Detected Vibrational Sum Frequency Generation Spectroscopy. *Journal of the American Chemical Society* **2008**, *130*, 2271–2275.

[122] Grevels, F.-W.; Jacke, J.; Klotzbücher, W. E.; Krüger, C.; Seevogel, K.; Tsay, Y.-H. Dynamic Processes on the IR Time Scale: Coalescence of CO Stretching Vibrational Bands in [(η4-Diene)Fe(CO)3] Complexes. *Angewandte Chemie International Edition in English* **1987**, *26*, 885–887.

[123] Ito, T.; Hamaguchi, T.; Nagino, H.; Yamaguchi, T.; Washington, J.; Kubiak, C. P. Effects of Rapid Intramolecular Electron Transfer on Vibrational Spectra. *Science* **1997**, *277*, 660–663.

[124] Grevels, F.-W.; Kerpen, K.; Klotzbücher, W. E.; McClung, R. E. D.; Russell, G.; Viotte, M.; Schaffner, K. *Journal of the American Chemical Society* **1998**, *120*, 10423–10433.

[125] Cohen, B.; Weiss, S. IR lines broadened by chemical exchange. *The Journal of Chemical Physics* **1980**, *72*, 6804–6804.

[126] Cohen, B.; Weiss, S. Reply to a comment by Weston on "IR lines broadened by chemical exchange". *The Journal of Chemical Physics* **1981**, *74*, 3635–3635.

[127] Cohen, B.; Weiss, S. Solvent effects on the i.r. spectrum of acetylacetone and of 1,2-dichloroethane. *Spectrochimica Acta Part A: Molecular Spectroscopy* **1988**, *44*, 529 – 531.

[128] Johnston, V. J.; Einstein, F. W. B.; Pomeroy, R. K. The new binary carbonyl tetraosmium tetradecacarbonyl: an example of carbonyl exchange on the infrared time scale. *Organometallics* **1988**, *7*, 1867–1869.

[129] Balch, A. L.; Miller, J. 1,2-Dithiolene complexes of ruthenium and iron. *Inorganic Chemistry* **1971**, *10*, 1410–1415.

[130] Bernal, I.; Clearfield, A.; Epstein, E. F.; Ricci, J. S.; Balch, A.; Miller, J. S. Isomeric conformations in a pentaco-ordinated ruthenium compound; crystal and molecular structures of the orange and violet isomers of (Ph3P)2[(CF3)2C2S2]Ru(CO). *Journal of the Chemical Society, Chemical Communications* **1973**, 39–40.

[131] Hoffman, P. R.; Caulton, K. G. Solution structure and dynamics of five-coordinate d6 complexes. *Journal of the American Chemical Society* **1975**, *97*, 4221–4228.

[132] Zheng, J.; Kwak, K.; Fayer, M. D. Ultrafast 2D IR Vibrational Echo Spectroscopy. *Accounts of Chemical Research* **2007**, *40*, 75–83.

[133] Anna, J. M.; Ross, M. R.; Kubarych, K. J. Dissecting Enthalpic and Entropic Barriers to Ultrafast Equilibrium Isomerization of a Flexible Molecule Using 2DIR Chemical Exchange Spectroscopy. *The Journal of Physical Chemistry A* **2009**, *113*, 6544–6547.

[134] Nilsen, I. A.; Osborne, D. G.; White, A. M.; Anna, J. M.; Kubarych, K. J. Monitoring equilibrium reaction dynamics of a nearly barrierless molecular rotor using ultrafast vibrational echoes. *The Journal of Chemical Physics* **2014**, *141*, 134313.

[135] Eckert, P. A.; Kubarych, K. J. Dynamic Flexibility of Hydrogenase Active Site Models Studied with 2D-IR Spectroscopy. *The Journal of Physical Chemistry A* **2017**, *121*, 608–615.

[136] Cahoon, J. F.; Sawyer, K. R.; Schlegel, J. P.; Harris, C. B. Determining Transition-State Geometries in Liquids Using 2D-IR. *Science* **2008**, *319*, 1820.

[137] Roberts, S. T.; Ramasesha, K.; Tokmakoff, A. Structural Rearrangements in Water Viewed Through Two-Dimensional Infrared Spectroscopy. *Accounts of Chemical Research* **2009**, *42*, 1239–1249.

[138] Anna, J. M.; Kubarych, K. J. Watching solvent friction impede ultrafast barrier crossings: A direct test of Kramers theory. *The Journal of Chemical Physics* **2010**, *133*, 174506.

[139] Lee, K.-K.; Park, K.-H.; Joo, C.; Kwon, H.-J.; Han, H.; Ha, J.-H.; Park, S.; Cho, M. Ultrafast internal rotational dynamics of the azido group in (4S)-azidoproline: Chemical exchange 2DIR spectroscopic investigations. *Chemical Physics* **2012**, *396*, 23–29.

[140] Rosenfeld, D. E.; Gengeliczki, Z.; Smith, B. J.; Stack, T. D. P.; Fayer, M. D. Structural Dynamics of a Catalytic Monolayer Probed by Ultrafast 2D IR Vibrational Echoes. *Science* **2011**, *334*, 634.

[141] Rosenfeld, D. E.; Nishida, J.; Yan, C.; Kumar, S. K. K.; Tamimi, A.; Fayer, M. D. Structural Dynamics at Monolayer–Liquid Interfaces Probed by 2D IR Spectroscopy. *The Journal of Physical Chemistry C* **2013**, *117*, 1409–1420.

[142] Kiefer, L. M.; Kubarych, K. J. Solvent-Dependent Dynamics of a Series of Rhenium Photoactivated Catalysts Measured with Ultrafast 2DIR. *The Journal of Physical Chemistry A* **2015**, *119*, 959–965.

[143] King, J. T.; Anna, J. M.; Kubarych, K. J. Solvent-hindered intramolecular vibrational redistribution. *Physical Chemistry Chemical Physics* **2011**, *13*, 5579–5583.

[144] King, J. T.; Ross, M. R.; Kubarych, K. J. Water-Assisted Vibrational Relaxation of a Metal Carbonyl Complex Studied with Ultrafast 2D-IR. *The Journal of Physical Chemistry B* **2012**, *116*, 3754–3759.

[145] Fedoseeva, M.; Delor, M.; Parker, S. C.; Sazanovich, I. V.; Towrie, M.; Parker, A. W.; Weinstein, J. A. Vibrational energy transfer dynamics in ruthenium polypyridine transition metal complexes. *Physical Chemistry Chemical Physics* **2015**, *17*, 1688–1696.

[146] Krespan, C. G. Bis-(polyfluoroalkyl)-acetylenes. IV. Fluorinated Dithietenes and Related Heterocyclic Compounds From Bis-(polyfluoroalkyl)-acetylenes and Sulfur1. *Journal of the American Chemical Society* **1961**, *83*, 3434–3437.

[147] Neese, F. An improvement of the resolution of the identity approximation for the formation of the Coulomb matrix. *Journal of Computational Chemistry* **2003**, *24*, 1740–1747.

[148] Kossmann, S.; Neese, F. Comparison of two efficient approximate Hartee–Fock approaches. *Chemical Physics Letters* **2009**, *481*, 240–243.

[149] Neese, F.; Wennmohs, F.; Hansen, A.; Becker, U. Efficient approximate and parallel Hartree–Fock and hybrid DFT calculations. A 'chain-of-spheres'algorithm for the Hartree–Fock exchange. *Chemical Physics* **2009**, *356*, 98–109.

[150] Izsák, R.; Neese, F. An overlap fitted chain of spheres exchange method. *The Journal of Chemical Physics* **2011**, *135*, 144105.

[151] Neese, F. The ORCA program system. *Wiley Interdisciplinary Reviews: Computational Molecular Science* **2012**, *2*, 73–78.

[152] Huzinaga, S.; Andzelm, J.; Radzio-Andzelm, E.; Sakai, Y.; Tatewaki, H.; Klobukiwski, M. *Physical Sciences Data*; Elsevier, 1983; Vol. 16; p 434.

[153] Andrae, D.; Häußermann, U.; Dolg, M.; Stoll, H.; Preuß, H. Energy-adjustedab initio pseudopotentials for the second and third row transition elements. *Theoretica chimica acta* **1990**, *77*, 123–141.

[154] Schäfer, A.; Horn, H.; Ahlrichs, R. Fully optimized contracted Gaussian basis sets for atoms Li to Kr. *The Journal of Chemical Physics* **1992**, *97*, 2571–2577.

[155] Schäfer, A.; Huber, C.; Ahlrichs, R. Fully optimized contracted Gaussian basis sets of triple zeta valence quality for atoms Li to Kr. *The Journal of Chemical Physics* **1994**, *100*, 5829–5835.

[156] Weigend, F. Accurate Coulomb-fitting basis sets for H to Rn. *Physical Chemistry Chemical Physics* **2006**, *8*, 1057–1065.

[157] Pantazis, D. A.; Neese, F. All-electron scalar relativistic basis sets for the 6p elements. *Theoretical Chemistry Accounts* **2012**, *131*, 1292.

[158] Pantazis, D. A.; Neese, F. All-Electron Scalar Relativistic Basis Sets for the Actinides. *Journal of Chemical Theory and Computation* **2011**, *7*, 677–684.

[159] Pantazis, D. A.; Neese, F. All-Electron Scalar Relativistic Basis Sets for the Lanthanides. *Journal of Chemical Theory and Computation* **2009**, *5*, 2229–2238.

[160] Pantazis, D. A.; Chen, X.-Y.; Landis, C. R.; Neese, F. All-Electron Scalar Relativistic Basis Sets for Third-Row Transition Metal Atoms. *Journal of Chemical Theory and Computation* **2008**, *4*, 908–919.

[161] Sinnecker, S.; Rajendran, A.; Klamt, A.; Diedenhofen, M.; Neese, F. Calculation of Solvent Shifts on Electronic g-Tensors with the Conductor-Like Screening Model (COSMO) and Its Self-Consistent Generalization to Real Solvents (Direct COSMO-RS). *The Journal of Physical Chemistry A* **2006**, *110*, 2235–2245.

[162] Grimme, S.; Ehrlich, S.; Goerigk, L. Effect of the damping function in dispersion corrected density functional theory. *Journal of Computational Chemistry* **2011**, *32*, 1456–1465.

[163] Grimme, S.; Antony, J.; Ehrlich, S.; Krieg, H. A consistent and accurate ab initio parametrization of density functional dispersion correction (DFT-D) for the 94 elements H-Pu. *The Journal of Chemical Physics* **2010**, *132*, 154104.

[164] Pettersen, E. F.; Goddard, T. D.; Huang, C. C.; Couch, G. S.; Greenblatt, D. M.; Meng, E. C.; Ferrin, T. E. UCSF Chimera—A visualization system for exploratory research and analysis. *Journal of Computational Chemistry* **2004**, *25*, 1605–1612.

[165] Urbanek, D. C.; Vorobyev, D. Y.; Serrano, A. L.; Gai, F.; Hochstrasser, R. M. The Two-Dimensional Vibrational Echo of a Nitrile Probe of the Villin HP35 Protein. *The Journal of Physical Chemistry Letters* **2010**, *1*, 3311–3315.

[166] Muetterties, E. L.; Schunn, R. A. Pentaco-ordination. *Quarterly Reviews, Chemical Society* **1966**, *20*, 245–299.

[167] Couzijn, E. P. A.; Slootweg, J. C.; Ehlers, A. W.; Lammertsma, K. Stereomutation of Pentavalent Compounds: Validating the Berry Pseudorotation, Redressing Ugi's Turnstile Rotation, and Revealing the Two- and Three-Arm Turnstiles. *Journal of the American Chemical Society* **2010**, *132*, 18127–18140.

[168] Giordano, A. N.; Lear, B. J. Solvent versus Temperature Control over the Infrared Band Shape and Position in Fe(CO)3(η4-Ligand) Complexes. *The Journal of Physical Chemistry A* **2013**, *117*, 12313–12319.

[169] Giordano, A. N.; Lear, B. J. Comparing the Energetic and Dynamic Contributions of Solvent to Very Low Barrier Isomerization Using Dynamic Steady-State Vibrational Spectroscopy. *The Journal of Physical Chemistry A* **2015**, *119*, 3545–3555.

[170] Hill, A. D.; Zoerb, M. C.; Nguyen, S. C.; Lomont, J. P.; Bowring, M. A.; Harris, C. B. Determining Equilibrium Fluctuations Using Temperature-Dependent 2D-IR. *The Journal of Physical Chemistry B* **2013**, *117*, 15346–15355.

[171] Berry, R. S. Correlation of Rates of Intramolecular Tunneling Processes, with Application to Some Group V Compounds. *The Journal of Chemical Physics* **1960**, *32*, 933–938.

[172] Bernal, I.; Clearfield, A.; Ricci, J. S. Crystal structure of the orange isomer of [(C6H5)3P]2[C2S2(CF3)2]RuCO. *Journal of Crystal and Molecular Structure* **1974**, *4*, 43–54.

[173] Clearfield, A.; Epstein, E. F.; Bernal, I. The crystal and molecule structure of the violet isomer of ($\emptyset$P)$_2$[(CF$_3$)$_2$C$_2$S$_2$]RuCO. *Journal of Coordination Chemistry* **1977**, *6*, 227–240.

[174] Cohen, B.; Weiss, S. Picosecond kinetics by exchange broadening in the infrared and Raman. 1. 1,2-Dichloroethane. *The Journal of Physical Chemistry* **1983**, *87*, 3606–3610.

[175] Porter, T. M.; Wang, J.; Li, Y.; Xiang, B.; Salsman, C.; Miller, J. S.; Xiong, W.; Kubiak, C. P. Direct observation of the intermediate in an ultrafast isomerization. *Chem. Sci.* **2019**, *10*, 113–117.

[176] Thompson, D. E.; Merchant, K. A.; Fayer, M. D. Two-dimensional ultrafast infrared vibrational echo studies of solute–solvent interactions and dynamics. *The Journal of Chemical Physics* **2001**, *115*, 317–330.

[177] Heck, R. *Organotransition Metal Chemistry A Mechanistic Approach*; Elsevier, 2012; p 350.

[178] Klingler, R. J.; Rathke, J. W. High-Pressure NMR Investigation of Hydrogen Atom Transfer and Related Dynamic Processes in Oxo Catalysis. **1994**, *116*, 4772–4785.

[179] Nalesnik, T. E.; Orchin, M. Free radical reactions of tetracarbonylhydridocobalt. **1982**, *1*, 222–223.

[180] Ungváry, F.; Markó, L. Reaction of $HCo(CO)_4$ with olefins. Effect of $Co_2(CO)_8$. **1981**, *219*, 397–400.

[181] Ungváry, F. Kinetics if the $Co_2(CO)_8$-dependent reactions of $HCo(CO)_4$ with olefins. **1982**, *111*, 117–130.

[182] Brunet, J. J.; Sidot, C.; Caubere, P. Activation of reducing agents. Sodium hydride containing complex reducing agents : XIV. NaCoCO4as an SRN1 nucleophile in the carbonylation of aryl halides by CoCRACO at atmospheric pressure. New preparation of NaCoCO4 by NaH reduction of dicobalt octacarbonyl. **1981**, *204*, 229–241.

[183] Wegman, R. W.; Brown, T. L. Photochemical and thermal decomposition of hydridotetracarbonylcobalt(I). Evidence for a radical pathway involving octacarbonyldicobalt. **1980**, *102*, 2494–2495.

[184] Roth, J. A.; Orchin, M. The stoichiometric hydrogenation of 1,1-diphenylethylene with hydridocobalt tetracarbonyl; differences from the hydroformylation reaction. **1979**, *182*, 299–311.

[185] Rathke, J. W.; Feder, H. M. Catalysis of carbon monoxide hydrogenation by soluble mononuclear complexes. **1978**, *100*, 3623–3625.

[186] Paulik, F. E. RECENT DEVELOPMENTS IN HYDROFORMYLATION CATALYSIS. **1972**, *6*, 49–84.

[187] Seyferth, D.; Millar, M. D. Reactions of dicobalt octacarbonyl and related compounds with gem-dihalides. **1972**, *38*, 373–383.

[188] Susuki, T.; Tsuji, J. Organic syntheses by means of metal complexes. I. Carbonylation of olefins with carbon monoxide and carbon tetrachloride catalyzed by binuclear metal carbonyls. **1968**, *9*, 913–915.

[189] Crichton, O.; Poliakoff, M.; Rest, A. J.; Turner, J. J. Infrared spectral evidence for the formation of the new complexes dicarbonyldinitrosylosmium and tetracarbonylcobalt in frozen gas matrices at 20 K. **1973**, *0*, 1321–1324.

[190] Wawersik, H.; Keller, H. J. [Zeitschrift fr Naturforschung B] Spektroskopische Untersuchungen an Komplexverbindungen II EPR-Spektren des monomeren Kobalttetracarbonyls. **1965**, 938–942.

[191] Huo, C.-F.; Li, Y.-W.; Wu, G.-S.; Beller, M.; Jiao, H. Structures and Energies of [Co(CO)n]m(m= 0, 1+, 1-) and HCo(CO)n: Density Functional Studies. **2002**, *106*, 12161–12169.

[192] Ozin, G. A.; Vander Voet, A. Transition metal atom inorganic synthesis in matrixes. **2002**, *6*, 313–318.

[193] Hoffmann, R.; Elian, M. Bonding Capabilities of Transition Metal Carbonyl Fragments. **2001**, 1–19.

[194] Sweany, Photolysis of Matrix-Isolated Hydridotetracarbonylcobalt(1). Evidence for Metal-Hydrogen Bond Homolysis. **1980**, 1–5.

[195] Hanlan, L. A.; Huber, H.; Kuendig, E. P.; McGarvey, B. R.; Ozin, Chemical synthesis using metal atoms. Matrix infrared, Raman, ultraviolet-visible, and electron spin resonance studies of the binary carbonyls of cobalt, Co(CO)n (where n = 1-4), and the distortion problem in tetracarbonylcobalt. **1975**, *97*, 7054–7068.

[196] Margulieux, G. W.; Weidemann, N.; Lacy, D. C.; Moore, C. E.; Rheingold, A. L.; Figueroa, J. S. Isocyano Analogues of [Co(CO)4]n: A Tetraisocyanide of Cobalt Isolated in Three States of Charge. **2010**, *132*, 5033–5035.

[197] Chan, C.; Carpenter, A. E.; Gembicky, M.; Moore, C. E.; Rheingold, A. L.; Figueroa, J. S. Associative Ligand Exchange and Substrate Activation Reactions by a Zero-Valent Cobalt Tetraisocyanide Complex. **2018**, *38*, 1436–1444.

[198] Fox, B. J.; Millard, M. D.; DiPasquale, A. G.; Rheingold, A. L.; Figueroa, J. S. Thallium(I) as a Coordination Site Protection Agent: Preparation of an Isolable Zero-Valent Nickel Tris-Isocyanide. **2009**, *48*, 3473–3477.

[199] Labios, L. A.; Millard, M. D.; Rheingold, A. L.; Figueroa, J. S. Bond Activation, Substrate Addition and Catalysis by an Isolable Two-Coordinate Pd(0) Bis-Isocyanide Monomer. **2009**, *131*, 11318–11319.

[200] Ditri, T. B.; Fox, B. J.; Moore, C. E.; Rheingold, A. L.; Figueroa, J. S. Effective Control of Ligation and Geometric Isomerism: Direct Comparison of Steric Properties Associated with Bis-mesityl and Bis-diisopropylphenyl m-Terphenyl Isocyanides. **2009**, *48*, 8362–8375.

[201] Emerich, B. M.; Moore, C. E.; Fox, B. J.; Rheingold, A. L.; Figueroa, J. S. Protecting-Group-Free Access to a Three-Coordinate Nickel(0) Tris-isocyanide. **2011**, *30*, 2598–2608.

[202] Mokhtarzadeh, C. C.; Margulieux, G. W.; Carpenter, A. E.; Weidemann, N.; Moore, C. E.; Rheingold, A. L.; Figueroa, J. S. Synthesis and Protonation of an Encumbered Iron Tetraisocyanide Dianion. **2015**, *54*, 5579–5587.

[203] Carpenter, A. E.; Rheingold, A. L.; Figueroa, J. S. A Well-Defined Isocyano Analogue of HCo(CO)4. 1: Synthesis, Decomposition, and Catalytic 1,1-Hydrogenation of Isocyanides. **2016**, *35*, 2309–2318.

[204] Carpenter, A. E.; Chan, C.; Rheingold, A. L.; Figueroa, J. S. A Well-Defined Isocyano Analogue of HCo(CO)4. 2: Relative Brønsted Acidity as a Function of Isocyanide Ligation. **2016**, *35*, 2319–2326.

[205] Armarego, W. L. *Purification of laboratory chemicals*; Butterworth-Heinemann, 2017.

[206] Pangborn, A. B.; Giardello, M. A.; Grubbs, R. H.; Rosen, R. K.; Timmers, F. J. Safe and Convenient Procedure for Solvent Purification. *Organometallics* **1996**, *15*, 1518–1520.

[207] Agnew, D. W.; DiMucci, I. M.; Arroyave, A.; Gembicky, M.; Moore, C. E.; MacMillan, S. N.; Rheingold, A. L.; Lancaster, K. M.; Figueroa, J. S. Crystalline Coordination Networks of Zero-Valent Metal Centers: Formation of a 3-Dimensional Ni(0) Framework with m-Terphenyl Diisocyanides. *Journal of the American Chemical Society* **2017**, *139*, 17257–17260.

[208] Frisch, M. J. et al. Gaussian 16 Rev. C.01. 2016.

[209] Kumar, B.; Llorente, M.; Froehlich, J.; Dang, T.; Sathrum, A.; Kubiak, C. P. Photochemical and Photoelectrochemical Reduction of CO2. *Annual Review of Physical Chemistry* **2012**, *63*, 541–569.

[210] Galperin, M.; Nitzan, A. Molecular optoelectronics: the interaction of molecular conduction junctions with light. *Physical Chemistry Chemical Physics* **2012**, *14*, 9421–9438.

[211] Millan, K. M.; Mikkelsen, S. R. Sequence-selective biosensor for DNA based on electroactive hybridization indicators. *Analytical Chemistry* **1993**, *65*, 2317–2323.

[212] Benson, E. E.; Kubiak, C. P.; Sathrum, A. J.; Smieja, J. M. Electrocatalytic and homogeneous approaches to conversion of CO2 to liquid fuels. *Chemical Society Reviews* **2009**, *38*, 89–99.

[213] Smieja, J. M.; Benson, E. E.; Kumar, B.; Grice, K. A.; Seu, C. S.; Miller, A. J. M.; Mayer, J. M.; Kubiak, C. P. Kinetic and structural studies, origins of selectivity, and interfacial charge transfer in the artificial photosynthesis of CO. *Proceedings of the National Academy of Sciences* **2012**, *109*, 15646.

[214] Hovis, J. S.; Hamers, R. J. Structure and Bonding of Ordered Organic Monolayers of 1,3,5,7-Cyclooctatetraene on the Si(001) Surface: Surface Cycloaddition Chemistry of an Antiaromatic Molecule. *The Journal of Physical Chemistry B* **1998**, *102*, 687–692.

[215] Stöhr, J.; Outka, D. A. Determination of molecular orientations on surfaces from the angular dependence of near-edge x-ray-absorption fine-structure spectra. *Physical Review B* **1987**, *36*, 7891–7905.

[216] Castner, D. G.; Hinds, K.; Grainger, D. W. X-ray Photoelectron Spectroscopy Sulfur 2p Study of Organic Thiol and Disulfide Binding Interactions with Gold Surfaces. *Langmuir* **1996**, *12*, 5083–5086.

[217] Kiefer, L. M.; King, J. T.; Kubarych, K. J. Dynamics of Rhenium Photocatalysts Revealed through Ultrafast Multidimensional Spectroscopy. *Accounts of Chemical Research* **2015**, *48*, 1123–1130.

[218] Bredenbeck, J.; Helbing, J.; Hamm, P. Labeling Vibrations by Light: Ultrafast Transient 2D-IR Spectroscopy Tracks Vibrational Modes during Photoinduced Charge Transfer. *Journal of the American Chemical Society* **2004**, *126*, 990–991.

[219] Xiong, W.; Laaser, J. E.; Paoprasert, P.; Franking, R. A.; Hamers, R. J.; Gopalan, P.; Zanni, M. T. Transient 2D IR Spectroscopy of Charge Injection in Dye-Sensitized Nanocrystalline Thin Films. *Journal of the American Chemical Society* **2009**, *131*, 18040–18041.

[220] Ricks, A. M.; Anfuso, C. L.; Rodríguez-Córdoba, W.; Lian, T. Vibrational relaxation dynamics of catalysts on TiO2 Rutile (110) single crystal surfaces and anatase nanoporous thin films. *Chemical Physics* **2013**, *422*, 264–271.

[221] Clark, M. L.; Rudshteyn, B.; Ge, A.; Chabolla, S. A.; Machan, C. W.; Psciuk, B. T.; Song, J.; Canzi, G.; Lian, T.; Batista, V. S.; Kubiak, C. P. Orientation of Cyano-Substituted Bipyridine Re(I) fac-Tricarbonyl Electrocatalysts Bound to Conducting Au Surfaces. *The Journal of Physical Chemistry C* **2016**, *120*, 1657–1665.

[222] Nogues, C.; Wanunu, M. A rapid approach to reproducible, atomically flat gold films on mica. *Surface Science* **2004**, *573*, L383–L389.

[223] Ge, N.-H.; Zanni, M. T.; Hochstrasser, R. M. Effects of Vibrational Frequency Correlations on Two-Dimensional Infrared Spectra. *The Journal of Physical Chemistry A* **2002**, *106*, 962–972.

[224] Persson, B. N. J. Damping of excited molecules located above a metal surface. *Solid State Communications* **1978**, *27*, 417–421.

[225] Ueba, H. Vibrational lineshapes of adsorbates on solid surfaces. *Progress in Surface Science* **1986**, *22*, 181–321.

[226] Rosenfeld, D. E.; Nishida, J.; Yan, C.; Gengeliczki, Z.; Smith, B. J.; Fayer, M. D. Dynamics of Functionalized Surface Molecular Monolayers Studied with Ultrafast Infrared Vibrational Spectroscopy. *The Journal of Physical Chemistry C* **2012**, *116*, 23428–23440.

[227] Tully, J. C. Chemical Dynamics at Metal Surfaces. *Annual Review of Physical Chemistry* **2000**, *51*, 153–178.

[228] Roeterdink, W. G.; Berg, O.; Bonn, M. Frequency- and time-domain femtosecond vibrational sum frequency generation from CO adsorbed on Pt(111). *The Journal of Chemical Physics* **2004**, *121*, 10174–10180.

[229] Ueba, H. Vibrational relaxation and pump-probe spectroscopies of adsorbates on solid surfaces. *Progress in Surface Science* **1997**, *55*, 115–179.

[230] Matranga, C.; Guyot-Sionnest, P. Vibrational relaxation of cyanide at the metal/electrolyte interface. *The Journal of Chemical Physics* **2000**, *112*, 7615–7621.

[231] Persson, B. N. J.; Persson, M. Vibrational lifetime for CO adsorbed on Cu(100). *Solid State Communications* **1980**, *36*, 175–179.

[232] Persson, B. N. J.; Persson, M. Damping of vibrations in molecules adsorbed on a metal surface. *Surface Science* **1980**, *97*, 609–624.

[233] Persson, B. N. J.; Lang, N. D. Electron-hole-pair quenching of excited states near a metal. *Physical Review B* **1982**, *26*, 5409–5415.

[234] Persson, B. N. J.; Zaremba, E. Electron-hole pair production at metal surfaces. *Physical Review B* **1985**, *31*, 1863–1872.

[235] Persson, B. N. J.; Andersson, S. Dynamical processes at surfaces: Excitation of electron-hole pairs. *Physical Review B* **1984**, *29*, 4382–4394.

[236] Liebsch, A. Screening Properties of a Metal Surface at Low Frequencies and Finite Wave Vectors. *Physical Review Letters* **1985**, *54*, 67–70.

[237] Eguiluz, A. G. Electron-hole-pair damping of an excited state of a molecule absorbed on a metal surface. *Physical Review B* **1984**, *30*, 4366–4371.

[238] Ford, G. W.; Weber, W. H. Electromagnetic interactions of molecules with metal surfaces. *Physics Reports* **1984**, *113*, 195–287.

[239] Mukherjee, P.; Krummel, A. T.; Fulmer, E. C.; Kass, I.; Arkin, I. T.; Zanni, M. T. Site-specific vibrational dynamics of the CD3ζ membrane peptide using heterodyned two-dimensional infrared photon echo spectroscopy. *The Journal of Chemical Physics* **2004**, *120*, 10215–10224.

[240] Woys, A. M.; Lin, Y.-S.; Reddy, A. S.; Xiong, W.; de Pablo, J. J.; Skinner, J. L.; Zanni, M. T. 2D IR Line Shapes Probe Ovispirin Peptide Conformation and Depth in Lipid Bilayers. *Journal of the American Chemical Society* **2010**, *132*, 2832–2838.

[241] Ramasesha, K.; De Marco, L.; Mandal, A.; Tokmakoff, A. Water vibrations have strongly mixed intra- and intermolecular character. *Nature Chemistry* **2013**, *5*, 935 EP –.

[242] Petersen, P. B.; Tokmakoff, A. Source for ultrafast continuum infrared and terahertz radiation. *Optics Letters* **2010**, *35*, 1962–1964.

[243] Brandt, K.; Chiu, M. E.; Watson, D. J.; Tikhov, M. S.; Lambert, R. M. Chemoselective Catalytic Hydrogenation of Acrolein on Ag(111): Effect of Molecular Orientation on Reaction Selectivity. *Journal of the American Chemical Society* **2009**, *131*, 17286–17290.

[244] McMillan, D. G. G.; Marritt, S. J.; Kemp, G. L.; Gordon-Brown, P.; Butt, J. N.; Jeuken, L. J. C. The impact of enzyme orientation and electrode topology on the catalytic activity of adsorbed redox enzymes. *Electrochimica Acta* **2013**, *110*, 79–85.

[245] Barbey, R.; Lavanant, L.; Paripovic, D.; Schüwer, N.; Sugnaux, C.; Tugulu, S.; Klok, H.-A. Polymer Brushes via Surface-Initiated Controlled Radical Polymerization: Synthesis, Characterization, Properties, and Applications. *Chemical Reviews* **2009**, *109*, 5437–5527.

[246] Jailaubekov, A. E.; Willard, A. P.; Tritsch, J. R.; Chan, W.-L.; Sai, N.; Gearba, R.; Kaake, L. G.; Williams, K. J.; Leung, K.; Rossky, P. J.; Zhu, X.-Y. Hot charge-transfer excitons set the time limit for charge separation at donor/acceptor interfaces in organic photovoltaics. *Nature Materials* **2012**, *12*, 66 EP –.

[247] Wu, G.; Lee, K. Y. C. Effects of Poloxamer 188 on Phospholipid Monolayer Morphology: An Atomic Force Microscopy Study. *Langmuir* **2009**, *25*, 2133–2139.

[248] Lam, K. L. H.; Ishitsuka, Y.; Cheng, Y.; Chien, K.; Waring, A. J.; Lehrer, R. I.; Lee, K. Y. C. Mechanism of Supported Membrane Disruption by Antimicrobial Peptide Protegrin-1. *The Journal of Physical Chemistry B* **2006**, *110*, 21282–21286.

[249] Cracknell, J. A.; Vincent, K. A.; Armstrong, F. A. Enzymes as Working or Inspirational Electrocatalysts for Fuel Cells and Electrolysis. *Chemical Reviews* **2008**, *108*, 2439–2461.

[250] Eisenthal, K. B. Liquid Interfaces Probed by Second-Harmonic and Sum-Frequency Spectroscopy. *Chemical Reviews* **1996**, *96*, 1343–1360.

[251] Wang, H.-F.; Velarde, L.; Gan, W.; Fu, L. Quantitative Sum-Frequency Generation Vibrational Spectroscopy of Molecular Surfaces and Interfaces: Lineshape, Polarization, and Orientation. *Annual Review of Physical Chemistry* **2015**, *66*, 189–216.

[252] Yan, E. C. Y.; Wang, Z.; Fu, L. Proteins at Interfaces Probed by Chiral Vibrational Sum Frequency Generation Spectroscopy. *The Journal of Physical Chemistry B* **2015**, *119*, 2769–2785.

[253] Li, Z.; Weeraman, C. N.; Gibbs-Davis, J. M. Following the Azide-Alkyne Cycloaddition at the Silica/Solvent Interface with Sum Frequency Generation. *ChemPhysChem* **2014**, *15*, 2247–2251.

[254] Sohrabpour, Z.; Kearns, P. M.; Massari, A. M. Vibrational Sum Frequency Generation Spectroscopy of Fullerene at Dielectric Interfaces. *The Journal of Physical Chemistry C* **2016**, *120*, 1666–1672.

[255] Hopkins, A. J.; McFearin, C. L.; Richmond, G. L. Investigations of the solid–aqueous interface with vibrational sum-frequency spectroscopy. *Current Opinion in Solid State and Materials Science* **2005**, *9*, 19–27.

[256] Quast, A. D.; Curtis, A. D.; Horn, B. A.; Goates, S. R.; Patterson, J. E. Role of Nonresonant Sum-Frequency Generation in the Investigation of Model Liquid Chromatography Systems. *Analytical Chemistry* **2012**, *84*, 1862–1870.

[257] Wang, H.-F.; Gan, W.; Lu, R.; Rao, Y.; Wu, B.-H. Quantitative spectral and orientational analysis in surface sum frequency generation vibrational spectroscopy (SFG-VS). *International Reviews in Physical Chemistry* **2005**, *24*, 191–256.

[258] Roy, S.; Covert, P. A.; FitzGerald, W. R.; Hore, D. K. Biomolecular Structure at Solid–Liquid Interfaces As Revealed by Nonlinear Optical Spectroscopy. *Chemical Reviews* **2014**, *114*, 8388–8415.

[259] Li, Z.; Weeraman, C. N.; Azam, M. S.; Osman, E.; Gibbs-Davis, J. M. The thermal reorganization of DNA immobilized at the silica/buffer interface: a vibrational sum frequency generation investigation. *Physical Chemistry Chemical Physics* **2015**, *17*, 12452–12457.

[260] Simpson, G. J.; Westerbuhr, S. G.; Rowlen, K. L. Molecular Orientation and Angular Distribution Probed by Angle-Resolved Absorbance and Second Harmonic Generation. *Analytical Chemistry* **2000**, *72*, 887–898.

[261] Simpson, G. J.; Rowlen, K. L. An SHG Magic Angle: Dependence of Second Harmonic Generation Orientation Measurements on the Width of the Orientation Distribution. *Journal of the American Chemical Society* **1999**, *121*, 2635–2636.

[262] Li, Z.; Weeraman, C. N.; Gibbs-Davis, J. M. Ketone Binding at Amino and Ureido Monolayer/Solvent Interfaces Studied by Nonlinear Optical Techniques. *The Journal of Physical Chemistry C* **2014**, *118*, 28662–28670.

[263] Zhu, H.; Dhinojwala, A. Thermal Behavior of Long-Chain Alcohols on Sapphire Substrate. *Langmuir* **2015**, *31*, 6306–6313.

[264] Yamaguchi, S.; Hosoi, H.; Yamashita, M.; Sen, P.; Tahara, T. Physisorption Gives Narrower Orientational Distribution than Chemisorption on a Glass Surface: A Polarization-Sensitive Linear and Nonlinear Optical Study. *The Journal of Physical Chemistry Letters* **2010**, *1*, 2662–2665.

[265] Kundu, A.; Watanabe, H.; Yamaguchi, S.; Tahara, T. Agreement between Experimentally and Theoretically Estimated Orientational Distributions of Solutes at the Air/Water Interface. *The Journal of Physical Chemistry C* **2013**, *117*, 8887–8891.

[266] Bos, M. A.; Kleijn, J. M. Determination of the orientation distribution of adsorbed fluorophores using TIRF. I. Theory. *Biophysical Journal* **1995**, *68*, 2566–2572.

[267] Edmiston, P. L.; Lee, J. E.; Cheng, S.-S.; Saavedra, S. S. Molecular Orientation Distributions in Protein Films. 1. Cytochrome c Adsorbed to Substrates of Variable Surface Chemistry. *Journal of the American Chemical Society* **1997**, *119*, 560–570.

[268] Tronin, A.; Strzalka, J.; Chen, X.; Dutton, P. L.; Blasie, J. K. Determination of the Porphyrin Orientation Distribution in Langmuir Monolayers by Polarized Epifluorescence. *Langmuir* **2000**, *16*, 9878–9886.

[269] Runge, A. F.; Saavedra, S. S.; Mendes, S. B. Combination of Polarized TIRF and ATR Spectroscopies for Determination of the Second and Fourth Order Parameters of Molecular Orientation in Thin Films and Construction of an Orientation Distribution Based on the Maximum Entropy Method. *The Journal of Physical Chemistry B* **2006**, *110*, 6721–6731.

[270] Rao, Y.; Hong, S.-Y.; Turro, N. J.; Eisenthal, K. B. Molecular Orientational Distribution at Interfaces Using Second Harmonic Generation. *The Journal of Physical Chemistry C* **2011**, *115*, 11678–11683.

[271] Rao, Y.; Tao, Y.-s.; Wang, H.-f. Quantitative analysis of orientational order in the molecular monolayer by surface second harmonic generation. *The Journal of Chemical Physics* **2003**, *119*, 5226–5236.

[272] Yan, C.; Yuan, R.; Pfalzgraff, W. C.; Nishida, J.; Wang, L.; Markland, T. E.; Fayer, M. D. Unraveling the dynamics and structure of functionalized self-assembled monolayers on gold using 2D IR spectroscopy and MD simulations. *Proceedings of the National Academy of Sciences* **2016**, *113*, 4929.

[273] Anfuso, C. L.; Ricks, A. M.; Rodríguez-Córdoba, W.; Lian, T. Ultrafast Vibrational Relaxation Dynamics of a Rhenium Bipyridyl CO2–Reduction Catalyst at a Au Electrode Surface Probed by Time-Resolved Vibrational Sum Frequency Generation Spectroscopy. *The Journal of Physical Chemistry C* **2012**, *116*, 26377–26384.

[274] Inoue, K.-i.; Nihonyanagi, S.; Singh, P. C.; Yamaguchi, S.; Tahara, T. 2D heterodyne-detected sum frequency generation study on the ultrafast vibrational dynamics of H2O and HOD water at charged interfaces. *The Journal of Chemical Physics* **2015**, *142*, 212431.

[275] Singh, P. C.; Nihonyanagi, S.; Yamaguchi, S.; Tahara, T. Ultrafast vibrational dynamics of water at a charged interface revealed by two-dimensional heterodyne-detected vibrational sum frequency generation. *The Journal of Chemical Physics* **2012**, *137*, 094706.

[276] Laaser, J. E.; Zanni, M. T. Extracting Structural Information from the Polarization Dependence of One- and Two-Dimensional Sum Frequency Generation Spectra. *The Journal of Physical Chemistry A* **2013**, *117*, 5875–5890.

[277] Wu, H.; Zhang, W.-k.; Gan, W.; Cui, Z.-f.; Wang, H.-f. An empirical approach to the bond additivity model in quantitative interpretation of sum frequency generation vibrational spectra. *The Journal of Chemical Physics* **2006**, *125*, 133203.

[278] McCreery, R. L. *Raman spectroscopy for chemical analysis*; John Wiley & Sons, 2005; Vol. 225.

[279] Szymanski, H. A. *Raman spectroscopy: theory and practice*; Springer Science & Business Media, 2012.

[280] Shen, Y. R. Phase-Sensitive Sum-Frequency Spectroscopy. *Annual Review of Physical Chemistry* **2013**, *64*, 129–150.

[281] Chase, H. M.; Psciuk, B. T.; Strick, B. L.; Thomson, R. J.; Batista, V. S.; Geiger, F. M. Beyond Local Group Modes in Vibrational Sum Frequency Generation. *The Journal of Physical Chemistry A* **2015**, *119*, 3407–3414.

[282] Fu, L.; Xiao, D.; Wang, Z.; Batista, V. S.; Yan, E. C. Y. Chiral Sum Frequency Generation for In Situ Probing Proton Exchange in Antiparallel β-Sheets at Interfaces. *Journal of the American Chemical Society* **2013**, *135*, 3592–3598.

[283] Perry, J. M.; Moad, A. J.; Begue, N. J.; Wampler, R. D.; Simpson, G. J. Electronic and Vibrational Second-Order Nonlinear Optical Properties of Protein Secondary Structural Motifs. *The Journal of Physical Chemistry B* **2005**, *109*, 20009–20026.

[284] Nguyen, K. T.; King, J. T.; Chen, Z. Orientation Determination of Interfacial β-Sheet Structures in Situ. *The Journal of Physical Chemistry B* **2010**, *114*, 8291–8300.

[285] Nguyen, K. T.; Le Clair, S. V.; Ye, S.; Chen, Z. Orientation Determination of Protein Helical Secondary Structures Using Linear and Nonlinear Vibrational Spectroscopy. *The Journal of Physical Chemistry B* **2009**, *113*, 12169–12180.

[286] Xiao, D.; Fu, L.; Liu, J.; Batista, V. S.; Yan, E. C. Y. Amphiphilic Adsorption of Human Islet Amyloid Polypeptide Aggregates to Lipid/Aqueous Interfaces. *Journal of Molecular Biology* **2012**, *421*, 537–547.

[287] Singh, P. C.; Nihonyanagi, S.; Yamaguchi, S.; Tahara, T. Communication: Ultrafast vibrational dynamics of hydrogen bond network terminated at the air/water interface: A two-dimensional heterodyne-detected vibrational sum frequency generation study. *The Journal of Chemical Physics* **2013**, *139*, 161101.

[288] Hsieh, C.-S.; Okuno, M.; Hunger, J.; Backus, E. H. G.; Nagata, Y.; Bonn, M. Aqueous Heterogeneity at the Air/Water Interface Revealed by 2D-HD-SFG Spectroscopy. *Angewandte Chemie International Edition* **2014**, *53*, 8146–8149.

138

[289] Zhong, X.; Chervy, T.; Zhang, L.; Thomas, A.; George, J.; Genet, C.; Hutchison, J. A.; Ebbesen, T. W. Energy Transfer between Spatially Separated Entangled Molecules. *Angewandte Chemie International Edition* **2017**, *56*, 9034–9038.

[290] Georgescu, I. M.; Ashhab, S.; Nori, F. Quantum simulation. *Reviews of Modern Physics* **2014**, *86*, 153–185.

[291] Hartmann, M. J.; Brandao, F. G. S. L.; Plenio, M. B. Strongly interacting polaritons in coupled arrays of cavities. *Nature Physics* **2006**, *2*, 849–855.

[292] Dunkelberger, A. D.; Spann, B. T.; Fears, K. P.; Simpkins, B. S.; Owrutsky, J. C. Modified relaxation dynamics and coherent energy exchange in coupled vibration-cavity polaritons. *Nature Communications* **2016**, *7*, 13504 EP –.

[293] Xiang, B.; Ribeiro, R. F.; Dunkelberger, A. D.; Wang, J.; Li, Y.; Simpkins, B. S.; Owrutsky, J. C.; Yuen-Zhou, J.; Xiong, W. Two-dimensional infrared spectroscopy of vibrational polaritons. *Proceedings of the National Academy of Sciences* **2018**, *115*, 4845.

[294] Shim, S.-H.; Strasfeld, D. B.; Ling, Y. L.; Zanni, M. T. Automated 2D IR spectroscopy using a mid-IR pulse shaper and application of this technology to the human islet amyloid polypeptide. *Proceedings of the National Academy of Sciences* **2007**, *104*, 14197.

[295] Kuroda, D. G.; Bauman, J. D.; Challa, J. R.; Patel, D.; Troxler, T.; Das, K.; Arnold, E.; Hochstrasser, R. M. Snapshot of the equilibrium dynamics of a drug bound to HIV-1 reverse transcriptase. *Nature Chemistry* **2013**, *5*, 174 EP –.

[296] Bandarenka, A. S.; Koper, M. T. M. Structural and electronic effects in heterogeneous electrocatalysis: Toward a rational design of electrocatalysts. *Journal of Catalysis* **2013**, *308*, 11–24.

[297] Herrmann, J.-M. Heterogeneous photocatalysis: fundamentals and applications to the removal of various types of aqueous pollutants. *Catalysis Today* **1999**, *53*, 115–129.

[298] Litter, M. I. Heterogeneous photocatalysis: Transition metal ions in photocatalytic systems. *Applied Catalysis B: Environmental* **1999**, *23*, 89–114.

[299] Schultz, D. M.; Yoon, T. P. Solar Synthesis: Prospects in Visible Light Photocatalysis. *Science* **2014**, *343*, 1239176.

[300] Osterloh, F. E.; Parkinson, B. A. Recent developments in solar water-splitting photocatalysis. **2011**, *36*, 17–22.

[301] Alibabaei, L.; Brennaman, M. K.; Norris, M. R.; Kalanyan, B.; Song, W.; Losego, M. D.; Concepcion, J. J.; Binstead, R. A.; Parsons, G. N.; Meyer, T. J. Solar water splitting in a molecular photoelectrochemical cell. *Proceedings of the National Academy of Sciences* **2013**, *110*, 20008.

[302] Kudo, A.; Miseki, Y. Heterogeneous photocatalyst materials for water splitting. *Chemical Society Reviews* **2009**, *38*, 253–278.

[303] Warren, S. C.; Thimsen, E. Plasmonic solar water splitting. *Energy & Environmental Science* **2012**, *5*, 5133–5146.

[304] Machan, C. W.; Sampson, M. D.; Chabolla, S. A.; Dang, T.; Kubiak, C. P. Developing a Mechanistic Understanding of Molecular Electrocatalysts for CO2 Reduction using Infrared Spectroelectrochemistry. *Organometallics* **2014**, *33*, 4550–4559.

[305] Fujita, E. Photochemical carbon dioxide reduction with metal complexes. *Coordination Chemistry Reviews* **1999**, *185-186*, 373–384.

[306] Costamagna, J.; Ferraudi, G.; Canales, J.; Vargas, J. Carbon dioxide activation by aza-macrocyclic complexes. *Coordination Chemistry Reviews* **1996**, *148*, 221–248.

[307] Gaya, U. I.; Abdullah, A. H. Heterogeneous photocatalytic degradation of organic contaminants over titanium dioxide: A review of fundamentals, progress and problems. *Journal of Photochemistry and Photobiology C: Photochemistry Reviews* **2008**, *9*, 1–12.

[308] Wang, C.-C.; Li, J.-R.; Lv, X.-L.; Zhang, Y.-Q.; Guo, G. Photocatalytic organic pollutants degradation in metal–organic frameworks. *Energy & Environmental Science* **2014**, *7*, 2831–2867.